Modeling Operando Electrochemical CO2 Reduction

Modeling Operando electrochemical CO_2 reduction

Federico Dattila,[*,†,‡] Ranga Rohit Seemakurthi,[†] Yecheng Zhou,[¶] and Núria López[*,†]

†*Institute of Chemical Research of Catalonia (ICIQ), The Barcelona Institute of Science and Technology (BIST), Av. Països Catalans 16, 43007 Tarragona, Spain.*

‡*Current address: CREST Group, Department of Applied Science and Technology (DISAT), Politecnico di Torino, Corso Duca degli Abruzzi 24, 10129, Turin, Italy.*

¶*School of Materials Science and Engineering, Sun Yat-sen University, Guangzhou 510006, P. R. China.*

E-mail: federico.dattila@polito.it; nlopez@iciq.es

Abstract

Since the seminal works on the application of density functional theory (DFT) and the computational hydrogen electrode to electrochemical CO_2 reduction (eCO_2R) and hydrogen evolution (HER), the modeling of both reactions has quickly evolved for the last two decades. Formulation of thermodynamic and kinetic Linear Scaling Relationships for key intermediates on crystalline materials have led to the definition of activity volcano plots, overpotential diagrams, and full exploitation of these theoretical outcomes at laboratory scale. However, recent studies hint at the role of morphological changes and short-lived intermediates in ruling the catalytic performance under operation conditions, further raising the bar for the modeling of electrocatalytic systems. Here, we highlight some novel methodological approaches employed to address eCO_2R and HER reactions. Moving from the atomic scale to the bulk electrolyte, we first show how *ab initio* and machine learning (ML) methodologies can partially reproduce surface reconstruction under operation, thus identifying active sites and reaction mechanisms if coupled with microkinetic modeling. Later, we introduce the potential of DFT and ML to interpret data from *Operando* spectroelectrochemical techniques, such as Raman spectroscopy and Extended X-ray Absorption Fine Structure characterization. Next, we review the role of electrolyte and mass transport effects. Finally, we suggest further challenges for computational modeling in the near future as well as our perspective on the directions to follow.

Contents

1 Introduction

Electrocatalysis is a crucial process which "facilitates conversion between electrical and chemical energy in fuel cells and electrolysis devices".[1] Conversion of chemical energy into electrical energy takes place in a "galvanic" cell through spontaneous reactions occurring at the two electrodes once connected through a conductor.[2] Instead, exploitation of electrical energy to carry out chemical reactions takes place in an "electrolytic" cell by applying an external voltage across the electrodes greater than the open circuit potential.[2] In this review, we focus on electrocatalytic processes applied to electrolytic cells.

Due to the technological advances and consequent cost reduction enabled by the economy of scale of renewable energy within the last decades,[3] sustainable storage technologies as conversion of water to hydrogen (Hydrogen Evolution Reaction, HER) or electrochemical reduction of carbon dioxide (eCO_2R) will likely compete soon with the exploitation of fossil fuels.[4,5] The uptake of both processes has quickly evolved from pioneering outlooks at the beginning of the last century,[6] mainly as a result of key investigations,[7–11] as well as practical breakthroughs.[3,4,12] Over the last decade, most of the computational studies have been centered in going beyond Linear Scaling Relationships (LSR) and Computational Hydrogen Electrode (CHE),[8] typically applied to estimate the thermodynamics and kinetics of well-defined catalytic systems. In the present review we focus on the material gap between ideal structural models and the *in situ* catalytic phases under reaction conditions.

Very recently, new challenges are arising from processes occurring across the electrocatalytic cell during operation,[13–15] such as electric field, electrolyte, and mass transport effects, thus requiring more complex methodological approaches to rationalize the overall performance.[16] Many heavy methodological developments have been introduced to consider solvents either implicitly or explicitly and the effect of electric field (*i.e* the $jDFT_x$ scheme).[17–19] These approaches aim at incorporating these terms into the Kohn-Sham DFT formalism in an increasing self-consistent manner.[18] In contrast, much less attention has been paid to other modeling aspects, like the surface modifications induced at the electrode-electrolyte

interface or the impact of the current in restructuring the materials.

After a short preliminary discussion on the state-of-the-art research works, this review aims at giving a subjective, yet accurate overview about the advances in modeling electrochemical CO_2 reduction which have occurred for the last five years. Across the article, mentions to hydrogen evolution (competing reaction) and Oxygen Evolution Reaction (OER, anodic process) will instead be limited to specific cases. We start by discussing the main methodologies developed to rationalize eCO_2R on crystalline materials under well-defined reaction conditions (Section 2). Here we review approaches to reproduce the effect of electrochemical potential,[20] solvation,[21–26] and the concepts of network analysis and dimensionality reduction inherent to Linear Scaling Relationships.[27,28] Section 3 highlights new insights and corresponding challenges from *Operando* studies of electrocatalytic processes. Moving from catalyst to diffusion layer, we consider (1) reconstruction of active sites, (2) detection and identification of key reaction intermediates, and (3) electrolyte effects. In the core of the review, we discuss novel theoretical frameworks to tackle these experimental challenges. Initially, we focus on *ab initio* and machine learning techniques to model surface reconstruction under eCO_2R conditions (Section 4). Secondly, we underline the role of DFT vibrational analysis and microkinetic studies to complement spectroscopy and kinetic data to define reaction pathways for eCO_2 up to *n*-propanol (Sections 5-6). After, we introduce the relevance of multiphysics modeling and *ab initio* simulations to assess potential influences of pH and electrolyte species in CO_2 reduction activity and selectivity (Section 7). Section 8 offers a short discussion over applications of machine learning to (1) the development of atomistic potentials toward high computational efficiency and (2) the automatic extraction of structural properties from experimental data. Finally, we conclude the review by offering our own perspective on future developments needed in the field of computational electrocatalysis, as well as an outlook on relevant remaining research questions.

2 CO_2 reduction on crystalline materials

2.1 Hori's Milestones

The pioneering concept introduced by Giacomo Luigi Ciamician in 1912 – *By using suitable catalyzers, it should be possible to transform the mixture of water and carbon dioxide into oxygen and methane*[6] – is now a reality. In the field of eCO_2R, research has advanced from preliminary reports of polarization signals due to CO_2 reduction on mercury cathodes,[29] to production of added value C_{2+} products at high selectivities and current densities.[4,12] Catalytic search and mechanistic studies carried out by Hori and collaborators during the last forty years have elucidated the complexity of this reaction, thus providing key insights and experimental data for posterior theoretical rationalization.[9]

Since many of the milestones in the field naturally derive from Hori's work, we find it adequate to recall the main findings below.[7,30–37]

1. **Product distribution**. eCO_2R on Cd, Sn, Pb, In mainly accounts for formate. Zn is selective to formate or CO, whilst Cu is the only material which allows formation of C_{2+} compounds. Ag and Au catalyze CO_2 reduction to CO, whereas Ni and Fe are only active for HER.[7]

2. **Cation effect**. On a copper catalyst, cations with larger ionic radius promote CO_2 (CO) reduction to ethylene to the detriment of CH_4 production and eCO_2R activity correlates with cation ionic radius.[32]

3. **CO as key eCO_2R intermediate. pH effect (vs SHE reference**). High CO coverage ($\sim 90\%$) is observed during CO_2 reduction to hydrocarbons,[33] suggesting the relevance of adsorbed CO species. Ethylene and ethanol selectivity increases for bulk alkaline pH, whilst acidic pH favors methane production.[37] Thus, the rate-determining step (RDS) to form methane is expected to depend on pH, whilst ethylene production is pH-independent.[37] Spectroscopic signals for adsorbed CO are observed between -0.8

and −1.0 V vs NHE,[34] and are promoted by higher temperatures.[30,31]

4. **Copper facet sensitivity**. Cu(111) favors eCO_2R to methane. Cu(100) enables ethylene production, which is further promoted on (111) steps on (100). Conversely, (100) planes with (110) steps are mainly selective to ethanol.[35,36]

5. **Surface poisoning.** Metals contaminants, such as Fe^{2+} and Zn^{2+}, can poison copper electrodes during operation, causing its deactivation.[38]

2.2 Computational modeling

Many of the observations of Hori *et al.* for eCO_2R on well-defined catalysts (Section 2.1) in addition to evidence on other electrocatalytic reactions have been elucidated during the last decade through the introduction of the Computational Hydrogen Electrode[9] and the observation of Linear Scaling Relationships between CO_2 reduction intermediates (Sections 2.2.4).[11,39]

2.2.1 The "Anderson" Electrode

Albeit typically overlooked, the contribution of Anderson and his research group has been fundamental to the application of computational chemistry to electrocatalysis.[20] Already in 1982, Anderson and Ray studied hydrogen evolution on a Fe_5 cluster from H_3O^+ and H_2O reduction over a 4 V potential range simulated by shifting the Fe ionization potential.[40] This elegant approach was one of the first strategies to explicitly include potential bias in estimation of activation energies. Besides, the validity of this work is further highlighted by the assessment of different proton sources for HER, topic which has recently become very relevant in the field.[41,42] Few years later, Anderson and Kang extended their previous model by introducing an electron donor in the simulation cell to assess hydrogen evolution on diamond.[43] In this study, they employed H_3O^+ as proton source and CH_4 as a model molecule for the C-H bond (H on the diamond system). Besides, they placed a Li atom

coordinated to 1-2 water molecules 10 Å far away from the CH_4 molecule. Since equilibrium is assumed at the electron transfer, the electrochemical potential U of Li is given by Equation 1, where IP stands for the ionization potential of the alkali cation and 4.6 V represents the potential vs SHE of the electron. Different applied potentials were then estimated by simply tuning Li ionization potential. Remarkably, the use of alkali metals as electron donors has been reintroduced in 2016 by Nørskov and co-workers to assess explicit field effects in electrochemical CO_2 reduction on Ag,[44] and recently an analogous approach has allowed to rationalize the key role of cations in eCO_2R and HER on Au, Ag, and Cu.[42,45]

$$U = (IP/|e|^{-} - 4.6)\ \text{V} \tag{1}$$

One year later (1999), Anderson and Albu extended this framework to a general electron donor entity, D, representing the working electrode.[46,47] The chemical potential $\mu(D)$ of electrons at the electrode is defined as their Fermi energy, E_{F}, or equivalently as the negative of the electrode thermodynamic workfunction ϕ. On the standard hydrogen electrode scale, the electrode potential is then given by Equation 2, where the formula can be further simplified recalling the average value of 4.6 eV for $\phi_{\text{H}^+/\text{H}_2}$ and that $\phi = -\mu(D)$. The electron transfer to a specific reduction entity R is assumed to take place when the electron affinity of R, E_{ea}, matches the chemical potential of the donor, $\mu(D)$. The electron affinity of R can be estimated computationally as the difference between the energy of R and R^{-} with constant structure. Thus, different structures can be sampled and the ones which fulfill the relation $E_{\text{ea}} \sim \mu(D)$ identified. Finally, U can be derived from E_{ea} from the lowest energy configuration, see Equation 2.[46,47]

$$U = \phi - \phi_{\text{H}^+/\text{H}_2} = E_{\text{ea}} - 4.6\ \text{eV} \tag{2}$$

The last generalization of the "Anderson" electrode was developed to assess Oxygen Reduction Reaction (ORR) on a $Pt_3Cr(111)$ catalyst.[48,49] First, Roques and Anderson con-

sidered the well-known relationship between the variation of Gibbs free energy ΔG^0 for a given reduction reaction and the reversible potential U^0, Equation 3, where n is the number of electrons involved in the reduction and F is the Faradaic constant.[49] ΔG^0 can be estimated through the the reaction energy E_r plus a constant k which includes enthalpic, entropic, and solvation contributions. Equation 3 can then be further expanded as Equation 4, where the 4.6 V factor is due to the electron energy at 0 V vs SHE. In the computational study, Equation 4 allowed to determine the reversible potential for the reduction of OH radical (*i.e.* the reactant) to water (*i.e.* the product) with significant accuracy: $U^0_\mathrm{theo} = 2.99$ V vs $U^0_\mathrm{exp} = 2.81$ V.

Generalizing this approach, the reversible potential for a specific reduction reaction on a given catalyst M can be estimated by computing reactant R and product P binding strengths on the catalytic surface and correcting for the reversible potential given in aqueous solution, U^0_aq, see Equation 5.[48,49] As pointed out in Ref. 20 the only real difference between this methodology and the successive Computational Hydrogen Electrode formalism[8] is the choice of the OH radical as reference compound instead of H_2. Otherwise, both approaches are conceptually identical, since they include applied potential effects as linear corrections on the intermediates adsorption energies.

$$U^0 = -\frac{\Delta G^0}{n\mathrm{F}} \tag{3}$$

$$U^0 = -\left(\frac{E_r}{n\mathrm{F}}\right) - 4.6\ \mathrm{V} + k \tag{4}$$

$$U^0(M) = U^0_\mathrm{aq} + \frac{[E_\mathrm{ads}(P)_M - E_\mathrm{ads}(R)_M]}{n\mathrm{F}} \tag{5}$$

2.2.2 The Computational Hydrogen Electrode

Few months after the introduction of the "Anderson" electrode in February 2004,[48,49] Nørskov *et al.* introduced the Computational Hydrogen Electrode formalism to assess the effect of proton-coupled electron transfers (PCETs) on the thermodynamics of the oxygen reduc-

tion reaction on Pt(111) (Figure 1a).[8] This procedure is based on six steps and it is only applicable for reaction routes which occur *via* PCETs:

1. Following the Standard Hydrogen Electrode (SHE) scale, at standard conditions (pH = 0, 1 H_2 bar, T = 298.15 K, U = 0 V vs SHE), we can relate the chemical potential of a proton/electron couple to one half of H_2 Gibbs free energy.

2. Solvation contributions must be included either through explicit consideration of water molecules in the supercell,[8,22,25] or through implicit continuum models based on solvent dielectric permittivity.[23,24,26,50–52] Mixed schemes with explicit and implicit terms are less widely used than in homogeneous catalysis.

3. The Gibbs free energy of all the intermediates which involve an electron transfer (ET) must be shifted by $-n|e^-|U$, where n is the overall number of electron transferred (with electric charge in elementary unit $|e^-|$) and U the applied bias. Equation 6 reports a practical example to calculate the Gibbs free energy variation for CO_2 reduction to COOH *via* 1 PCET.

$$\Delta G_{*\mathrm{COOH}} = G_{\mathrm{products}} - G_{\mathrm{reactants}} = G_{*\mathrm{COOH}} - (G_{\mathrm{CO_2}} + \frac{1}{2}G_{\mathrm{H_2}} - |e^-|U) \qquad (6)$$

4. Electric field effects are estimated as $\vec{p} \cdot \vec{E}_{\mathrm{EDL}}$, where $\vec{p}$ is the dipole moment of the adsorbate and $\vec{E}$ is the electric field within the Electrical Double Layer (EDL).

5. At pH $\neq$ 0, the Gibbs free energy of the proton is linearly corrected *via* $k_B \cdot T \cdot \ln(10) \cdot$pH, in line with the Reversible Hydrogen Electrode (RHE) standard.

6. Gibbs free energy of adsorption must account for zero point energies and entropic contributions, including vibrational terms for adsorbed molecules).

The CHE formalism permitted the first mapping of experimental evidence to first principles calculations, such as cyclic voltammograms for H on Pt surfaces[53] and Pourbaix diagrams,[54] thus allowing significant advances in the field.[55] In the first application of the CHE

to CO_2 reduction,[9] overpotentials to form H_2, HCOOH, CO, and CH_4 obtained by DFT showed excellent agreement with experimental data from Hori's eCO_2R studies on copper (Section 2.1).[30,31] After more than a decade of success, the CHE is considered the fundamental framework to model the role of potential in the thermodynamics of electrochemical reactions under the assumption that activation energies can be initially disregarded.[56] Nevertheless, alternative approaches have been developed to include potential effects on reaction kinetics, as nicely summarized in this recent Review.[56]

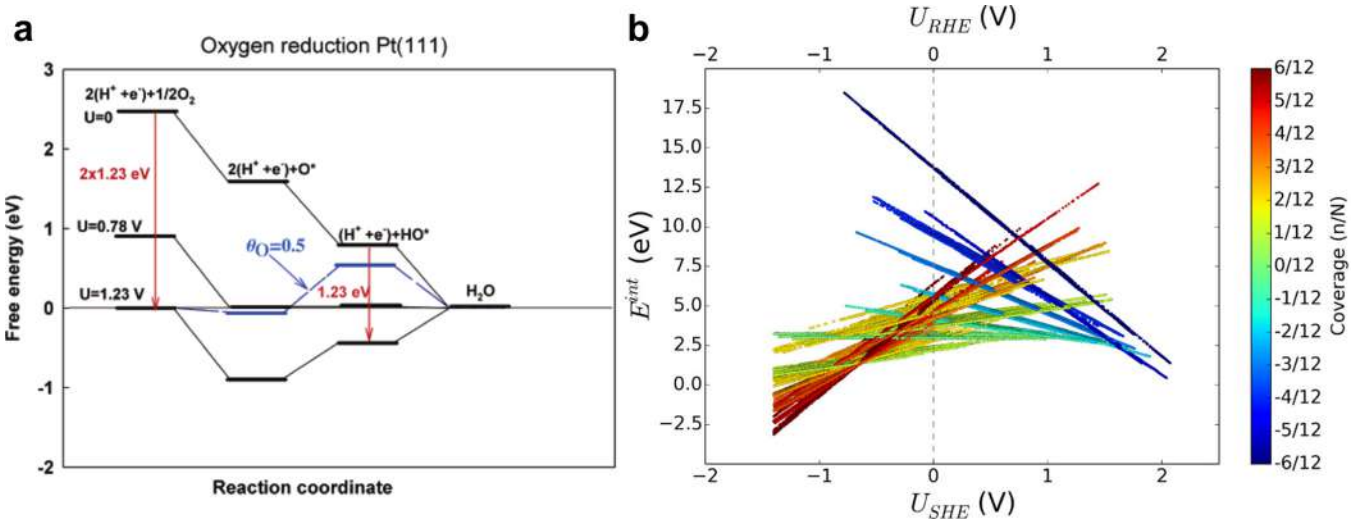

Figure 1: **a**, Determination of the Gibbs free energy diagram for oxygen reduction on Pt(111) at U=0 V vs SHE, U = +0.78 V vs SHE, and U = +1.23 V vs SHE through the CHE formalism. The energy profile at +1.23 V vs SHE for 0.5 ML oxygen coverage is highlighted in blue.[8] **b**,Interface energy vs U_{SHE} and U_{RHE} at pH = 0 calculated for different snapshots of *ab initio* molecular dynamics simulations carried out on a water/Au(111) interface with different number n of H^+ added to the system. N denotes the number of surface Au atoms (12).[57] Figures respectively adapted with permission from Ref. 8 (Copyright 2004 American Chemical Society) and Ref. 57 (Copyright 2016 American Chemical Society).

2.2.3 Beyond the Computational Hydrogen Electrode

Since the CHE formalism accounts for electric field effects only *a posteriori* from the dipole moment of the adsorbate (step 4 in Section 2.2.2),[8] recently Rossmeisl *et al.* developed a generalized formalism (GCHE) to include explicit interactions between electric field, intermediates, and solvent molecules.[58] Along with postulating that the bulk electrolyte is in

equilibrium and that the interface is in equilibrium with bulk electrodes and electrolyte, the GCHE assumes that the interface region is charge neutral and large enough to screen all charges.[57] Thus, a direct correlation exists between electron wave function, obtainable for a metallic surface through DFT, and electrode potential vs SHE at the electrochemical equilibrium. Additionally, the electrode potential can be referred to the RHE scale by correcting for the different pH.

According to the GCHE formalism,[58] the electrochemical potential of a proton/electron couple, $\mu_{\mathrm{H^+ + e^-}}$, can be calculated from Equation 7, where ΔG_{d} is the dissociation energy for $\frac{1}{2}$ $\mathrm{H_2}$, ΔG_{i} is the H ionization energy, $\phi_{\mathrm{e^-}}$ and $\phi^0_{\mathrm{H^+}}$ are respectively the work functions of electron and proton in solution (at pH = 0), measured with respect to the vacuum. Since for $U = 0$ V vs SHE and pH = 0 the electrochemical potential of the proton/electron couple is zero, Equation 7 can be simplified to Equation 8, where $\phi_{\mathrm{e^-}}(\mathrm{SHE}) = 4.44$ eV is the work function of an electron in a metal at the standard hydrogen electrode potential. Thus, $\mu_{\mathrm{H^+ + e^-}}$, $\phi_{\mathrm{e^-}}$, and pH are related *via* Equation 8 for a given metal/solution interface. $\phi_{\mathrm{e^-}}$ can be calculated from the electrode potential U, obtained from the interface dipole within the simulated cell, Equation 9.

$$\mu_{\mathrm{H^+ + e^-}} = \Delta G_{\mathrm{d}} + \Delta G_{\mathrm{i}} - \phi^0_{\mathrm{H^+}} - 2.3 \cdot \mathrm{k_B} \cdot T \cdot \mathrm{pH} - \phi_{\mathrm{e^-}} \tag{7}$$

$$\mu_{\mathrm{H^+ + e^-}} = \phi_{\mathrm{e^-}}(\mathrm{SHE}) - 2.3 \cdot \mathrm{k_B} \cdot T \cdot \mathrm{pH} - \phi_{\mathrm{e^-}} \tag{8}$$

$$U_{\mathrm{SHE}} = \frac{\phi_{\mathrm{e^-}} - \phi_{\mathrm{e^-}}(\mathrm{SHE})}{\mathrm{e^-}} \tag{9}$$

Since interface dipole, electrode potential, and electron work function are constant for a given structure, the Gibbs free energy of a metal/solution interface normalized per surface atom is defined at the electrochemical equilibrium (pH = 0) by Equation 10. n and N are respectively the number of hydrogens and surface metal atoms within the systems, while $G_{N,n}$, $G_{N,0}$, $G_{\mathrm{H_2}}$ are the Gibbs free energies of metal/solution interface, clean surface, and gas phase $\mathrm{H_2}$. These energies can be either calculated *via* DFT simulations or derived from

experimental data. Equation 10 can be extrapolated to account for pH $\neq 0$ as in Equation 11, where the proton/electron couple chemical potential can be obtained from Equations 8 and 9, knowing pH and estimating electron work function from the interface dipole.

$$G^{\text{interface}}(\mu_{\text{H}^+ + \text{e}^-} = 0, \phi_{\text{e}^-}) = \frac{G_{N,n} - G_{N,0}}{N} - \frac{1}{2}\frac{n}{N}G_{\text{H}_2} \tag{10}$$

$$G^{\text{interface}}(\mu_{\text{H}^+ + \text{e}^-}, \phi_{\text{e}^-}) = \frac{G_{N,n} - G_{N,0}}{N} - \frac{1}{2}\frac{n}{N}G_{\text{H}_2} - \frac{n}{N}\mu_{\text{H}^+ + \text{e}^-} \tag{11}$$

Following the GCHE principles relevant electrochemical properties, such as potentials of zero charge, Gibbs isotherms, and differential capacities as a function of pH, were estimated from DFT simulations on a Au/water interface.[57] Besides, the same methodology was applied to a Pt/water interface to estimate OH coverage vs bulk pH.[59] In Ref. 57, hydrogen atoms were either added or removed from the solvation layer and the resulting systems underwent *ab initio* molecular dynamics at 300 K with time step 0.5 fs to account for 90000 states with different number of protons in the system. Thus, the authors estimated the Gibbs free energy of the metal/solution interface as a function of applied potential and pH from Equation 11, see Figure 1b. They calculated the Gibbs free energies of Au/water system, the clean surface, and electron work function for all the AIMD snapshots with DFT. Finally, static properties of the interface were derived from grand canonical Metropolis Monte Carlo averages on the snapshots to define an ensemble with physical values of surface coverage and proton excess at any given electrode potential and pH.

Further approaches to relate thermodynamics/kinetics and electrochemical potentials involve the explicit insertion of electric field in slabs through an artificial dipole moments,[44,60–63] or the self-consistent solution of the Poisson-Boltzmann (PB) equation and the Kohn-Sham equations.[64–66] We refer to Ref. 20 for an accurate review of these methodologies.

2.2.4 Linear Scaling Relationships

In agreement with the Brønsted-Evans-Polanyi relation, first derived from experimental evidences,[67,68] kinetic Linear Scaling Relationships (kLSR) were demonstrated between activation barrier and reaction energy for different reactions.[69–73] Few years later Abild-Pedersen *et al.* developed a set of scaling properties between adsorption energies for hydrogen-containing molecules, the so-called thermodynamic Linear Scaling Relationships (tLSR), see Figure 2a.[10] The rationale behind these dependencies can be traced back to bond-order conservation theory and valence (octet) rules for light elements. As suggested by the *d*-band model,[74,75] the reactivity of a transition metal is mainly given by its *d*-band and this property affects an adsorbate depending on the bond order with the surface. When comparing the same metal in two environments, the system characterized by higher *d*-band center is more reactive, due to enhanced hybridization between the bonding and anti-bonding adsorbate states and the metal electronic states.[74]

According to the tLSR,[10] the adsorption energy for a given intermediate containing a hydrogen atom correlates with the bond order and ΔE_{sp}, parameter which depends on *sp* contribution to binding energy. In the case of adsorption of CH_x molecules on surfaces, tLSR are mathematically described by Equation 12, where $\gamma(x) = \frac{x_{\max}-x}{x_{\max}}$, $\xi = \Delta E_{sp}^{CH_x} - \gamma(x)\Delta E_{sp}^{C}$, and $x_{\max}$ is the maximum number of H atoms which can bond to C.

$$\Delta E^{CH_x} = \gamma(x)\Delta E^{C} + \xi \tag{12}$$

Analogous tLSR were demonstrated for NH_x, OH_x and SH_x intermediates,[10] thus suggesting their validity for other electrocatalytic reactions as well. In oxygen evolution reaction, binding energies of the reaction intermediates (*OH, *OOH, and *O) fulfill universal tLSR on both metallic[76] and oxidic systems,[77] thus leading to limitation of catalytic performance. Such limiting effect has been nicely exemplified through volcano plots correlating activity (or overpotential) for OER and energetic descriptors, as *O binding strength[76–79] or energy

differences (*e.g.* $\Delta E_{*\mathrm{O}} - \Delta E_{*\mathrm{OH}}$).[80] Similar volcano plots were defined for hydrogen evolution reaction, correlating *H binding and HER activity as first proposed by Trasatti.[41,81] Three decades later, Nørskov *et al.* employed this concept to rationalize the outstanding performance of Pt for HER, which is due to its thermoneutral *H chemisorption energy.[82]

In addition to tLSR based on electronic effects, analogous relationships were demonstrated between adsorption energies and coordination numbers of the active species,[83–85] predicting that surface defects exhibit stronger binding of cathodic reaction intermediates due to their lower coordination and consequently higher localized electronic density. Whilst the valence of the adsorbate (Equation 12) rules the slope of tLSR, both valence and local coordination of the catalyst center provides the offset. Hence, proper synthetic guidelines can tune the interplay of these effects to design systems with high performance by combining both electronic and structural dependencies of surface reactivity.[85] The application of this theoretical framework enabled the prediction of catalytic reactivity of defective surfaces for ORR and the identification of product-specific active sites motifs for $\mathrm{eCO_2R}$ on Cu.[86,87] Apart from coordination environment, local strain affects binding properties on metals as well, since lattice expansion leads to up-shift of the metal *d*-band and consequent stronger adsorption of reaction intermediates. Such phenomenon was first introduced by Mavrikakis and co-workers for *O and *CO on Ru and Au.[88,89] We anticipate here that this strain effect may be the physical foundation of the previously discussed coordination number-based linear scaling relationships.[83–85]

Since both thermodynamic and morphological linear scaling relationships are based on the *d*-band model, we here briefly mention a recent study from our group, highlighting the shortcomings of this framework to rationalize the adsorption energies of group 12 metals, such as Zn and Cd.[90] The reactivity of these two metals cannot be entirely described by their *d*-band center, suggesting the need for a second parameter. Hence, the authors introduced a second physical descriptor, the reduction potential,[91] to account for ionic effects on top of solely covalent interactions ruled by the *d*-band center. A statistical Principal Component

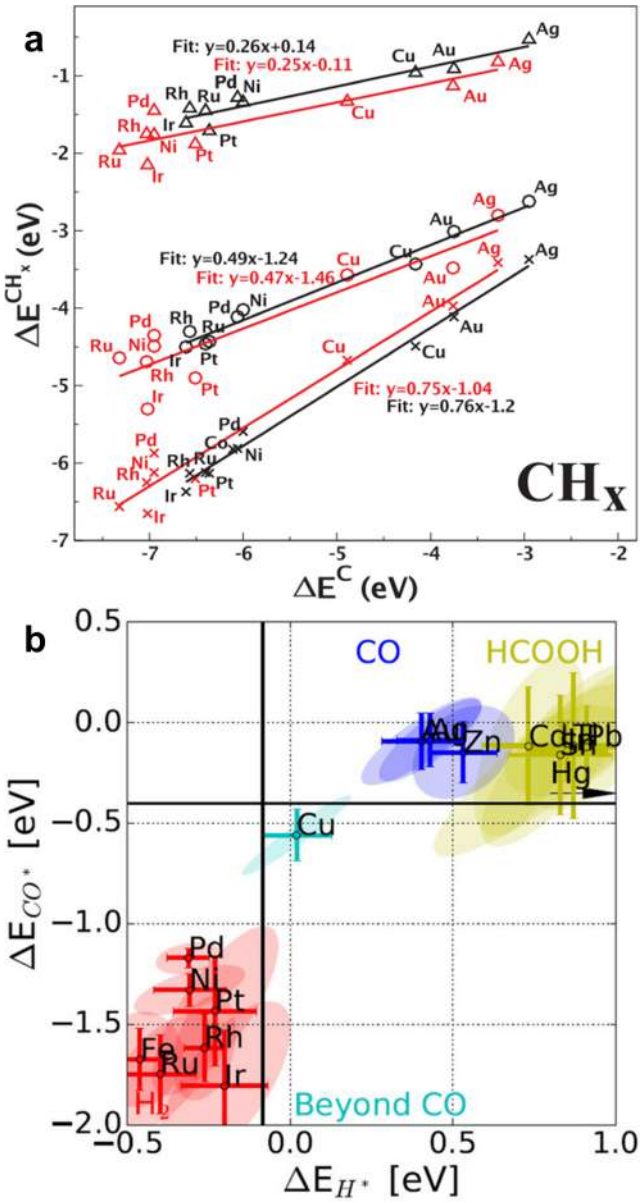

Figure 2: **a**, Adsorption energies of CH_x ($x = 1, 2, 3$ as crosses, circles, and triangles, respectively) vs adsorption energy of C on transition metals. Molecules in vacuum and clean surfaces were taken as energy references. Data points for close-packed and stepped surfaces are colored in black and red respectively.[10] **b**, $\Delta E_{*\mathrm{CO}}$ and $\Delta E_{*\mathrm{H}}$ as descriptors to classify transition metals into H_2 evolving catalysts (strong H binding), systems selective to C_{2+} (weak H binding, mild CO binding), and metals evolving CO (no H binding, weak CO binding) or $HCOO^-$ (no H neither CO binding).[11] Black lines highlight boundaries for H (x-axis) and CO adsorption (y-axis). Figures adapted with permission from Ref. 10 (Copyright 2007 American Physical Society) and Ref. 11 (Copyright 2017 Wiley-VCH) respectively.

Analysis (PCA) applied to DFT thermochemical data for 71 *H-, *O-, and *C-terminated C_1-C_2 adsorbed species on 12 close-packed metal surfaces confirmed validity of both covalent and

ionic descriptors to determine surface reactivity. By enabling prediction of surface reactivity, the developed framework enables quick screening of binding energy of intermediates and consequently it is transferable to the assessment of any reaction of choice.[92]

Following the discussion on application of tLSR to eCO_2R, Bagger *et al.* applied these concepts to classify the selectivity toward C_1-C_2 for *d*- and *p*−block metals,[11,93] observed experimentally by Hori *et al.* (Section 2.1).[7] A ΔE_{*HCOO} vs ΔE_{*COOH} LSR failed to differentiate between catalysts selective to CO (Ag, Au) and HCOOH (Zn),[11] thus they proposed three other descriptors: ΔE_{*COOH}, ΔE_{*H}, and ΔE_{*CO}, see Figure 2b.[11] The authors noted that metals which strongly bind *H are mainly selective to H_2, whilst CO-producing catalysts can adsorb both *COOH and *H. Besides, ideal systems for catalyzing eCO_2R to HCOOH must have endothermic *H adsorption. As for eCO_2R to C_2 products, a selective catalyst must exhibit a intermediate CO binding to hinder its release to the electrolyte, yet enabling C-C coupling.[93] Thus, Cu sits at the sweet spot, since it exhibits strong enough CO binding, but thermoneutral H adsorption. Finally, oxygen binding energy was proposed as a descriptor for alcohol vs hydrocarbon competition and this prediction was later confirmed by experimental reports on eCO_2R to methanol or methane on Au, Cu, and Ag electrodes.[11,94,95] As a crucial remark, we highlight that the above-mentioned descriptors are specifically tailored to single metals, thus alloys or oxide-derived materials may have completely different reactivity, see for instance eCO_2R to C_2 products (specifically ethylene glycol) on Fe_2P[96] and nickel oxygenates.[97]

In a following study, Bagger *et al.* included considerations on both thermodynamcs and surface morphology to rationalize Hori's results on copper single crystals (Section 2.1)[35,36] Since CO and H binding energies did not vary adequately to account for the different eCO_2R selectivity, the authors considered surface coordination number (N_{coord}) and adsorption energy (ΔE) of an extended list of intermediates (*OH, *OCCOH, *O, *H, *COOH, *CO, *C) as potential descriptors. By applying Principal Component Analysis on experimental Faradaic efficiencies, the authors demonstrated that structural properties can describe

C_{2+} compounds selectivity on copper better than binding energies:[39] (111) facet promotes methane, (110) acetaldehyde, (100) ethylene, whilst $n(100) \times (110)$ steps are responsible for ethanol production.

3 Challenges from electrocatalytic processes under working conditions

As we have seen, computational simulations on purely crystalline models were very effective in reproducing and rationalizing experimental observations on single crystals and under well-defined conditions (Sections 2.2.2-2.2.4). Particularly, all the terms contributing to the Gibbs free energies have been benchmarked extensively, demonstrating that the equations to obtain the energies are robust and contain all the key elements to constitute an accurate first order approach. However, limitations have been identified as the thermodynamic descriptor inherent to the CHE approach might not be sufficient. For instance, in the HER process the typically assumed $\Delta G_H = 0$ eV target of the volcano plot has been challenged due to coverage, kinetic, and the explicit applied overpotential effects.[98,99] In addition, new challenges are arising from *Operando* characterization when electrocatalytic systems are ruled by dynamic processes. This particularly affects the material gap between the prepared catalyst and its state under reaction conditions along with mass transport and concentrations at the interfaces between the electrode, electrolyte, and bulk solution.

3.1 Reconstruction of active sites during operation

Recently, many different observations of surface reconstruction towards optimized electrocatalytic performance were put forward. In the field of electrochemical CO_2 reduction, copper surface reconstruction has been discussed to a large extent during the last decades.[14,63,100–103] *Operando* characterization *via* Electrochemical Scanning Tunneling Microscopy (EC-STM) and Raman spectroscopy highlighted the reconstruction of polycrystalline copper (pc-Cu)

to (100) facets,[102] and nanocuboids.[63] Air-oxidized copper naturally reconstructed toward Cu(100) facets at cathodic bias,[104] as well as Cu(110) and copper materials including both polycrystalline and (111) facets.[105] Generally, product distribution and activity of copper catalysts strongly depends on the synthetic procedures, thus suggesting a completely different morphology on reconstructed surfaces than single crystals.[35,36,106] Specifically, oxide-derived copper mainly produce ethylene,[107–114] ethanol,[109] *n*-propanol,[109,115] and traces of acetate and ethane,[109,116] in line with the eCO_2R performance of copper nanoparticles at higher overpotentials[117–120]

Recent studies further confirm the role of metastable or kinetically trapped phases, surface reconstruction, and solvent molecules in tuning catalytic performance.[14,107,112,114,121] Carbon isotopic labelling ($^{12}CO_2$ vs $^{13}CO_2$) differentiated between three specific active sites on oxide-derived copper (OD-Cu) catalyst, selective to (1) ethanol and acetate; (2) ethylene, and (3) 1-propanol, whilst no difference was found for crystalline Cu.[122] Furthermore, a Cu_2O-derived material showed an outstanding CO reduction selectivity toward ethanol and acetate at very low cathodic bias ($\sim 40\%$ and $> 10\%$ Faradaic efficiency at -0.3 V vs RHE for 0.1 M KOH respectively),[109] suggesting residual oxygen or solvent water to take part into CH_3COO^- formation.[123,124] A successive study on $C^{16}O$ reduction in a $H_2^{18}O$ electrolyte on crystalline copper facets confirmed that around 65%, 80%, and 70% of ethanol, acetate, and 1-propanol products had at least one oxygen from solvent molecules.[125] The presence of low amount of residual oxygen during CO_2 reduction conditions has been demonstrated by oxygen isotopic labelling ($< 1\%$ of the original content within 100 nm).[119] Recently, an independent study has detected the presence of residual oxygen under reductive conditions through grazing incident hard X-ray Photoelectron Spectroscopy.[126] The authors identified those species as oxygen present at defects and/or vacancies on the surface and oxygen intercalated within metal layers. Arán-Ais *et al.* showed that C_{2+} products formation correlates with the amount of surface defects and percentage of Cu(I) site during pulsed CO_2 electroreduction.[14] In particular, the extent of Cu(100) terraces promotes ethylene selectivity,

whilst Cu(I)-Cu^0 sites, together with defects, lead to higher ethanol production. An elegant assessment of Cu(I) reducibility through pulsed eCO_2R at different temperatures further indicated that, when the kinetics of Cu(I) reduction is minimized ($T = 278.14$ K), ethanol is the main C_2 reduction product to the detriment of ethylene formation (Figure 3a).[127] Finally, DiDomenico *et al.* proposed that pulsed CO_2 electrolysis may have two-fold impact on eCO_2R: (1) "self-cleaning" of the catalysts from surface poisons (from $E_{\text{anodic}} > -0.5$ V) and (2) enhanced C_{2+} selectivity due to electrolyte/electric field effects (from $E_{\text{anodic}} > -0.1$ V).[128]

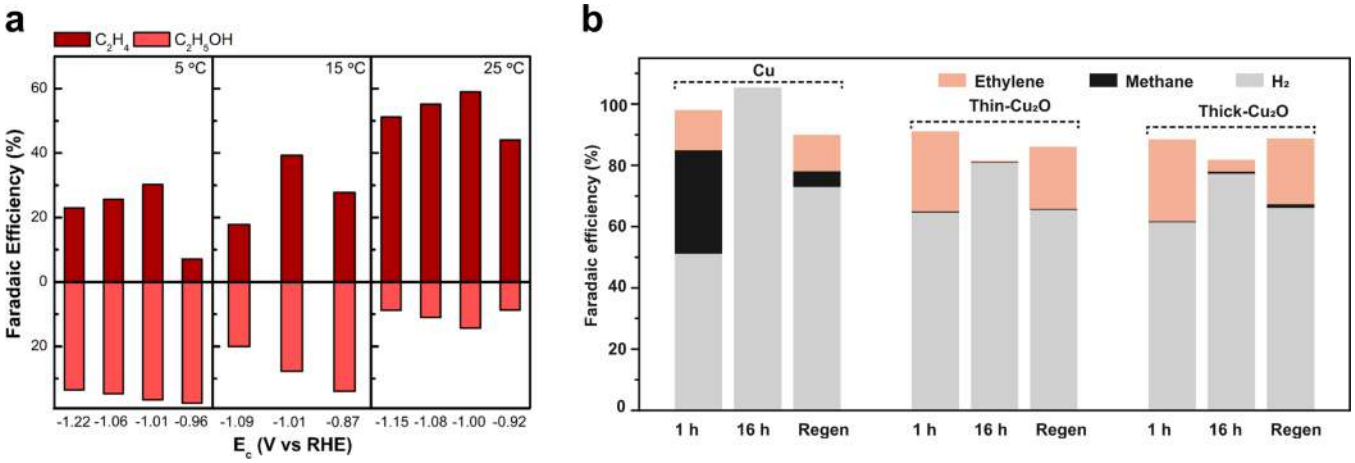

Figure 3: **a**, Faradaic efficiencies of ethylene and ethanol for eCO_2R in 0.1 M $KHCO_3$ on Cu at different cathodic bias and applied temperatures. Anodic pulse: +0.6 V vs RHE, timesteps for anodic and cathodic pulses: 1 s.[127] **b**, Product distribution on Cu, thin Cu_2O, and thick Cu_2O for CO_2 reduction in a 0.1 M K_2CO_3 electrolyte at −1.0 V vs RHE after 1 hour, 16 hours of continuous operation, and regeneration of the oxide layer by exposing the catalyst to air for two weeks after operation.[129] Figures adapted with permission from Ref. 127 (Copyright 2021 American Chemical Society) and Ref. 129 (Copyright 2021 National Academy of Sciences) respectively.

Recently, it was highlighted that almost no CO_2 reduction products are formed in absence of oxygen or surface defects.[129,130] After 16 hours of operation at −1.0 V vs RHE in CO_2-saturated 0.1 M K_2CO_3 electrolyte, hydrogen evolution was the only electrocatalytic reaction observed on both pc-Cu and a Cu/Cu_2O catalyst, unless oxygen was reintroduced in the system (Figure 3b). Since the authors demonstrated through *in situ* Raman spectroscopy that Cu_2O was fully reduced after only 1 hour at −1.0 V vs RHE, they highlighted the rel-

evance of disordered Cu^0 for C_2H_4 production. Additionally, CO_2 reduction performance differs significantly depending on the pre-treatment of the catalyst, as shown in a recent work on well-defined Cu(100) and Cu(111) facets. These catalysts were prepared by pristine atomically flat Ultra-High Vacuum (UHV) specifically to reproduce Hori's results.[35,36] UHV-prepared, sputtered, electrochemically polished, and O_2 plasma treated copper surfaces presented similar eCO_2R reduction current densities normalized by their electrochemically active surface area,[130] in line with a recent outlook.[131] Higher Faradaic efficiencies toward eCO_2R products on electrochemically polished and plasma treated samples were entirely due to suppression of H_2 production,[130] expected to happen due to variations of surface pH.[131] Hydrocarbons were observed only for electrochemically polished or plasma-treated samples, thus surface defects were deemed responsible for tuning CO binding energy, crucial property to enable the C-C pathway. These features were observed by CO Temperature Programmed Desorption (TPD) analysis.

Briefly extending the discussion to OER catalysts, a pristine $SrIrO_3$ catalyst performed better than IrO_x and RuO_x for OER due to strontium leaching during operation.[13] The resulting non-stoichiometric catalyst enables only 0.27-0.29 mV overpotential for 30 hours of continuous operation. X-ray Photoelectron Spectroscopy (XPS) on Ir $4f$ and Sr $3d$ observed a decrease of Sr signal to 25% of its original value after only 30 minutes and 20% after 24 hours. Thus, a novel structure was entirely formed *in situ* and became extremely active after 2 hours of electrochemical testing. Besides, the typically employed Ni materials reorganize extensively to form oxyhydroxy-compounds[132–135] which may be further doped by iron coming from nonpurified electrolytes.[54,136–138] Under operation, nickel catalysts evolve from α-$Ni(OH)_2$ at low potentials to γ-NiOOH at high potentials as indicated by Ni K-edge X-Ray Absorption Spectroscopy (XAS) measurements.[139] In addition to the morphological evolution, the layer-layer stacking is typically enlarged by water insertion and all these structural changes lead to improvements in the reactivity of the active sites as well as the mass transport of the reaction intermediates. The complexity of the system increases when

Ni electrocatalyst are doped with Ir ions, since these dopants may coordinate with water molecules in solution, adsorb on the surface, and/or intercalate across the NiOOH lattice.[54]

3.2 Short-lived reaction intermediates

Many computational and experimental mechanistic studies have been dedicated to disentangle the key intermediates and elementary steps of catalytic reactions,[9,37,140–142] toward an accurate description of the reaction pathways for eCO_2R reduction on transition metals.[143,144] Steady adsorbates have been successfully identified through spectroscopic techniques,[145] thus confirming theoretical predictions on adsorbed species.[9] However, short-lived intermediates formed during reaction pose a new challenge to both spectroscopy,[146] and computational modeling. These species are typically crucial for differentiating mechanistic routes and ruling activity, as in the case of $OCCO^-$ along the C_{2+} route,[16] and their unequivocal identification needs an integrated approach involving experimental and theoretical characterization.[16,147]

As a clear proof of the relevance of short-lived intermediates, lately new features have been reported through *Operando* techniques.[148–150] Surface-selective infrared spectroscopy has been employed to sample CO adsorption configurations on copper.[151] By integrating the C=O vibrational bands associated to bridge adsorption site (1800-1900 cm^{-1}) and top adsorption site ($\sim$ 2100 cm^{-1}) at different cathodic bias, top-bound CO was indicated as the only active species for both eCO_2R and CO reduction (COR). Besides, the authors observed that this specific adsorption configuration partially converts to unreactive bridge-bound CO below CO saturation regime.[151] An *et al.* further confirmed the presence of a reactive CO configuration *via* Time-Resolved Surfaced Enhanced Raman Spectroscopy (TR-SERS) for CO_2 reduction on copper nanoparticles. They revealed a highly dynamic, short-lived CO intermediate with low frequency C=O vibration ($\sim$ 2060 cm^{-1}, Figure 4a), appearing at -1.0 V vs RHE, the sweet spot for ethylene formation (Figure 4b).[152] Concurrently, an independent work observed the increase in Cu-CO stretching band at the expense of Cu-

CO rotation band for high CO partial pressure and high negative potential and related this feature to C-C coupling.[153] Lately, two vibrational signals at $\sim$ 490 cm^{-1} and $\sim$ 530 cm^{-1} have been detected on Ag-decorated Cu_2O catalysts using *Operando* SERS for potentials more negative than -1.0 V vs RHE, with a concurrent increase in selectivity toward ethanol, 1-propanol, and acetaldehyde.[154] A proper assignment of these bands may shed light on the preferential selectivity of Ag-based catalysts toward oxygenates[155,156]

3.3 Electrolyte effects

Electrolyte, as well as mass transfer of reaction intermediates, are crucial parameters for electrocatalytic reactions, as CO_2 reduction,[158,159] hydrogen evolution,[42,160,161] and oxygen evolution,[162] since concentration profiles at the interface might severely depart from the bulk electrolyte composition.[2,16,162–164] For instance, alkaline pH at the surface is expected to promote CO_2 reduction to C_{2+} to the detriment of C_1 products.[165–167] Laser-microstructured cavities on copper allowed the local tuning of surface pH and CO_2 concentrations, confirming high Faradaic efficiency (F.E.) toward ethanol, ethylene, and propanol for alkaline pH and intermediate CO_2 concentration.[167] Further investigations with pulsed CO_2 reduction proved a two-fold effect of anodic bias in lowering the surface pH and stabilizing and/or generating polarized sites.[168] Whilst for a anodic bias of +0.9 V vs RHE the authors observed a 10% enhancement of C_2 selectivity with respect to the lack of anodic pulses, a more positive bias ($E_{\text{anodic}} = +1.2$ V vs RHE) resulted in increased CH_4 production due to consumption of OH^- at the surface and a consequently more acidic pH.[141] Finally, ions in the electrolyte are also crucial for cathodic reactions as eCO_2R and HER. Cations are expected to interact with reaction intermediates through local electric field effects,[32,169–171] or inducing water electrolysis from their solvation shell,[172] whilst anions are mainly responsible for surface poisoning due to specific adsorption.[2,173–176] Besides, the impact of ions is not only limited to transition metals, as demonstrated by observed cation effect for CO_2 reduction on perovskite oxides.[177]

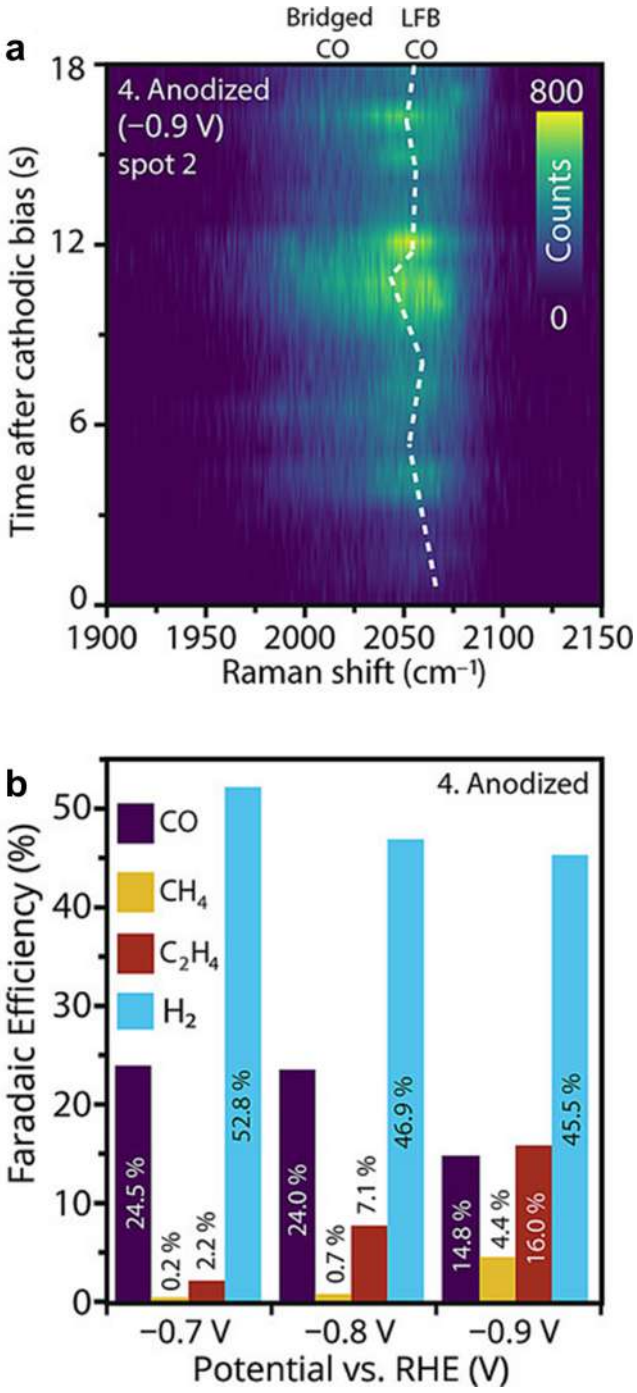

Figure 4: **a**, Time-Resolved Surface Enhanced Raman Spectroscopy (TR-SERS) heat map on anodized mechanically polished Cu at −0.9 V vs RHE, showing a low-frequency band due to an highly dynamic CO intermediate. Raman spectra interval: 717 ms. **b**, Catalyst performance at different applied potential in a CO_2-saturated 0.1 M $KHCO_3$. Figures adapted with permission from Ref. 152 (Copyright 2021 Wiley-VCH under Creative Commons Attribution 4.0 International License[157]).

Whilst simulations on crystalline models successfully accounts for some of these phenomena, the assessment of the interplay of cation, surface pH, and mass transfer effects is so far limited. Recently, specific anion and cation contributions were employed in an empirical way to promote long-term stability for CO_2 reduction on continuous-flow electrolyzers.[15] Since flow cells undergo deactivation due to formation of salt at the cathode,[176] Endrődi *et al.* designed a novel *Operando* procedure, where fresh electrolyte solution (1.0 M CsOH) was introduced into the CO_2 feed every 12 hours to regenerate and activate the silver cathode. Through this process, they achieved partial current density for CO up to 420 mA cm^{-2} for more than 200 hours. They attributed the enhanced performance of this proof-of-concept setup to physical interactions, such as removal of salt at the cathode from the fresh solution and promoting effects from the cations. Besides, benchmark studies of the reaction conditions indicated that CO Faradaic efficiency depended on bulk pH, peaking at pH = 13.6 ($j_{CO} > 200$ mA cm^{-2}), thus suggesting the concurrent influence of surface pH effects.[178] Very recently, a fundamental study demonstrated the triggering role of alkali metals in enabling CO_2 reduction on polycrystalline Au, Ag, and Cu in acidic media due to stabilization of a short-lived $*CO_2^-$ intermediate.[45] Such evidence was reported independently for eCO_2 on a copper Gas Diffusion Electrode (GDE) configuration, even though the authors observed such effect only for nonacidic bulk pH.[179] In fact, different pH regimes lead to variations in cation concentration at the surface,[180]as rationalized by Goyal *et al* through fundamental experiments and theoretical insights.[161]

Cation effects extend beyond eCO_2, since they have been identified as well for HER, ORR, and OER on different electrodes. Along the alkali group, as the ionic radius increases, higher reduction activities are typically expected (Figure 5), however the mechanism underlying this promotional phenomenon is widely debated. Gao *et al.* reported that the alkali-metal ions significantly influence the oxidation state of Mn in MnO_x OER catalysts.[182] Specifically, Li^+ ion stabilizes the Mn^{2+} species, which is OER-inactive, thus leading to low OER performance for small radius cations.[182] Instead, Garcia *et al.* postulated that the superior OER catalytic

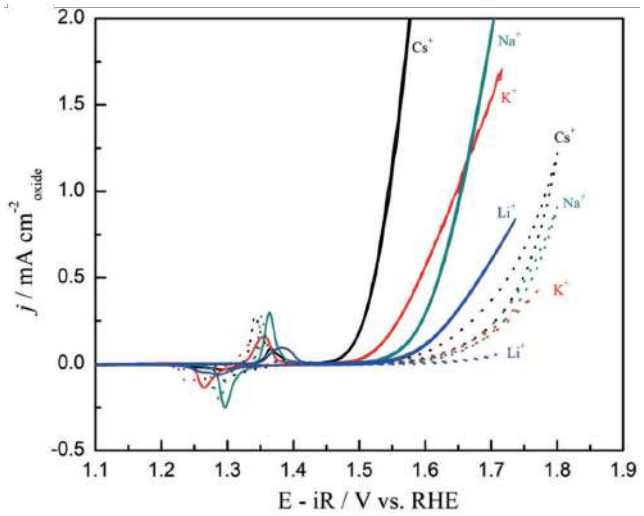

Figure 5: Cyclic voltammograms of NiOOH at pH 13 during OER in different electrolytes. Solid lines: unpurified electrolytes; dotted lines: purified electrolytes. Measurements were performed under rotation of the working electrode (1600 rpm) and collected at 0.010 V s^{-1}.[181] Adapted with permission from Ref. 181 (Copyright 2019 Wiley-VCH).

performance of larger cations M^+ is due to specific interactions with Ni-OO^- species to form $NiOO^- \cdots M^+$ complexes, whose formation is increasingly stabilized as the cation radius becomes larger.[181]

On top of cations, anions are relevant for OER as well, since they may accumulate at the anode and form complexes on the surface. Eventually, these species may lead to deactivation and/or degradation of the employed catalysts,[162] thus considerable effort has been devoted recently to tuning the chemical environment at the anode.[183] Typically, these anionic complexes generated on the surface are hard to identify since they evolve during operation, converting to other chemicals depending on surface pH and applied potential.[184] For instance, for a Pt(111) catalyst in sulfuric acid solution different anionic adsorbates have been proposed such as sulfate,[185] bisulfate,[186] $SO_4^{2-} \cdots H_3O^+$ ion pairs,[187] or OH^-.[188] To further increase the complexity of these processes, mutual dependencies between cations and anions are also expected, since cations may act as counterions and stabilize anions species. García *et al.* proposed a similar mechanism for anions on Pt, suggesting a two layer morphology with chemisorbed (bi)sulfate on the Pt catalyst and adsorbed cations on the

(bi)sulfate layers.[189]

3.4 Perspective for *Operando modeling*

Recent experimental challenges summarized in Sections 3.1-3.3 cannot be fully rationalized through simulations on as-synthesized crystalline models,[190] which in brief we here define as *"as-synthesized" modeling* (Section 2.2). New approaches must be developed to reproduce electrocatalytic conditions, addressing the material gap and mass transport phenomena within the diffusion layer[2] toward the definition of an *"Operando" modeling* framework.[123] Predictions achieved through this new approach must then be validated by *ad hoc* experimental studies under well-defined conditions.[190]

This framework should aim at realistically assessing (1) electric field/adsorbate driven surface reconstruction, (2) evolution of active sites and consequent changes in catalyst reactivity, (3) electrolyte effects as cation/anion/solvation contributions to electrocatalytic reactions, (4) mass transfer, and (5) surface/bulk pH effects. These five challenging phenomena are certainly crucial in tuning the overall performance of electrocatalytic cells, thus in our opinion the field of computational modeling should tackle these challenges, possibly by integrating these processes into generalized, multiphysics models. While insights from computational studies on as-synthesized catalysts (in brief, *as-synthesized modeling*, Figure 6) are only partially valid under operation, *"Operando" modeling* can properly tackle challenges from *Operando* characterization. Thus, by assessing more "realistic" conditions, this novel framework could enable the identification of potential-, adsorbate-, and pH-dependent actives sites and trigger a second step in the optimization cycle, Figure 6.

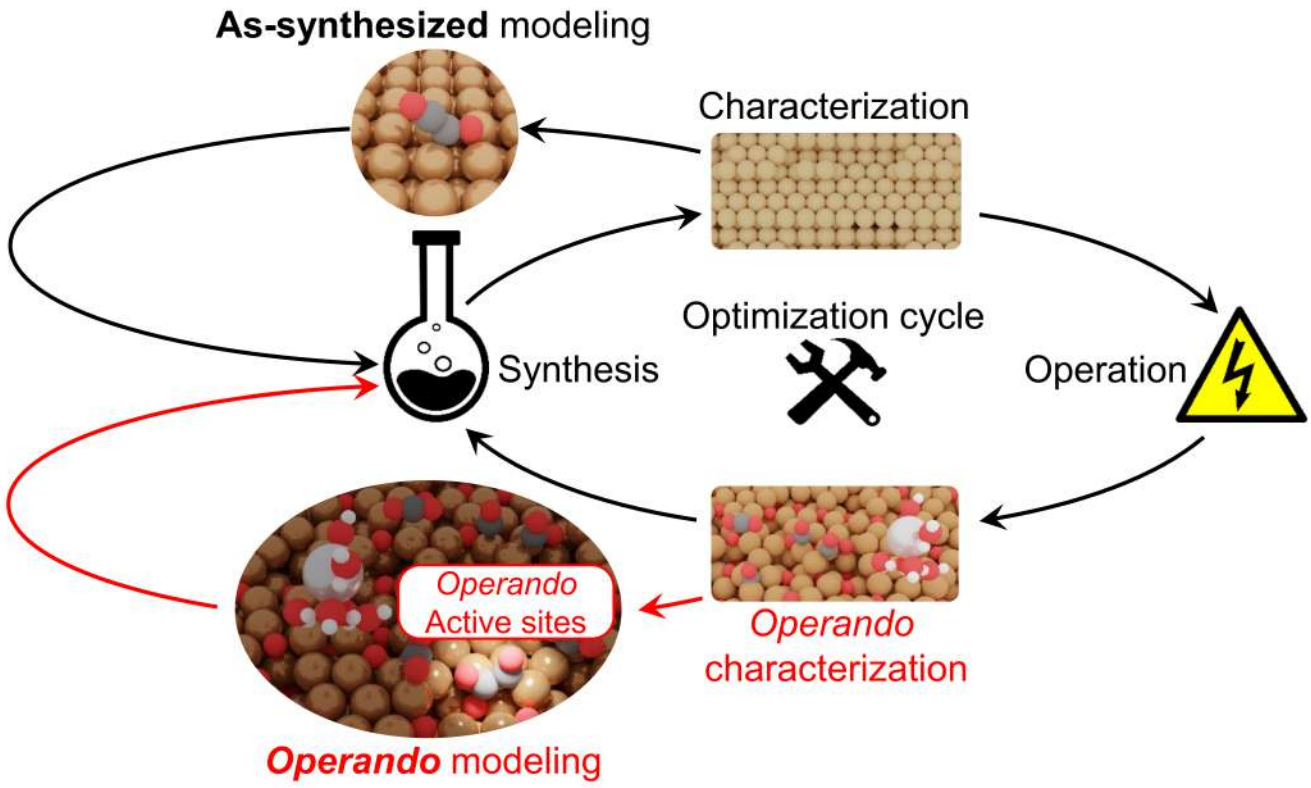

Figure 6: Catalyst optimization cycle and contribution from *"as-synthesized" modeling* and *"Operando" modeling*. Characterization of pristine systems and *Operando* tracking of structural changes and/or intermediates provide fundamental understanding of the role of the active sites. After two decades of modeling of as-synthesized catalysts, theoretical methods must now move toward the accurate modeling of the overall reaction environment during operation.

4 Modeling reconstruction under electrochemical conditions

Surface sensitivity, *i.e.* the contribution of surface morphology to catalytic activity and selectivity, has been extensively assessed in the field of catalysis,[191] leading to the development of Linear Scaling Relationships correlating adsorption energies of reaction intermediates and coordination number of the active sites (Section 2.2.4). Application of these concepts to crystalline domains suggest that undercoordinated sites bind adsorbates more strongly,[83–85] motivating both the high reactivity of defects for eCO_2R reduction,[14,129,192] and the raise of competing HER for surface atoms with very low coordination number.[117,193]

Even though defined synthetic procedures and catalyst treatments have proved effective to increase the density of surface defects,[112,194–197] reconstruction phenomena occurring during operation have prevented the reproducibility and scalability of these approaches.[63,102,198–200] Additionally, poor modeling of reconstruction processes hinders the identification of active sites during operation and thus prevents the definition of guidelines to maximize these reaction centers. The material gap, important in thermal catalysis, is even more acute in the context of electrochemistry, as the potential and electrolyte are thermodynamic sinks to which the simulations are typically not coupled. Furthermore, thermodynamic considerations alone cannot reproduce local morphologies originated from kinetic processes,[201] such as metastable and kinetically trapped ensembles which might be extremely active in electrocatalysis.[202–207] A comprehensive investigation of kinetic effects driving surface restructuring through purely static DFT simulations is limited by the large configuration space of detective surfaces, thus such studies can be performed only under well-defined mechanistic hypothesis[208] or through machine learning (ML).[209] The ML strategy is promising, yet not fully realizable to date. Besides, for suitable application to electrocatalysis it should be generalized to include electrolyte species and adsorbates. As an ultimate consequence, experimental studies are not yet able to fully exploit theoretical insights from models based

only on thermodynamic contributions and crystalline materials.

In this section, we will discuss new methodologies to (1) assess the thermodynamics and kinetics of adsorbate-driven surface reconstruction on crystalline facets,[100,208] and (2) to reproduce metastable phases formed during catalytic reactions.[54,210,211] This second strategy is particularly relevant, since application of molecular dynamics enables the assessment of surface patterns which originate from non thermodynamic processes. Nevertheless, the robustness of such DFT-MD approach must be properly validated through *ad hoc* experiments, as Korpelin *et al.* have recently highlighted.[212] All in all, detailed computational characterization of these reconstructed surfaces allows to identify active sites responsible for improved catalytic performance as well as local effects which tune activity and selectivity (Sections 4.3-4.4).[166,210,211,213]

4.1 Restructuring processes on "as-synthesized" models

Copper reconstruction has been observed through different characterization techniques and under distinct conditions. Low-Energy Electron Diffraction (LEED) and Scanning Tunnelling Microscope (STM) have detected surface restructuring under ultrahigh vacuum conditions in presence of O and H adsorbates,[214–219] or graphene overlayers.[220] Besides, this continuous process occurs as well under electrocatalytic conditions, as reported through *Operando* EC-STM for HER[221,222] and with electrolytes typical of CO_2 reduction.[63,100,102,103,105,198,223,224] Overall, cathodic bias alone or surface modifications *via* adsorption of H or C species are expected to be the main promoters of such reconstruction,[224] nevertheless at very negative potential specific cation adsorption may also play an active role.[225,226]

Researchers from the groups of Prof. Buonsanti and Prof. Marzari assessed the extent of morphological evolution in copper under CO_2 reduction conditions and described a potential-driven degradation mechanism due to CO and H adsorption *via* Grand-Potential density functional theory simulations.[100] Copper nanocubes with different sizes (16, 41 and 65 nm) were subjected to CO_2 electrolysis in a 0.1 M $KHCO_3$ electrolyte at -1.1 V vs RHE.

Although some cuboids were still observable after 6 hours, after 12 hours the nanoparticles underwent a full degradation of the crystalline facets, which caused a marked increase of HER. Nanoclustering was observed as well in a CO_2-free electrolyte, thus suggesting the instrumental role of applied potential for enabling this phenomenon. To assess the influence of both adsorbates and applied potential, the authors employed DFT simulations on specific crystalline facets of copper, either clean or covered by H, CO, and H+CO with solvation included through a self-consistent polarizable continuum model.[227]

A grand canonical approach was applied to predict the potential-dependent equilibrium shape of nanoparticles under electrochemical conditions.[228] In case of adsorption of a proton, the dependence of the free energy of a catalytic system versus the potential U at the RHE scale is defined by Equation 13. ΔG is the Gibbs free energy for hydrogen adsorption, corrected for entropic and zero-point energy contributions, obtained from DFT. The last term accounts for the variation of configurational entropy of the surface upon H adsorption. Contribution for the bulk pH is intrinsically included in the RHE dependence of the potential. The electrode potential U is obtained from the variation of electrostatic potential between vacuum and the Fermi energy of the metal, which was induced in the study by introducing opposite charges localized respectively on the slab and at 3 Å from the surface, and then correcting for the potential of zero charge. Hydrogen coverage θ at equilibrium can be estimated as a function of applied potential U by solving Equation 13 for $\Delta G_{\mathrm{tot}} = 0$. Consequently, the surface energy γ of a given system in presence of an adsorbed species is calculated from the electrocapillary equation knowing θ and U. This method can be extrapolated to any species involving an electron transfer from the surface, i.e. CO.

$$\Delta G_{\mathrm{tot}} = |\mathrm{e}^-| U_{\mathrm{RHE}} + \Delta G(\theta) + \mathrm{k_B} T \ln\left(\frac{\theta}{1-\theta}\right) \tag{13}$$

This methodology reproduced the well-documented thermodynamic stability trend of copper facets without potential: $\gamma_{110} > \gamma_{100} > \gamma_{111}$, which implies that the formation of

(111) facet requires less energy than (100) and (110) cleaving. However, at cathodic bias, the adsorption of H and CO reduces the interface free energy, leading to negative surface energies for potential more negative than −0.5 V vs RHE (Figure 7a-b). A negative surface energy implies instability of the given facet and its degradation or evolution toward a stable domain.[229,230] Thus, the authors proposed that surface dissolution starts at the edges of the nanocuboids and more negative potentials determine a stabilization of non cubic domains, *i.e.* (111), to the detriment of cubicity. The predicted triggering effect of negative enough applied potential to enable reconstruction was confirmed by experimental studies at more positive voltages (−0.7 and −0.3 V vs RHE), for which no significant degradation was observed.

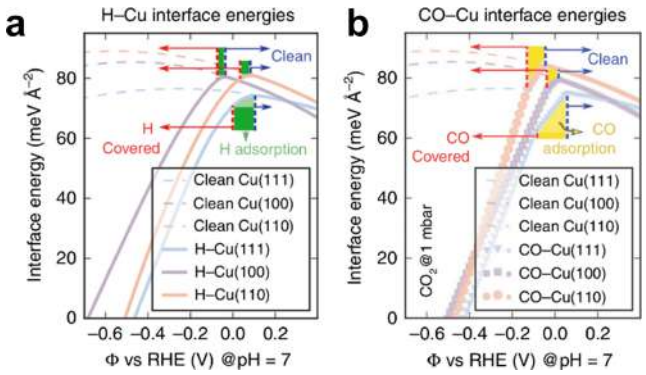

Figure 7: a-b, Grand potential interface energies calculated for H-covered and CO-covered Cu surfaces in aqueous solution.[100] Adapted with permission from Ref. 100 (Copyright 2018 Springer Nature under Creative Commons Attribution 4.0 International License[157]).

In a following study in collaboration with our group,[63] the application of a graphene-layer on top of polycrystalline copper accounted for a different reconstruction process. After 4 hours, polarization at −1.0 V vs SHE in a 0.1 M $KHCO_3$ electrolyte, *Operando* EC-STM and Raman spectroscopy revealed the evolution of pc-Cu to copper nanocuboids.[63] Suggesting a minor, likely kinetic effect of reaction intermediates due to the protective graphene overlayer, the authors rationalized the nanostructuring process through sole electrostatic considerations. In the modeling section, we explicitly induced electric field on the chosen copper surfaces *via* a dipole correction,[231,232] as described in the DFT datasets generated and stored in the ioChem-BD database.[233] Thus, by modeling the electrical double layer as

a parallel plane capacitor under the assumptions of high polarization and large electrolyte concentration,[2] we derived a dependence of copper surface energy γ on applied electric field $\vec{E}$ and solvent dielectric permittivity, ϵ_{r}.[63] The intensity of $\vec{E}$, modulated by ϵ_{r}, determines an increased electronic density at the surface, thus stabilizing the overall system. Open facets as Cu(100) and Cu(110) can better accommodate electronic density than (111) due to the lower coordination of their surface sites.[232] Thus, upon application of high cathodic bias, these domains are more stable than close-packed domains. Finally, surface morphologies with shorter radius of curvature experience a higher electric potential, thus boosting the reconstruction even further.

Analogous thermodynamic considerations can be applied as well to assess the stability of nanoparticles (NPs). According to the Wulff theorem, at standard conditions the most abundant facet on a nanoparticle is the one which presents the lowest surface energy.[234] Thus, by estimating surface energies of different crystalline domains, it is possible to represent nanoparticles through their Wulff construction.[235] However, under reaction conditions, Ostwald ripening and degradation mechanisms can occur along with the formation of complexes at the surface. The window of stability of nanoparticles can be estimated following the theoretical framework developed by Ouyang *et al.*[236] For instance, considering the case of Ni nanoparticles on N-doped supports under eCO_2R conditions, the Gibbs free energy of disintegration $\Delta G^{\mathrm{dis}}_{\mathrm{NP}}$ toward $Ni(CO)_x$ was computed depending on the nanoparticle radius, temperature, and pressure, Equation 14.[237] $E^{\mathrm{f}}_{\text{surf-}n\mathrm{CO}}$ represents the energy of the Ni center on carbon support coordinated to n CO molecules, $\Delta\mu$ is the excess chemical potential of CO, $\Delta E'_{\mathrm{NP}}(R)$ is the energy of the CO-covered nanoparticle, R, T, p, and S are respectively radius, temperature, pressure, and entropy. By comparing $\Delta G^{\mathrm{dis}}_{\mathrm{NP}}$ with the energy of an isolated Ni adatom, Pršlja *et al.* concluded that at very high coverage ($\theta_{*\mathrm{CO}} = 1.00$ ML) and close to standard conditions ($T = 300$ K, $p = 0.1$ mbar), Ni nanoparticles smaller than 4 nm naturally disintegrate into $Ni(CO_2)$ complexes.[237,238]

$$\Delta G^{\mathrm{dis}}_{\mathrm{NP}}(R,T,p) = E^{\mathrm{f}}_{\text{surf-}n\mathrm{CO}} - n \cdot \Delta\mu_{\mathrm{CO}}(T,P) - \Delta E'_{\mathrm{NP}}(R) - TS \tag{14}$$

Extending those concepts to HER, a similar thermodynamic approach was employed to elucidate the occurrence of the so-called "third hydrogen peak" in the cyclic voltammograms on Pt electrodes at +0.22 V vs RHE.[208] This feature has been linked to (110) steps sites, (111) terraces, or (110)-(2 × 1) domains through accurate studies on single crystal surfaces.[239–241] McCrum *et al.* calculated the surface energies of Pt(553) and Pt(533) characterized respectively by (111) terraces with (110) and (100) steps in presence of adsorbed hydrogen. The onset potentials for hydrogen adsorption on the (110) and (100) edges was calculated as +0.46 eV and +0.56 eV for Pt(553) and Pt(533) respectively. Overall, this process was more favorable on steps rather that (111) terraces due to the lower coordination number of these defects.[83–85] The authors observed that by applying more negative potential, hydrogen adsorption becomes thermodynamically favorable on the terraces as well and *H coverage increases. Consequently, the surface energy of the overall system decreases and the gradient of such effect depends on the number of electrons transferred per unit area, *i.e.* on hydrogen coverage (Figure 8).[208] The surface energy γ of the system in presence of H adsorption was calculated through Equation 15. G_x are the Gibbs free energy of adsorbed hydrogen (*H), clean surface (*), and 1/2 hydrogen molecule ($\frac{1}{2}\mathrm{H_2}$), U is the applied potential vs RHE, U_{pzc} is the potential of zero charge, $\vec{p}_x$ are the electric dipole moments for adsorbed hydrogen (*H) and clean surface (*), d is the thickness of the double layer, and A is the geometric area of the surface.

$$\gamma(U_{\mathrm{RHE}}) = \gamma(U_{\mathrm{RHE}} = 0\ \mathrm{V}) + \frac{G_{*\mathrm{H}} - G_{*} - G_{\frac{1}{2}\mathrm{H_2}} + |\mathrm{e}^-|U + |\mathrm{e}^-|(U - U_{\mathrm{pzc}})\frac{\vec{p}_{*\mathrm{H}} - \vec{p}_{*}}{d}}{A} \tag{15}$$

The surface energies of the roughened facets, labeled as Pt(553)-SER and Pt(533)-SER, decrease as well under more negative potential. These systems were modeled starting from

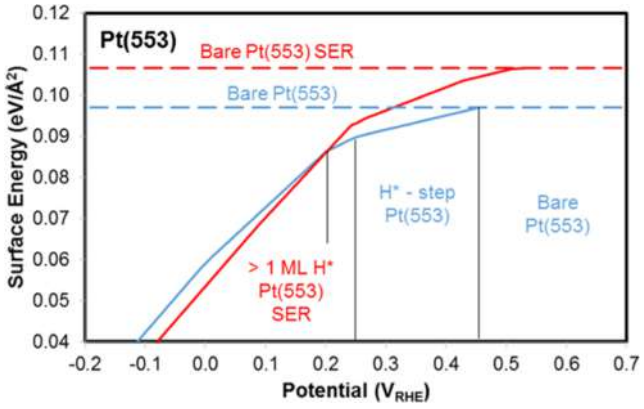

Figure 8: Surface energy of the pristine and roughened (denoted as SER) Pt(553) facet with (solid lines) and without (dashed lines) *H. Changes in surface energies slope are due to variation in hydrogen coverage, as indicated as insets.[208] Adapted with permission from Ref. 208 (Copyright 2019 American Chemical Society).

a pristine surface, either Pt(553) or Pt(533), with 1/3 of the step atoms translated to the minimum energy adsorption site close by. Thus, this corner at the edges showed opposite crystalline facet than the pristine steps: (100) for Pt(553)-SER, whilst a (110) for Pt(533)-SER. Since the (100) corner has lower coordination than the pristine (110) step-edges sites, this site binds hydrogen stronger and thus Pt(553)-SER presents a lower surface energy that Pt(553) from +0.20 V vs RHE (Figure 8). Thus, below this critical bias, the pristine (533) facet naturally reconstructs to its roughened form, giving rise to the experimental peak observed at +0.22 V vs RHE. Instead, this process is not favorable on Pt(533), since the pristine (100) step-edges sites on Pt(533) adsorb H strongly than the reconstructed (110) corner, thus Pt(533) is more stable than Pt(533)-SER for any applied potential. Kinetic studies further confirmed the crucial role of hydrogen coverage to drive platinum reconstruction. The concerted translation of two neighboring Pt − the first to create the corner and the second to fill the vacancy created − is kinetically hindered by a high activation barrier of 1.75 eV in absence of hydrogen. Instead, at high *H coverage such kinetic barrier decreases to 0.93 eV and the reaction is exergonic. Thus, H adsorption leads to a reduction of the kinetic barrier > 0.8 eV, yielding rates observable experimentally.

4.2 Modeling *Operando* surface reconstruction

Metastable phases or kinetically trapped ensembles stand at the core of electrocatalytic reactivity.[207] Albeit their thermodynamic instability, configurational entropy or kinetic processes can locally stabilize these actives sites,[204,242,243] leading to enhanced activity and selectivity.[244,245] For instance, stability and role of polarized sites is a crucial dilemma in the field of eCO_2R, following the first observation by Kanan and Li of the enhanced activity of a Cu_2O-derived catalyst.[108] Even though copper is expected to be fully metallic under cathodic bias,[246–248] many direct and indirect experimental evidences hint at the presence of either kinetically trapped or metastable active sites under reduction conditions.[14,111,202,206,249–258] Thus, further insights from theory are needed and DFT modeling on crystalline surfaces is unable to fully reproduce the experimental data.[205,259,260]

We report here two possible approaches to mimic the complexity of copper surfaces under eCO_2R conditions, respectively (1) *ab initio* molecular dynamics (MD) modeling,[261] and (2) methodologies based on machine learning (ML) techniques (Section 8).[262] The outcomes from DFT-MD simulations must be properly validated by experimental evidences, since commonly employed thermostats may lead to non physical temperature variations and large temperature gradients within the simulation cells.[212] Instead, the ML strategy will likely play a determinant role in the future, as can be easily extended as well to the stability of other components of electrocatalytic devices, such as membranes for fuel cells for instance.[263] Besides, alternative methods can serve the scope, as effective medium theory[264,265]which was recently employed to mimic surface roughening on copper electrodes derived from cuprous oxide, phosphide, nitride, and sulfide precursors.[266] As a last remark to guide the reader, in this section we limit the discussion to methodology and structural properties, while we cover the insights on active sites and local polarization effects in Sections 4.3 and 4.4 respectively.

The first study which aimed at reproducing reconstruction on an oxide-derived model employed an *ab initio* molecular dynamics (AIMD) approach. Since subsurface oxygen was calculated to be unstable on a crystalline slab system in contrast with experimental obser-

vations,[202,203] Liu *et al.* assessed a disordered Cu_2O-derived nanocube.[205] By employing a Self-Consistent Charge Density Functional Tight Binding scheme (SCC-DFTB),[267] they initially built a $(5\times5\times5)$ Cu_2O supercell accounting for 1.7 nm width and composed of 500 Cu atoms and 250 O atoms (Figure 9a). To simulate reduction processes occurring at cathodic bias, the surface oxygens were fully depleted. Besides, oxygen atoms within the two outermost layers were removed ten at a time, and after each removal a structural optimization was performed until no oxygen atoms were exposed. The resulting systems, which accounted for 500 Cu and 91 O, underwent a minima hopping algorithm with an initial NVE molecular dynamics temperature of 500 K for 50 cycles with 1 fs time step.[268] Oxygen diffusion from subsurface sites to the surface was tested within the SCC-DFTB framework, suggesting that such process is hindered on the distorted nanocube geometry. Migration of oxygens to the surface was possible only for edge and corner subsurface sites, however these configurations were endothermic, thus confirming the overall stability of subsurface oxygens.

Recently, we applied a similar strategy, albeit in a more systematic manner.[210] Since OD-Cu is usually synthesized either through oxidation of copper foils or electrochemical reduction of copper oxides,[109,247] we built two classes of model to mimic these regimes, labelled respectively red-Cu_2O and oxi-Cu (Figure 9b). The red-Cu_2O class was derived from a pristine $(2\sqrt{3}\times2\sqrt{3})$-$R30°$ $Cu_2O(111)$ supercell with 2.1 nm lateral size. We fully depleted the outermost oxygen layer (12/144) and we partially removed subsurface oxygens (4-6/144). The elimination of subsurface oxygen was done following three geometric shapes, rhomboidal (R), triangular (T), and linear (L) to enhance clustering, pitting, and formation of grain boundaries. The three resulting nS systems were characterized by equivalent suboxide formation energy within 0.01 eV per Cu atom (n = number of subsurface oxygen removed; S = elimination motif). The simulated O content, 30-31 at.%, was higher than values reported experimentally (10-20%),[111,112] due to contribution from the bulk oxide. Besides, a 7 layers-thick symmetric slab (SY-red-Cu_2O) was employed to model deep reduction conditions, after having depleted all the oxygens within the three outermost Cu_2O layers

from each side (120/168, O content of 13 at.%, Figure 9b). Finally, systems mimicking copper oxidation were obtained by depositing three Cu_2O layer on a $(5\sqrt{3}\times5\sqrt{3})$-$R30°$ Cu(111) matrix and removing surface and subsurface oxygens according to the protocol previously defined (11 at.% O, Figure 9b). Analogously, these three systems were isoenergetic within 0.01 eV. The seven simulated models underwent AIMD simulations with the PBE density functional (Ref. 269) for 10 ps at 700 K (3 fs time steps with a canonical ensemble, NVT, Nosé-Hoover thermostat).[261,270] The full AIMD trajectories are freely available on the open-source ioChem-BD database.[271] Benchmark tests with a Hubbard correction $U_{\text{eff}} = U - J = 7 - 1$ eV on the d orbital of Cu,[272–276] and different AIMD temperatures (300 K, 500 K) confirmed the robustness of the computational setup. As a proof of agreement with experimental data, simulated STM images of the reconstructed surfaces resembled experimental observations on Cu_2O/Cu(111) materials under CO autocatalytic reduction.[277] Secondly, the overall atomic roughness for our models was significantly higher than crystalline Cu (0.8-1.4 Å vs 0.32 Å, respectively).[210,278] Finally, both simulated Cu 2p and O 1s features,[279,280] as well as Raman spectra,[281] agreed with the experimental reports.[202,251,282–284]

Previously, Huang *et al.* employed a different approach, which combined DFT with Grand Canonical techniques and an artificial Neural Network (NN) to investigate Cu nanoparticles.[213] As-synthesized nanoparticles cannot be explicitly model through DFT simulations due to computational limits, since 10 nm NP accounts for $\sim$ 200000 atoms and $\sim$ 10000 surface sites. Thus, the authors designed the copper nanoparticle through the reactive force field framework (ReaxFF) developed earlier,[285–287] and the semi-empirical embedded-atom model to model interactions between copper atoms.[288] To simulate chemical vapor deposition, copper atoms were subsequently introduced in the computational system at a rate of 3.2 atoms per ns for 30 ns. Later, 38 annealing cycles were simulated to optimize the structure. Each cycle consisted of a temperature ramp from 300 K till 1200 K (5 ps), 5 ps stabilization at 1200 K, cooling down to 300 K (5 ps). Finally, the resulting system was relaxed through ReaxFF for 20 ps at 300 K. Up to 400 random sites were chosen from the

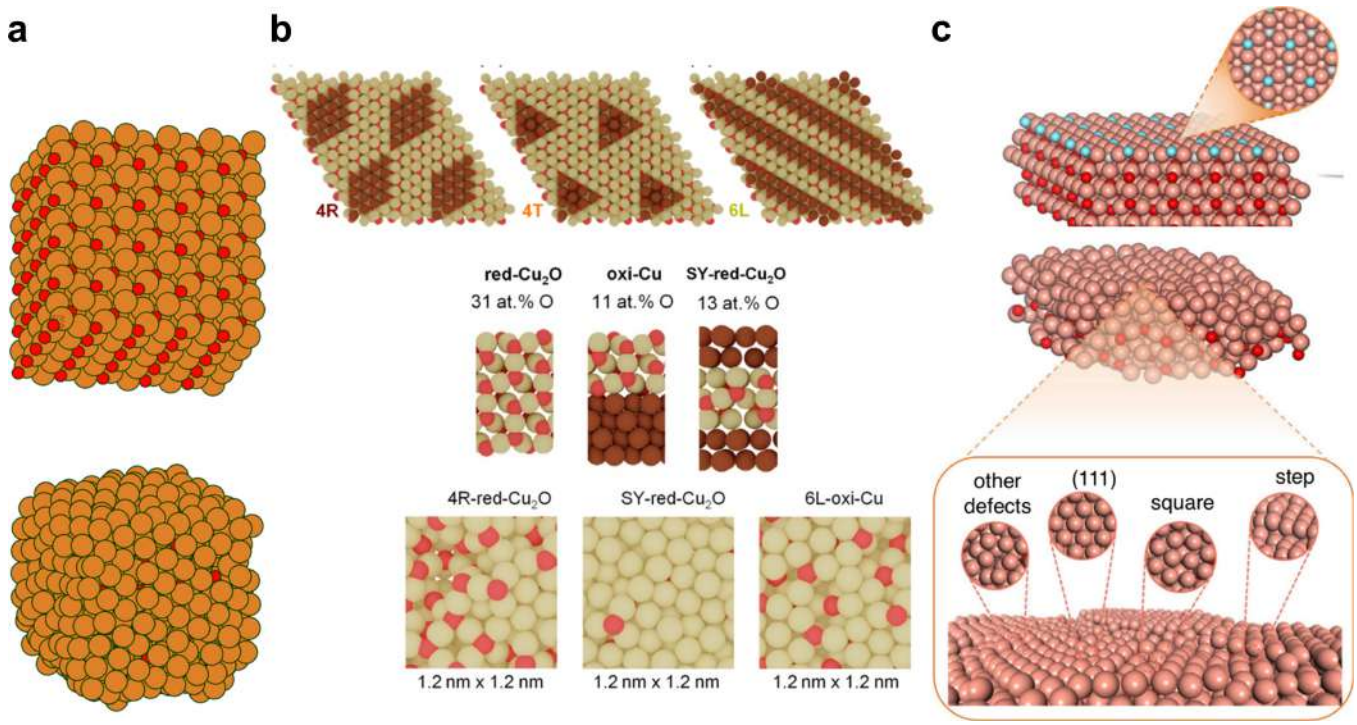

Figure 9: Molecular dynamics-based approaches to reproduce surface reconstruction occurring for oxide-derived copper catalysts under operation. Depending on the oxygen content, different surface motifs are reproducible. **a**, OD-Cu nanocube containing 250 unit cells initially, then manually reduced to 500 Cu (brown) and 91 O (red) atoms prior to apply minima hopping.[205] **b**, Partially oxidic phases for O-lean surfaces.[210] Red and light/dark brown highlight oxygen and oxidic/metallic copper atoms, respectively. **c**, Defective Cu facets for O-free surfaces.[211] Red and brown atoms represent O and Cu, respectively, whilst light blue atoms highlight the surface oxygens initially removed. Adapted with permission from Ref. 205 (Copyright 2017 American Chemical Society), Ref. 210 (Copyright 2020 American Chemical Society), and Ref. 211 (Copyright 2021 Springer Nature under Creative Commons Attribution 4.0 International License[157]) respectively.

final structure and the local environment of each site up to 8 Å was integrated into a neural network. Each neighboring atom was transformed into a 12 two-body and 18 three-body molecular descriptors for a 2-layer NN with 50 nodes in each layer. The 400 sites were further partitioned into training, validation and test sets with an 8:1:1 ratio.

Later, Cheng *et al.* developed a framework integrating molecular dynamics and a neural network potential (NN-MD)[289] to assess the reconstruction occurring on a oxygen-lean copper material.[211] Initially, the whole surface oxygen layer was depleted from a pristine $Cu_2O(111)$, since previous studies suggested oxygens to be unstable at the electrode/electrolyte

interface under CO_2R conditions (Figure 9c).[247,290] Then, the resulting system underwent NN-MD for 1 ns at 300 K to mimic the first stage of the reduction process. Since some of the subsurface oxygens migrated to the surface, O atoms with lower vacancy formation energy and coordination number 3 were removed, since they are expected to be the least stable during reduction. An additional 1 ns NN-MD was carried out and the previous step was repeated until no surface oxygen was present to derive six different OD-Cu models. The surface morphology largely evolved, accounting for (111) facets ($\sim$ 53%), square domains ($\sim$ 12%), steps ($\sim$ 16%), and other defects ($\sim$ 19%), see Figure 9c.[211]

The above mentioned methodologies are applicable as well to assess reconstruction processes for other electrocatalytic reactions, as the effect of potential dopants on catalytic performance for OER. For instance, in our group we have studied the formation of NiO_xH_y phases under OER conditions.[54,291] Based on computed Pourbaix diagrams, a NiO_xH_y catalyst is expected to evolve to the γ-$Ni(OH)_2$ phase when in contact with water solution. Besides, a successive transition to γ-NiOOH is envisioned when a positive potential is applied.[54,292] These phase transitions happen concurrently with water intercalation.[293–295] In fact, due to strong water adsorption and H-bonds, a NiOOH surface fully covered by water molecules results in a negative surface energy. This indicates that the water will intercalate between NiOOH layers, which agrees with the volume expansion observed in experimental studies.[293–295] When Fe is introduced in the system as dopant, the Fe^{2+}/Fe^{3+} ions may also penetrate into nickel layers further increasing layer-layer distance and active inner surface. Consequently, the surface of a Fe-doped NiO_xH_y electrode in water solution is expected to become gel-like under work conditions. Through AIMD simulations, we found that the adsorption of iron ions on the NiOOH surface is stable. However, we observed that the local chemical environment of Fe ions, such as the number of coordinated water molecules, is dynamic, as shown in Figure 10. Water molecules coordinated with iron ions frequently exchange their proton (coupled with electron) with oxygen at the catalytic surface. This behavior dynamically changes the oxidation state of Fe and further enables more flexible va-

lence state of Ni ions, from Ni^{3+} to Ni^{2+}, lowering the overall potential for oxygen evolution to 0.23 V.

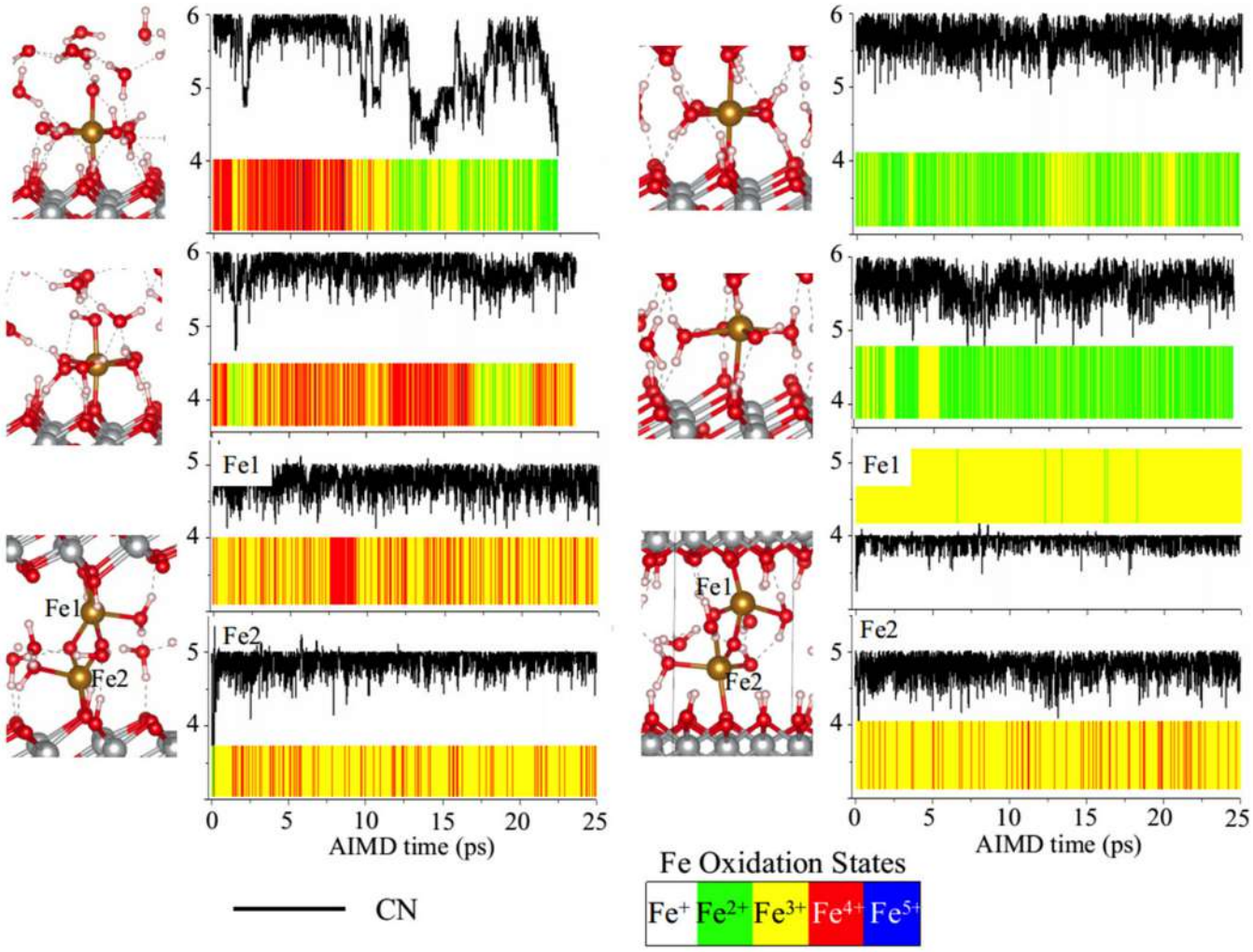

Figure 10: Evolution of coordination numbers (CNs) and oxidation states (OSs) of Fe ion adsorbed and/or intercalated for different Ni-based (oxy-)hydroxide models (NiO_xH_y) during AIMD simulations.[54,291] Figures adapted with permission from Ref. 54 (Copyright 2020 American Chemical Society).

4.3 Identification of active sites

In addition to properly reproduce morphological changes at the surface, the methodologies described in Section 4.2 enable the identification of crucial surface ensembles and active sites responsible for the catalytic performance.[205,210,211,213]

The AIMD-based study on oxygen-lean Cu_2O catalysts (Figure 9a, Section 4.2) highlighted the presence of copper in three well-defined structural and electronic states: metallic Cu^0, suboxidic $Cu^{\delta+}$, and oxidic Cu^+, respectively coordinated with 0, 1, and 2 oxygen atoms.[210] Remarkably, suboxidic $Cu_2O_{0.5}$ ensembles have been observed experimentally,[206,255,256] and reported with an average Cu-O coordination number of 1.1 estimated through EXAFS,[256] confirming theoretical predictions. While metallic and oxidic copper exhibited the typical oxidation states of bulk Cu and Cu_2O, suboxidic Cu accounted for a Bader charge between 0.1 and 0.4 $|e^-|$, in line with experimental evidence of formation of polarized $Cu^{\delta+}$ sites during thermal and electrochemical reactions.[206,255,256] Besides, all the three copper species were significantly undercoordinated if compared to surface atoms on crystalline facets and each oxygen coordination further lowered Cu-Cu coordination number by one unit. Thus, average $\bar{N}_{\text{Cu-Cu}}$ of 4.9, 3.6, and 2.0 units for Cu^0, $Cu^{\delta+}$, and Cu^+ were estimated from these OD-Cu models, showing good agreement with experimental characterization of OD-Cu (respectively 6.6, 3.08, and 2.21).[256,296] The abundance of residual Cu^+ species within the surface layers ranged between 10 and 40 at.% (for red-Cu_2O and oxi-Cu classes respectively), in line with recent experimental observations on Cu_2O nanocubes at -0.95 V vs RHE (20 at% Cu^+)[258] and Cu(100) under pulsed CO_2 electroreduction (7-11 at.% at -1 V vs RHE).[14] Finally, sampling the occurrence of interatomic angles for a given central species (Cu^0, $Cu^{\delta+}$, Cu^+, and O), we detected 14 recurrent ensembles. Darker areas in the 2D histogram reported in Figure 11a correspond to higher density of similar structural morphology. By mapping recurrent angles with geometric patterns visible on the reconstructed surfaces, we characterized surface defects (4- and 6-coordinated copper adatoms) and crystalline reconstructions toward (100), (110), and (111) facets, either fully metallic or partially polarized. These observations closely agree with experimental reports on surface reconstruction toward open facets,[63,100,102,223] as well as high surface density of defects.[14,112,195,199] Finally, a remarkable $Cu_3^{\delta+}O_3$ feature appeared at the surface, which was characterized in an independent experimental work.[255] As for oxygen species, subsurface

configurations adopted the bulk-like tetrahedral shapes, $O_{4Cu,t}$ as well as possible distorted 3- and 5-fold coordinations, $O_{3Cu,d}$ and O_{5Cu}. Remarkably, few oxygens reconstruct toward planar configurations near the surface, $O_{3Cu,p}$ and $O_{4Cu,p}$, and may be the species found stable as a $Cu_2O_{0.5}$ stoichiometry for a $Cu(OH)_2$-derived electrode under CO_2 reduction conditions at -1.0 V vs RHE.[256]

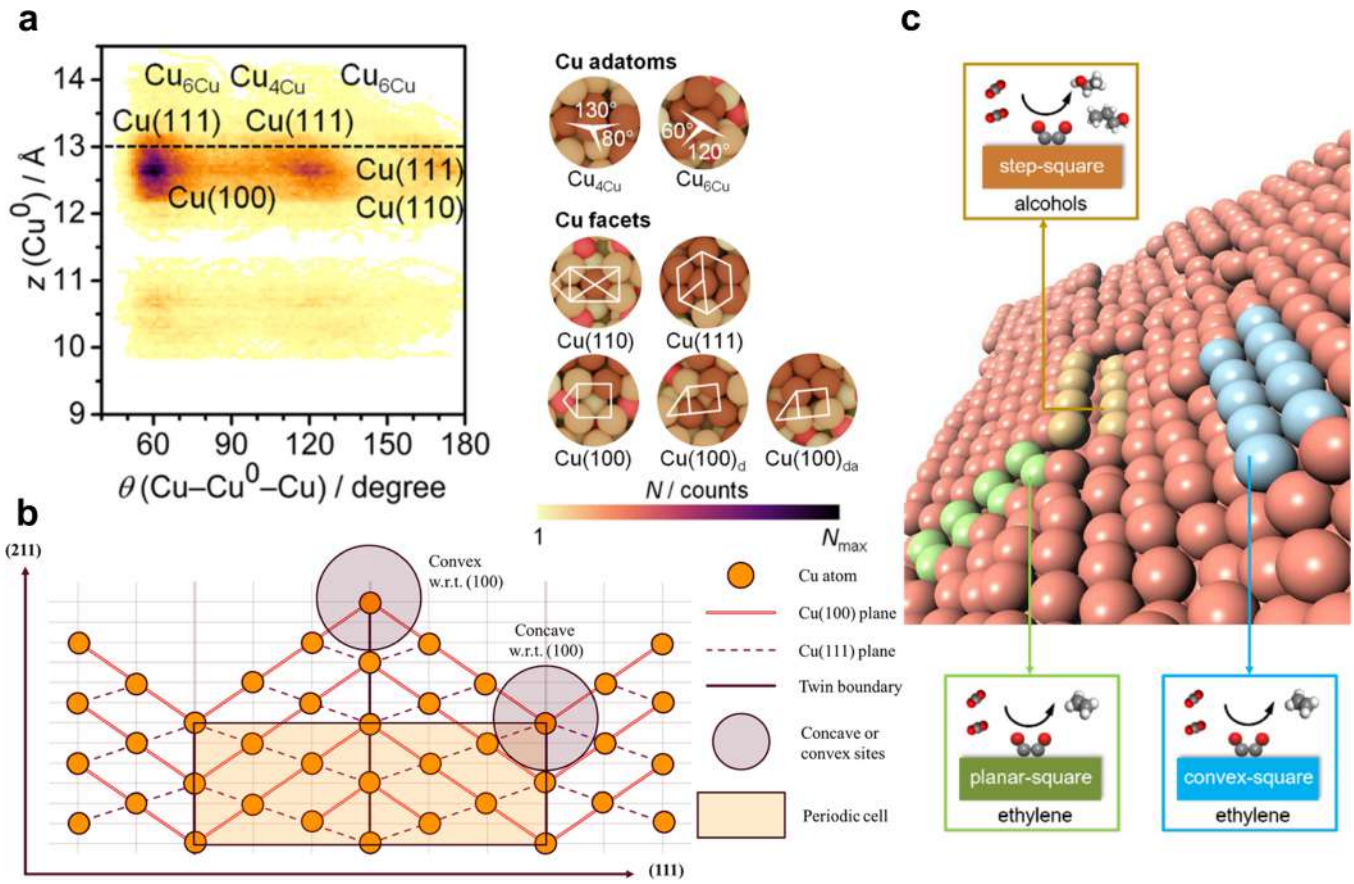

Figure 11: Relevant ensembles identified on OD-Cu and Cu models. **a**, Recurrent surface ensembles on O-lean OD-Cu structures (Figure 9a), defined by the local geometry of a given Cu cluster.[210] Oxygen atoms are shown in red, whilst copper is depicted in brown, from dark (Cu^0) to light (Cu^+) depending on its oxidation state. **b**, Theoretically-designed FCC copper containing (100) and (111) planes, as well as twin boundaries.[213] **c**, On a O-free OD-Cu surface (Figure 9c), step-square (dark yellow), planar-square (green), and convex-square (light blue) domains were characterized and related to alcohols and ethylene formation.[211] Adapted with permission from Ref. 210 (Copyright 2020 American Chemical Society), Ref. 213 (Copyright 2018 American Chemical Society), and Ref. 211 (Copyright 2021 Springer Nature under Creative Commons Attribution 4.0 International License[157]) respectively.

To assess a small sample of their computationally designed copper nanoparticle (Section

4.2),[213] scientists from Prof. Goddard III's group selected 400 surface sites and calculated CO binding energy on these active species through their reactive force field framework, ReaxFF (Refs. 285–287). Further, they extrapolated the corresponding values for all the 10000 surface sites of their original NP *via* the NN trained during the study. As a result, they identified specific active sites with stronger binding than low crystalline facets, *i.e.* (100) and (211), in line with previous TPD experiments on copper.[297] Then, applying the formation energy of the protonated CO dimer, *OCCOH, as a potential descriptor for C_{2+} selectivity, they observed that square motifs similar to (100) accounted for favorable binding of this intermediate. Assessing the local geometry of the favorable square domains, a specific (100) terrace coupled to (111) was reported to further enhance this process, in agreement with experimental observations on the promoting effect of Cu(S)[n(100) × (111)].[35,36,298] As a final guideline to catalytic design synthesis, the authors proposed a periodic FCC copper structure with high surface density of this (111)-(100) motif as a promising active ensemble for increasing C_{2+} formation (Figure 11b), since it showed the most favorable formation energy for OCCOH (0.35 eV and 0.41 eV either on convex or concave sites). This devised catalyst was predicted to grant 97% F.E. toward multi-carbon products, assuming a linear correlation between density of twin boundaries and C_{2+} selectivity and no influence on HER.

Identification of the active sites on the O-lean OD-Cu developed with the NN-MD methodology (Figure 9c, Section 4.2)[211] and correlation with eCO_2R selectivity was achieved following a reductionist approach alike the previous study.[213] The authors selected 155 surfaces sites out of the reconstructed slabs and calculated *CO and *COCO binding energy for these active centers *via* the NN potential.[289,299] The robustness of the NN potential was confirmed by benchmark tests through single-points DFT simulations, which returned low systematic offset of 0.08 eV and 0.13 eV for $\Delta E_{*\mathrm{CO}}$ and $\Delta E_{*\mathrm{COCO}}$ respectively. The CO dimer was chosen since it is generally assumed as the RDS toward formation of multicarbon products on copper.[16] In line with the results from Huang *et al.*,[213] square motifs exhibited the strongest *COCO binding energy, accounting for an average energy cost for C-C

coupling of 1.27 eV. This conclusion agrees with an earlier theoretical study by Bagger *et al.*[39] and experimental insights from Hori *et al.* (Section 2.1).[35,36] By further differentiating between the squared domains, Cheng *et al.* characterized four surface motifs: planar-square (p-sq), step-square (s-sq), concave-square (cc-sq), and convex-square (cv-sq) facets, which were extracted as slab models to calculate the energetics of CO dimerization through accurate DFT simulations. All structures allowed for a less endothermic C-C coupling in comparison to (111) and (211) facets. Besides, p-sq, s-sq, and cv-sq sites permitted a facile kinetics, with an activation barrier lower than 0.7 eV vs 0.85/1.19 eV on the crystalline domains. C_{2+} selectivity of these ensembles was mapped according to their $*CH_2CHO$ adsorption energy, since this adsorbate is expected to be the intermediate ruling competition between ethanol and ethylene.[16,143,300] The authors observed that planar and convex squares promote the cleavage of the C-O toward ethylene, whilst step-square resembling Cu(S)-$[n(111) \times (100)]$ motifs inhibit the hydrocarbon pathway (Figure 11c), in good agreement with previous experimental and theoretical suggestions.[35,36,39] The different surface reactivity was rationalized through considerations on the local morphology. p-sq and cv-sq can stabilize *O after C-O bond breaking on 4-fold sites, whilst the s-sq cleaving presents the lowest coordination number,[83,83,84] thus the strongest binding of the acetaldehyde intermediate which enables its further protonation. Additionally, C-O bond length was employed as descriptor for ethylene and ethanol selectivities. As expected, a shorter bond length is representative of a stronger bond, which consequently hinders C-O breaking, favoring formation of C_2H_5OH. Finally, the authors extended their theoretical framework by comparing performance of experimentally annealed OD-Cu with models obtained with different AIMD temperature ramps. Remarkably, C_{2+} current density correlated with the atomic ratio of the three identified ensembles (p-sq, cv-sq, s-sq) estimated for the AIMD-annealed slabs. eCO_2R activity toward ethylene and alcohols exhibited a linear dependence on (p-sq+cv-sq) and (s-sq) atomic contents respectively, confirming the selectivity of step-square domains toward ethanol and planar/concave-square morphology toward C_2H_4. However, according

to both theoretical and experimental observations, the highest density of actives sites, and consequently highest performance of the catalyst, was achieved for the non-annealed Cu_2O catalyst, whilst thermal treatments worsened both parameters.[211]

4.4 Surface polarization effects

As demonstrated through the *d*-band model,[74,75] surface reactivity of transition metals depends on their *d*-band center calculated with respect to their Fermi energy, *i.e.* a proxy of the degree of filling of the *d*-band (Section 2.2). In general, the capability of a catalytic center to bind intermediates is driven by its local electronic density. For cathodic reactions, low-coordinated surface defects exhibit stronger binding of the reaction intermediates due to their higher electronic density, resulting in tLSR based on average coordination numbers (Section 2.2.4).[83–85] In fact, the electronic density at the surface correlates with the effective potential, *i.e.* applied potential vs the potential at the point of zero charge (PZC).[2,63,171,208] Besides, undercoordinated sites are locally more charged due to their higher local curvature, as predicted by Green's theorem.[63,301] In addition to local variations of surface electronic density, the applied potential leads to the build-up of the electrochemical double layer, so that local electrostatic interactions can further stabilize or destabilize reaction intermediates.[44]

According to the Computational Hydrogen Electrode,[8] electric field/adsorbate electric dipole interaction can be estimated by a $\vec{p} \cdot \vec{E}_{\mathrm{EDL}}$ term which is added to the adsorption energy of the intermediate (Section 2.2.2). Following this concept, average electronic density at the surface, proxy of the effective electric field across the EDL, is a key factor to tune formation energies of specific compounds, as shown in Figure 12a for *CO, *COOH, and $*CO_2$ adsorption during CO_2 reduction.[166] On top of these average fields effect, local electrostatic phenomena are expected to play a crucial role in triggering catalytic activity for eCO_2R on otherwise inactive catalysts.[42,45,97] In fact, recent theoretical and experimental observations pointed out that dopants may further tune the local polarization of surface sites, so that limitations from tLSR can be overcome due to the formation of active sites with significantly

different electronic properties. For instance, we rationalized the enhanced eCO_2R selectivity of S-doped copper toward formate through local electronic effects.[302,303] As an adatom, since S is more electronegative than Cu, it withdraws electronic density from the neighboring copper sites and thus acts as a tethering center to adsorb either CO_2 or a hydride. Then, adsorbed CO_2 selectively reduces to formate upon protonation of the C atom, whilst the *H pathway undergoes an Heyrovský-like mechanism to the same product (Section 5.2, Figure 15). The negative charges localized on S is instrumental to enable both processes and to limit unselective eCO_2R pathways on neighboring copper sites. Instead, positively charged surface sites are expected to influence reactivity in an opposite manner. $Sn^{\delta+}$ sites in Cu-Sn alloys were predicted to weaken *COOH and *CO binding energy, thus leading to enhanced selectivity toward formate and CO depending on Sn/Cu ratio.[304–306] Cu^+-Cu^0 pair have been deemed responsible for the enhanced C_{2+} selectivity of OD-Cu materials.[307,308] Recently, a joint experimental and theoretical study employed TPD, *in situ* Attenuated Total Reflection Fourier Transform Infrared spectroscopy (ATR-FTIR), and DFT to suggest that strongly bound, bridge-adsorbed CO (CO_B) is a precursor for methane formation, whilst a Cu^+ site accounts for weaker binding of linearly adsorbed CO, enabling CO dimerization to ethylene.[257] A similar weakening effect of polarized sites on binding energy was reported by Ismail *et al.*,[309,310] on a Au/Pb interface, where subsurface oxygens dopants hindered poisoning of the Pb surface, thus allowing formation of methane. An analogous electrostatic repulsion between positively charged surface atoms and adsorbates has been mentioned for a In-Pd solid solution, where In substituents weaken *H and *CO binding energy due to their partial positive charge, $+0.64\ |e^-|$ estimated through Bader charge analysis.[311,312] Finally, similar tuning of eCO_2R selectivity due to surface polarization were proposed for nickel oxygenates.[97]

Recently, we have systematically assessed the influence of polarized sites on CO_2 reduction activity and selectivity on the AIMD-derived OD-Cu models discussed previously (Figure 9a, Section 4.2).[210,313] We observed Linear Scaling Relationships of $*CO_2$, *OCCO, and 2*CO

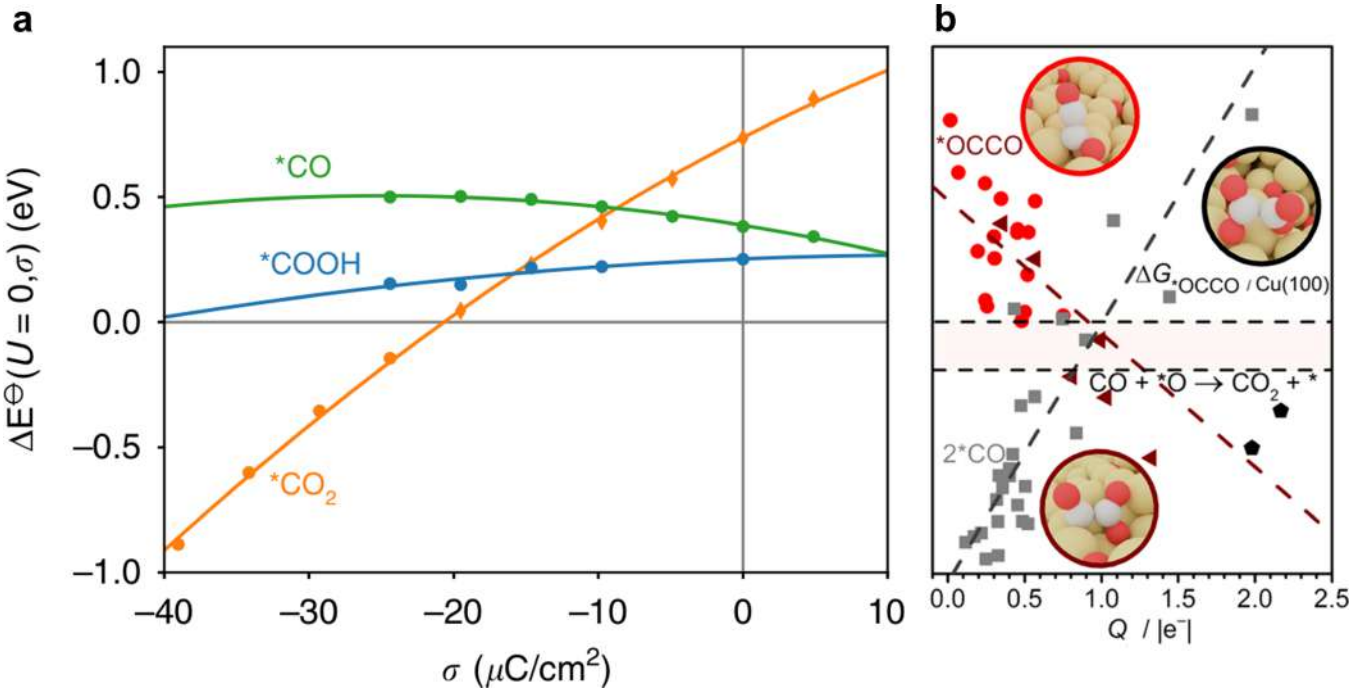

Figure 12: **a**, Formation energies for *CO_2 (orange), *COOH (blue), and *CO (green) on Au versus the surface charge density, taking CO_2, H_2O, and clean metallic surface as energy reference.[166] **b**, 2*CO and *OCCO formation energies as a function of surface polarization Q. An asymmetric OCCO dimer on metallic copper, deprotonated glyoxylate, and oxalate intermediate are reported as red, dark red, and black insets respectively. Q is defined as the sum of the absolute Bader charges of the active sites, Eqaution 17.[210] Adapted with permission from Ref. 166 (Copyright 2020 Springer Nature under Creative Commons Attribution 4.0 International License[157]) and Ref. 210 (Copyright 2020 American Chemical Society).

formation Gibbs free energies vs surface polarization Q (Equation 16, Figure 12b). Q was obtained as the sum of the absolute values of the Bader charges q of the active sites (X) binding O or C, Equation 17. Overall, ΔG_{*CO_2}, ΔG_{*OCCO}, and ΔG_{2*CO} exhibited different dependencies on Q, with $\beta < 0$ for intermediates adsorbed *via* a $\eta^2_{C,O}$ configuration (*CO_2, *OCCO) and $\beta > 0$ for adsorbates solely bound through the terminal carbons (2*CO).

$$\Delta G = \alpha + \beta Q \tag{16}$$

$$Q = \frac{1}{N_{X(C)}} \left| \sum_{i=1}^{N_{X(C)}} q_{X_i(C)} \right| + \frac{1}{N_{Y(O)}} \left| \sum_{i=1}^{N_{Y(O)}} q_{Y_i(O)} \right| \tag{17}$$

Overall, surface polarization strengthens the binding of $\eta^2_{C,O}$ configurations, whilst it leads

to a weaker binding of C-bound compounds. Following these principles, $*CO_2$ adsorption is increasingly stabilized by surface polarization, thus suggesting a triggering role of electrode charging for the enhanced eCO_2R activity of OD-Cu materials. Eventually, highly negatively charged sites such as near-surface oxygens (O_{ns}) can combine with strongly bond $*CO_2$ adsorbates to form carbonate species, which limit the overall activity of the system through surface poisoning.[121] On the contrary, adsorption of CO molecules as separate entities on the surface is destabilized by increased surface polarization, whilst *OCCO formation is increasingly promoted. Mildly polarized active sites, such as a O_{ns}-Cu couple, makes C-C coupling thermoneutral, thus enabling the possible formation of a deprotonated glyoxylate,[314] characterized by a low kinetic barrier (0.53 eV) (dark red inset in Figure 12b). This compound is a well-known intermediate for prebiotic CO_2 reduction,[315] although it has never been reported for the electrocatalytic counterpart.[146] Finally, high surface polarization characteristic of a O_{ns} pair can lead to formation of oxalates at the surface, which passivate the catalytic layer similarly as carbonate and may cause copper dissolution.

5 Reaction Pathways

The application of *Operando* techniques has evolved exponentially,[150,316] providing theoreticians with new challenges (Section 3.2), as only a direct mapping to computational structures allows for real insights into active sites and intermediates. Whilst initially spectroelectrochemical techniques could only shed light on catalytic properties under well-defined conditions or long-lived adsorbates on the surface, new advances have allowed to detect crucial, yet metastable reaction intermediates,[147–149,151] and to define complex reaction pathways and mechanisms.[151–153,317] In the incoming section, we review three recent works which highlight how systematic integration of spectroscopic and computational studies enabled the rationalization of the eCO_2 reaction mechanism (Section 5.1). Later, we describe the reaction routes for CO_2 reduction, hydrogen evolution, and oxygen evolution reactions (Sections 5.2-5.3.)

5.1 Spectroscopy-assisted identification of key reaction intermediates

A key step for deciphering the CO_2 reduction pathway puzzle was the identification of the RDS for C_{2+} formation, the $OCCO^-$ intermediate.[16] As observed by Hori *et al.*,[37] CO_2 (CO) reduction to ethylene is pH-independent, thus the rate-determining step for C_2H_4 formation must involve an electron transfer (Section 2.1). Since methane production is instead pH dependent,[37,141] the reaction pathways toward these two hydrocarbons must bifurcate at early stages. Whilst several studies suggested the formation of a negatively charged CO dimer as the RDS,[140,300] only a joint spectroscopic/DFT study could undeniably demonstrate the existence of this intermediate on the surface.[147] The authors observed two vibrational bands on Cu(100) in a ^{13}CO-saturated 0.1 M $LiOH/D_2O$ electrolyte from +0.1 to −0.15 V vs RHE, 1191 cm^{-1} and 1584 cm^{-1}, through *in situ* Fourier transform infrared (FTIR) spectroscopy, see Figure 13a. Transmission spectra of potential CO reduction intermediates as formaldehyde, formate, methanol, acetaldehyde, and acetic acid did not show compatible features, thus neglecting the assignment of these bands to other C-containing species. Finally, DFT-based vibrational analysis was crucial in identifying C-O-H and C=O stretching modes of a hydrogenated CO dimer (OCCOH) as responsible for the features observed (Figure 13b).

DFT vibrational analysis and *Operando* characterization can be further employed to provide mechanistic insights. In a recent collaboration with our group, computational modeling correctly reproduced experimental observations from *Operando* Surface Enhanced Raman Spectroscopy on CO_2 reduction on Cu_2O nanocubes. As introduced in Section 3.2, scientists from Prof. Roldán-Cuenya's research group observed a remarkable correlation between C_2H_4 selectivity and intensity ratio between Cu-CO stretching and CO rotation bands (Figure 14a).[153] By assessing different CO surface coverages on Cu *via* DFT and estimating the related CO vibrational frequencies, we demonstrated a correlation between computationally-estimated intensity ratio and theoretical CO surface coverage (Figure 14b),[318] in line with

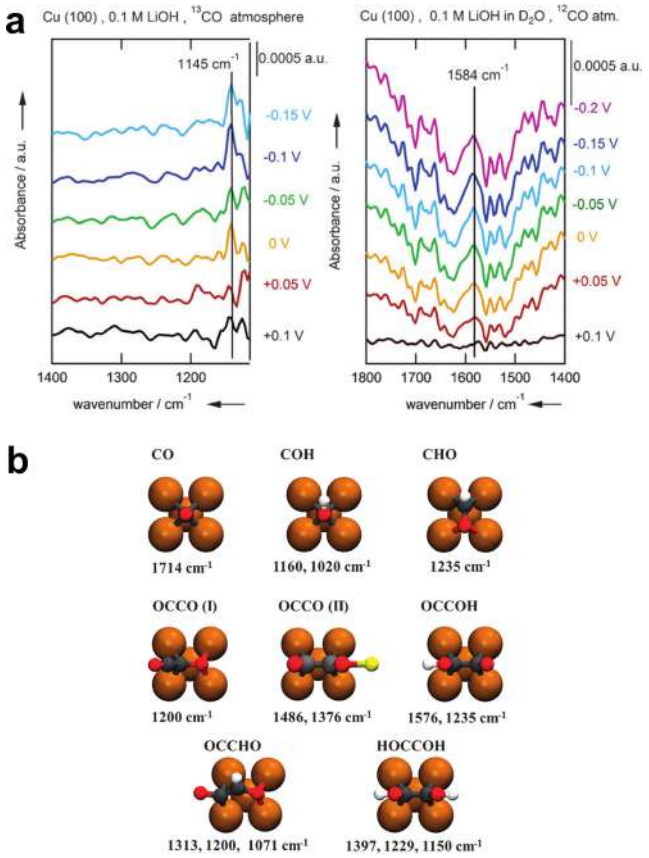

Figure 13: C-C coupling intermediate during CO reduction on Cu(100) observed and identified *via in situ* FTIR spectroscopy and DFT-based vibrational analysis. **a**, Spectra recorded on Cu(100) for a ^{13}CO-saturated D_2O electrolyte in 0.1M LiOH exhibits a 1145 cm^{-1} and 1584 cm^{-1} assigned to ^{13}C-OH and ^{12}C=O stretching bands. **b**, Among C_1 and C_2 intermediates, a single(double)-hydrogenated CO-CO dimer presents analogous DFT vibrational frequencies as observed experimentally.[147] Adapted with permission from Ref. 147 (Copyright 2017 Wiley-VCH).

experimental observations for different CO concentrations in the electrolyte. Furthermore, the more intense Cu-CO stretching band was attributed to weakly-bond CO adsorbed on top sites at high coverages, which showed the lowest activation barrier for CO-CO dimerization.

By assigning spectroscopic signals to adsorbed species on different catalysts, DFT-based vibrational analysis can define complex reaction pathways and descriptors for catalyst performance. Vibrational bands for CO_2 reduction on Cu, Au, and Pt were detected through *in situ* Surface Enhanced Infrared Absorption Spectroscopy (SEIRAS) at different applied potentials and later attributed to key reaction intermediates.[317] The authors observed a sin-

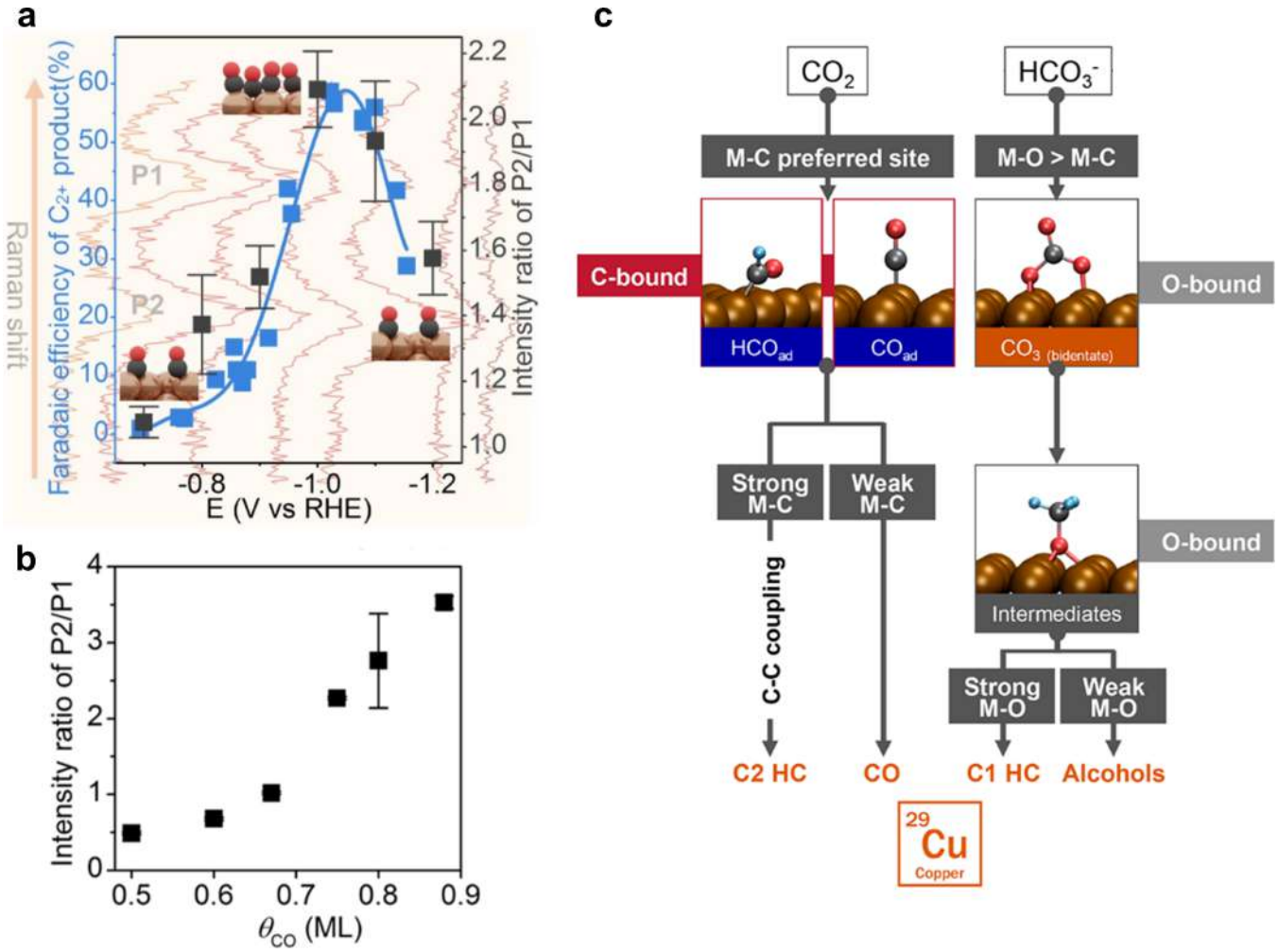

Figure 14: Unveiling reaction mechanisms and key intermediates with joint investigations involving density functional theory and *Operando* SERS. **a**, eCO_2 reduction to ethylene on Cu_2O-derived catalysts exhibits a peak at around $U = -1.0$ V vs RHE analogously to the ratio between Cu-CO stretching (P2) and CO rotation (P1) bands. **b**, Comparable P2/P1 ratio are reproduced *via* DFT for CO adsorption on Cu(100) at high coverage, suggesting a coverage driven C-C coupling mechanism.[153] **c**, eCO_2 reduction reaction mechanism on Cu defined through a joint *in situ* SERS/DFT-vibrational study.[317] Adapted with permission from Ref. 153 (Copyright 2021 American Chemical Society) and Ref. 317 (Copyright 2019 American Chemical Society).

gle signal for CO_2 reduction on Au, ~ 2100 cm^{-1}, which DFT ascribed to linearly-adsorbed CO. In fact only CO was produced at low cathodic bias (F.E. $> 50\%$ at -0.3 V vs RHE). Four vibrational bands were instead reported on Pt: 2074 and 1831 cm^{-1} for $U < +0.2$ V vs RHE); 1620 and 1376 cm^{-1} for anodic bias. DFT analysis attributed these signals to linearly-bond CO, CO on a bridge site, adsorbed COOH, and bidentate bicarbonate, respec-

tively. No eCO_2R reaction products were detected, in line with CO poisoning expected for Pt.[7] Finally on Cu, adsorbed species varied depending on the applied potential. Bidentate carbonate was indicated responsible for the band at 1495 cm^{-1} between +0.3 V vs RHE and −0.2 V vs. RHE, in good agreement with DFT calculations on Cu(100) and Cu(111) (1510 cm^{-1} and 1533 cm^{-1} respectively). O-bound intermediates such as $*OCH_3$ (1390 cm^{-1}), $*OCH_2CH_3$ (1340 cm^{-1}), and bidentate *HCOO (1240 cm^{-1}) were observed from +0.1 V vs RHE until −0.9 V vs RHE. Besides, vibrational features for *CHO (1477 cm^{-1}) and *CO ($\sim$ 1900 cm^{-1}) were detectable from −0.3 V vs RHE and −0.6 V vs RHE, respectively. With regard to the catalytic performance, mainly CO was formed at −0.3 V vs RHE (F.E. = 30%), whilst CO_2 reduction to formate (F.E. $\sim$ 15%) and ethylene (F.E. $\sim$ 20%) become relevant from −0.9 V vs RHE at expenses of CO. Since only *CHO and *CO were detected within this potential windows, these intermediates were deemed responsible for C-C dimerization on Cu. Finally, the authors rationalized Pt, Au, and Cu reactivity assuming the strength of M-O and M-C bonds (M = metal) as descriptor (Figure 14c). In the case of copper, sites with stronger C affinity preferentially catalyze C-C coupling, whilst a weaker C binding allows for CO production. Conversely, sites which absorb eCO_2R intermediates *via* a terminal oxygen are selective toward C_1 products or alcohols in case of strong or weak M-O bond, respectively.

5.2 Mechanism for CO_2 reduction and hydrogen evolution

From very early reports by Hori *et al.*, CO has been considered as the first key intermediate toward formation of C_1-C_2 hydrocarbons such as methane and ethylene (Section 2.1).[33,319] Thus, electrochemical CO_2 reduction to CO is expected to occur either *via* (1) a proton-coupled electron transfer (PCET) to form a *COOH species or (2) an electron-transfer (ET) toward a metastable $*CO_2^-$ adsorbate, followed by a quick proton transfer (PT) toward *COOH, see Figure 15a)[9,143] The preferential pathway depends on the given catalytic system.[143,320] Weak to mild *CO binding elements as Cu, Ag, Au have been demonstrated to

favor the $*CO_2^-$ route,[45] while strong binding elements as Pt and Pd and single atom catalysts may prefer the *COOH pathway.[320] As evidence of the $*CO_2^-$ route, experimentally eCO_2R activity was reported to be pH-independent (vs SHE) on mercury and gold.[321–323] High CO_2 reduction activity was observed on Hg in media with low proton availability (dimethylformamide)[321] , while CO partial current density was reported to be independent from bicarbonate and proton concentration and first order on CO_2 pressure on Au.[323]

Generalizing these evidences to other catalysts, the formation of adsorbed $*CO_2^-$ intermediate has been hypothesized as the rate-determining step for electrochemical CO_2 reduction on transition metals,[16] while *COOH formation has been proposed to limit eCO_2R activity on single atom catalysts.[320] Interestingly, recent works shows that alkali metal cations play a significant role along the eCO_2RR pathway.[44,45,170,171] Specifically, Koper and co-workers observed that no CO_2 reduction products were catalyzed on Cu, Ag, and Au without an alkali cation in solution,[45] thus suggesting that explicit cation-CO_2 interactions are needed to stabilize adsorbed CO_2^- on these metals. If instead *COOH formation *via* PCET from CO_2 were to be the first step in eCO_2R, as generally assumed in studies employing the CHE framework,[8,9] then cation stabilization should be less relevant and CO_2 reduction should take place at large overpotentials even without cation.[171]

In addition to $*CO_2^-$ and *COOH formation, recently Chan and co-workers proposed $*CO_2$ adsorption prior to ET as the RDS for eCO_2R on transition metals,[166,320] since a previous study suggested quick electron transfer kinetics for CO_2 activation on Au. In this work,[324] Nørskov, Chan, and coworkers described a reaction scheme involving an initial physisorption of the CO_2 intermediate and a successive electron transfer only at the transition state for CO_2 activation, confirmed by Bader charge for activated CO_2 of -0.35 $|e^-|$. The authors then indicated average electric field/CO_2 dipole interaction as crucial to facilitate CO_2 adsorption.[44] Since no proton transfer is involved in this step, this reaction mechanism fulfills the experimental observation of no pH dependence of CO_2R rate vs SHE. As a short remark on this study, we observe that CO_2 dipole depends on CO_2 activation angles, thus

such dipole stabilization effect may become relevant only after CO_2 activation (bending) due to electron transfer. New studies should carefully assess this aspect, to verify whether average field/dipole interactions are sufficient to stabilize $*CO_2$ before its activation[171,324] or alternative promoters, as cations, are keys.[44,45]

Following the reaction route toward C_1 (from center to left in Figure 15a), the *COOH formed from CO_2 *via* PCET or ET + PT then undergoes a successive proton-coupled electron transfer to form adsorbed *CO. Elements with weak *CO binding, as Au, Ag, and Zn, can release this adsorbate in solution, thus leading to high selectivity toward CO. Instead, for mild to strong *CO binding catalysts, the CO adsorbate can evolve toward other C_1 reduction products, such as methanol and methane, *via* successive proton-coupled electron transfers (Figure 15a)[143] The pH dependence (in SHE scale) of methane formation was first observed by Hori *et al.* for CO reduction on polycrystalline copper,[37] and then confirmed for both CO and CO_2 reduction on Cu(100) and Cu(111) by Schouten *et al.*[141] While methane selectivity is remarkable on copper for cathodic bias more negative than -1.0 V vs RHE, methanol formation on pure Cu is limited to Faradaic efficiencies lower than 1%.[7,106] Both products form either from a *CHO or *COH precursor via 5 and 3 proton-coupled electron transfers respectively (Figure 15a).[143] Since the pioneering work of Peterson *et al.*,[9,325] density functional theory simulations have reported the former intermediate (*CHO) to be thermodynamically more stable, however recent kinetic analysis have indicated that methane formation occurs through the COH* pathway.[326] Generally, Cu(111) has been regarded as selective toward methane[141] due to an effective stabilization of key intermediates on fcc sites.[39,257] In fact, *COH/*CHO and further reduced species accommodate nicely on hollow sites,[39] which can effectively donate electronic density to the adsorbate.[257]

Formate (or formic acid depending on bulk pH) is the last major C_1 product observed during eCO_2R[106] This chemical is expected to originate either from (1) coupling of a hydride with CO_2 *via* sequential PCET and ET,[16,143,302] or a (2) $*CO_2^-$ intermediate adsorbed in a $\eta^2_{O,O}$ configuration *via* ET (see central mechanism in Figure 15a).[141] Alternavely, the second

mechanism may proceed as well directly through a PCET to *OCHO.[327]Strong *H/*CO binding metals as Pt and Pd favors the first route, while weak binding elements as Sn and In exhibit endergonic *H binding, thus favoring the $*OCO^-$/*OCHO route.[11] Then, the hydride-mediated pathway continues with an Heyrovský-step, where the $*H^-$ adsorbate couple with a CO_2 in solution leading to $HCOO^-$ (Figure 15a). On the other hand, the $*OCO^-$ gets protonated to formate (Figure 15a).[327] Evolution of HCOOH depends on bulk pH and may occur as well as a chemical step in solution due to acid/base reactions.[302]

eCO_2R to multicarbon products to date is limited to copper-based catalysts and is assumed to occur from CO-CO dimerization *via* ET (Figure 15b),[16] since the rate-determining step to form these products is pH-independent (Section 2.1).[37,141] The peculiar ability of copper to catalyze this reaction has been attributed to its mild CO binding, which prevents CO poisoning yet allowing the coupling reaction under fairly negative reduction potentials.[11] CO-CO dimerization takes place at high CO coverages and from activated CO adsorbed on atop sites, as demonstrated by suppression of CO rotation band[153] and dynamic C=O stretching band lower than 2060 cm^{-1}.[152] The sluggish kinetics of C-C coupling ($E_a > 1$ eV)[153] should in principle involve poor C_2 formation rates, while in contrast high rates are reported experimentally.[12] Under experimental conditions, cations may stabilize the $*OCCO^-$ dimer[328] and possibly facilitate the electron transfer, thus motivating this discrepancy between experiments and simulations.[45] In fact, short-lived adsorbates with vibrational frequencies attributable through DFT analysis to hydrogenated dimer (*OCCOH) or cation-coordinated dimer were spectroscopically observed under CO reduction on Cu(100), see Section 5.1.[147] In addition to the CO-CO dimerization mechanism, other C-C coupling precursors have been proposed, such as *CO-CH,[155]*CO-$*CH_2$[37], *CO-*CHO[144,329], *CO-*CHO[65,329], and *C-CO.[326] However none of these species have been observed experimentally for eCO_2R on copper.[5,16,330] These alternative C-C steps may be relevant instead for different catalysts and CO coverage regimes.[155,331] Recently, Buonsanti, Calle-Vallejo and co-workers proposed a *CO-*CH coupling step on mixed Cu-Ag nanoparticles to motivate their enhanced selec-

tivity to ethanol.[155] In line with this reaction route, Chang *et al.* employed CO adsorption isotherms and electrokinetic data to demonstrate that under low CO coverage typical of COR, CO-CO is unlikely to be the rate-determining step toward C_{2+} formation.[331]

Following the pathways toward multicarbon species, the transient $OCCO^-$ gets quickly proponated to *COCOH, which then undergoes successive proton-coupled electron transfers toward ethylene, ethanol, and *n*-propanol, the main C_{2+} products (Figure 15b).[106,143] Spectroscopic techniques have not managed yet to detect the short-lived intermediates linking *COCOH to reduction products.[16,146,149] Thus, even though many potential species have been proposed theoretically[5,143,144,329]we avoid here any detailed discussion on them and refer the reader to other works.[5,332] Instead, we address here reaction species and pathways which were verified experimentally through spectroscopic or specific reduction experiments. *$OCHCH_2$, formed from *OCCOH *via* 5 proton-coupled electron transfers (Figure 15b), is generally assumed as the selectivity-determining intermediate between ethanol and ethylene.[16] Schouten, Koper *et al.* reported fully selective reduction of glyoxal (OCHOCH) and glycolaldehyde ($HOCH_2CHO$) to acetaldehyde and ethanol on polycrystalline copper on phosphate buffer by Online Electrochemical Mass Spectrometry (OLEMS).[140] Since both glyoxal and glycolaldehyde can undergo 3 and 1 PCETs to *$OCHCH_2$ (Figure 15b),[144] this intermediate is a precursor of ethanol. To further assess the relevance of this precursor, Calle-Vallejo and Koper calculated the thermodynamic cost for further protonation of *$OCHCH_2$ either to (1) *$OCHCH_3$ or (2) *O + C_2H_4.[300] Both steps are exergonic, with the ethylene selective route, (2), more favorable than the ethanol/acetaldehyde one, (1), by 0.2 eV.[300] Since ethylene is the major C_2 product and it is typically formed at higher rates than ethanol,[35,36,106] the authors concluded that *$OCHCH_2$ should be the key reaction intermediate to rule selectivity toward ethylene and ethanol, so-called selectivity-determining step (SDS).

Alternatively, other theoretical studies employed thermodynamic considerations to suggest earlier bifurcation in the ethylene/ethanol route, with among others *CHCOH,[329] *CO-

CHOH,[144,329] and other ketenes as potential ethylene precursors (Figure 15b). These precursors may then lead to formation of ethylene oxide adsorbed *(O)CH_2CH_2,[329] which proved to be fully selective to ethylene on copper in a phosphate buffer.[140] While several sound theoretical evidences confirm a *$OCHCH_2$ → *$OCHCH_3$ → ethanol route on copper and OD-Cu,[140,142,333] a *$OCHCH_2$ mediated ethylene pathway seems at odds with the full selectivity of glyoxal and glycolaldehyde to ethanol.[140] Besides, an early bifurcation between the ethylene and ethanol pathways would reconcile experimental and theoretical observations on the role of atomic oxygen to trigger C_2H_5OH formation.[14,109,125,127,210] Recently, we have proposed a subsurface oxygen-mediated deprotonated glyoxylate (Figure 15b) as the precursor leading to ethanol formation on oxide-derived copper,[210,314] where this alcohol is reported as main reaction product (F.E. > 40% at −0.3 V vs RHE) without any trace of ethylene.[109] Otherwise, this intermediate could undergo one 1 PT and 5 successive PCETs to acetate (Figure 15b), observed concurrently with ethanol at low overpotential on OD-Cu (20% F.E. at −0.25 V vs RHE)[109] Besides, competition between ethanol and ethylene during pulsed CO_2 electroreduction was reported to depend on the cell temperature, with lower temperature (5 °C) favoring the alcohol while higher temperature (25 °C) promoting hydrocarbon formation.[127] This interesting result was attributed to Cu(I) (or equivalently residual oxygen) reducibility.

As a further proof of the role of atomic oxygens from OD-Cu or solvation, more than 60% of oxygen contained in ethanol formed on crystalline copper facets arises from water molecules, as demonstrated for $C^{16}O$ reduction in $H_2^{18}O$ solvent.[125] This evidece was confirmed also for acetate and 1-propanol, thus to rationalize this process the authors suggested a OH^- insertion mechanism on a *CCH backbone, which then reduce to the three products. Instead, successive theoretical and experimental studies attributed the observation to oxygen exchange between acetaldehyde reduced from CO and water, thus disregarding any role of solvation molecules in earlier reaction stages.[123,124,335] In addition, analogous insertion mechanisms of solvent or subsurface atomic oxygen were predicted. Heenen *et al.*

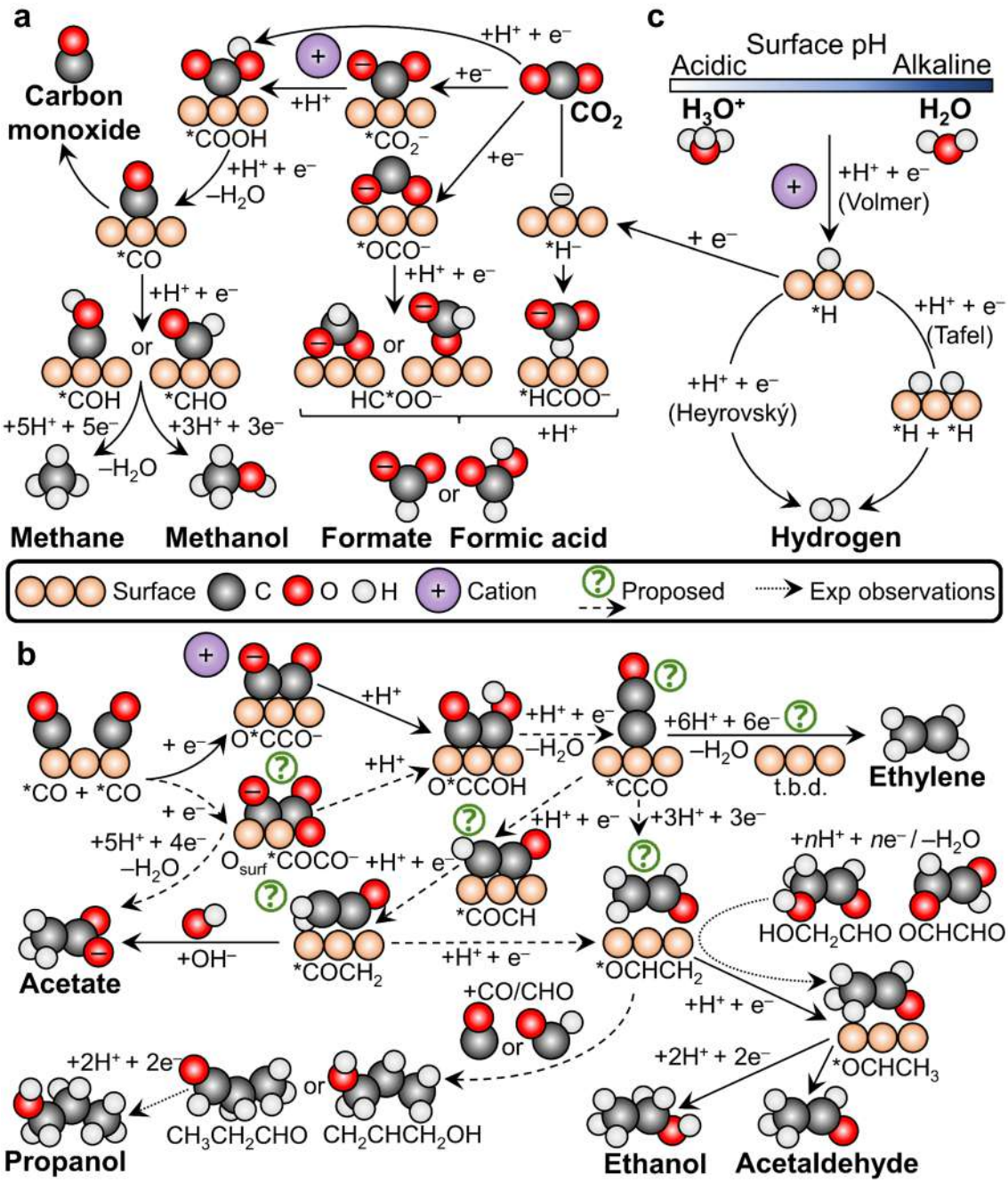

Figure 15: eCO_2R pathway toward major **a**, C_1 and **b**, C_{2+} products on metals. Experimental observations are taken from Refs. 140 and 334. The CO-CO dimer bound to a near-surface oxygen is the deprotonated glyoxylate geometry predicted on OD-Cu.[210,314] n is equal to 3 and 1 for reduction of glyoxal (OCHOCH) and glycolaldehyde ($HOCH_2CHO$) to $*OCHCH_2$. **c**, Hydrogen evolution reaction mechanism on metals, as defined in Ref. 41. The key role of cations in enabling CO_2 adsorption, C-C coupling, and Volmer step for water dissociation has been proposed in Refs. 44,45, 328, 42,160,161. Full arrows represent confirmed routes.

employed an *ab initio* kinetic-transport model to describe the mechanism for acetate formation on copper, proposing H_2CCO coupling to OH^- in solution as the main precursor toward $CH_3CO_2^-$ with ketene as common C_{2+} intermediate (Figure 15b, further details on the mechanism in Section 6).[336] Such analogy between acetate and ethanol reaction route is further supported by $^{13}CO_2$-^{12}CO electroreduction experiments on OD-Cu copper. Different $^{13}C/^{12}C$ ratios were detected in the reaction products, namely ethylene, ethanol, acetate, and *n*-propanol.[122] Ethylene and propanol showed an high ^{13}C fraction (0.3-0.5 isotopic composition), thus suggesting a more favorable reduction from $^{13}CO_2$ precursors, while acetate and ethanol present an equivalent low ^{13}C fraction (0.25-0.4), thus preferential formation from paired $^{13}CO_2$-^{12}CO or ^{12}CO. This led to the conclusion that the active sites on OD-Cu involved in acetate/ethanol formation might be different from the ones enabling ethylene and propanol formations

Experimental and theoretical insights into C_{3+} products are limited by the complexity of the reaction mechanism and the low selectivity of these chemicals, which prevents spectroscopic observation of the potential intermediates and comprehensive screening of electrochemical reduction experiments for key reagents. Even though sequential CO trimerization has been proposed in the past,[337] currently the expected coupling mechanism toward C_3 products involves a $OC(H)CH_2$-$C(H)O$ precursor,[156,334] potentially involving allyl alcohol (CH_2CHCH_2OH) and propionaldehyde (CH_3CH_2CHO) at later reduction stage (Figure 15b).[334] In fact, F.E. toward propanol, allyl alcohol, and propionaldehyde for eCO_2R exhibits similar dependencies on applied potential for a polycrystalline copper catalysts[106] and were equally promoted on Ag-decorated Cu_2O nanocubes[154] As for C_4 products, to date two main reaction pathways have been proposed for the formation of 1-butanol, the only species observed at significant rate.[94,338] Both reaction schemes highlight the key role of an acetaldehyde precursor. Ting *et al.* have indicated that CO_2 first reduces to acetaldehyde on OD-Cu under alkaline bulk pH.[94] Acetaldehyde then undergoes a base-catalyzed aldol condensation to crotonaldehyde, which is then reduced to butanal, 1-hydroxybutyl,

and finally 1-butanol. On the other hand, Choi *et al.* have highlighted a different reduction mechanism on phosphorus-rich copper, involving formation of acetaldehyde from aldehyde self-condensation of two formate precursors. Finally, acetaldehyde undergoes aldol condensation and sequential hydrogenation to 1-butanol.[338]

Moving to the reaction competing with eCO_2R, hydrogen evolution (Figure 15c), we refer the reader to the nice perspective by Dubouis and Grimaud for a detailed discussion.[41] In short, HER first involves reduction of a proton *via* a proton-coupled electron transfer, the so called Volmer step, Scheme 18. Then, this *H species can evolve molecular H_2 either through a second proton-coupled electron transfer from solution, Heyrovský step, or the coupling of two adsorbed protons, Tafel step, Scheme 18. H_3O^+ and H_2O in solution are typically assumed as proton sources at acidic and alkaline surface pH (Figure 15c)[41] Nevertheless, under electrochemical CO_2 reduction, HER is generally assumed to occur through water reduction (H_2OR), thus releasing OH^- upon reaction,[16] since proton reduction is diffusion limited even at acidic bulk pH.[339,340] Proton reduction does not typically exhibit cation effect, while water reduction strongly depends on cation concentration and species.[42,160,161] Such dependence is discussed in details in Section 7.1.

$$\begin{aligned} \text{(Volmer)} \quad & H_3O^+/H_2O + e^- + * \rightarrow H* + H_2O/OH^- \\ \text{(Heyrovský)} \quad & H_3O^+/H_2O) + e^- + H* \rightarrow H_2 + H_2O/OH^- \\ \text{(Tafel)} \quad & 2H* \rightarrow H_2 \end{aligned} \tag{18}$$

5.3 Mechanism for oxygen evolution

In acidic environments, the OER mechanism can be described as below, Scheme 19.[77] In the scheme, * is adsorption site, *OH, *O, and *OOH are adsorbed OH group, O atom, and OOH group respectively. ΔG_i is variation of Gibbs free energy related for each step i.

$$
\begin{aligned}
&\mathrm{H_2O} + * \rightarrow *\mathrm{OH} + \mathrm{H^+} + \mathrm{e^-}; \Delta G_1 = \Delta G_{*\mathrm{OH}} - \Delta G_{\mathrm{H_2O}} - |\mathrm{e^-}|U \\
&*\mathrm{OH} \rightarrow *\mathrm{O} + \mathrm{H^+} + \mathrm{e^-}; \Delta G_2 = \Delta G_{*\mathrm{O}} - \Delta G_{*\mathrm{OH}} - |\mathrm{e^-}|U \\
&*\mathrm{O} + \mathrm{H_2O} \rightarrow *\mathrm{OOH} + \mathrm{H^+} + \mathrm{e^-}; \Delta G_3 = \Delta G_{*\mathrm{OOH}} - \Delta G_{*\mathrm{O}} - |\mathrm{e^-}|U \\
&*\mathrm{OOH} \rightarrow * + \mathrm{O_2} + \mathrm{H^+} + \mathrm{e^-}; \Delta G_4 = \Delta G_{\mathrm{O_2}} - \Delta G_{*\mathrm{OOH}} - |\mathrm{e^-}|U
\end{aligned} \tag{19}
$$

The total energy increase in these four steps is 4.92 eV, which is the energy cost for water splitting. The overpotential is defined by: $\eta^{\mathrm{OER}} = \max[\Delta G_i]/|\mathrm{e}|^- - 1.23$ V. The ideal catalyst should evenly divide the total energy cost, thus resulting in zero overpotential. Based on this mechanism, the adsorption energies ($E_{\mathrm{ads}}(X) = E(X*) - E(*) - E(X)$, X = OH, O, and OOH) of OH, O, and OOH determines the OER energy profile. To some extent, E_{ads}(OOH) correlate with E_{ads}(OH) through tLSR, as discussed in detail in Section (2.2.4) On one hand, a strong O binding, *i.e.* large $\Delta G(\mathrm{O_{ads}})$, leads to large ΔG_3 (Scheme 19), hence a large overpotential is expected. On the other hand, a weak O adsorption results in large ΔG_2 and ΔG_4 (Scheme 19), leading equally to large overpotential. An optimal catalyst is predicted to have $\Delta G(\mathrm{O_{ads}}) = 2.46$ eV.

In alkali environments,[77] OER process follows the Scheme 20. for which the considerations reported for alkaline pH applies as well.

$$
\begin{aligned}
&\mathrm{OH^-} + * \rightarrow *\mathrm{OH} + \mathrm{e^-} \\
&*\mathrm{OH} + \mathrm{OH^-} \rightarrow *\mathrm{O} + \mathrm{H_2O} + \mathrm{e^-} \\
&*\mathrm{O} + \mathrm{OH^-} \rightarrow *\mathrm{OOH} + \mathrm{e^-} \\
&*\mathrm{OOH} + \mathrm{OH^-} \rightarrow * + \mathrm{O_2} + \mathrm{H_2O} + \mathrm{e^-}
\end{aligned} \tag{20}
$$

6 Microkinetic modeling

Mechanistic studies for the large reaction network involved in eCO_2R couple well with multi-scale methods like microkinetic modeling (MKM), as this technique can help delineate which reaction pathways have the dominant rates for selective production of the target hydrocarbon or alcohol products. Even though microkinetic modeling is vastly used in heterogeneous catalysis, its application to electrocatalysis is limited by the complexity embedded in estimation of electrochemical activation barriers and potential contributions from electric field and solvent.[341–343] Nevertheless, in the past few years the use of microkinetic modeling has picked up pace and several studies have used MKM to simulate polarization curves for selective CO conversion from CO_2.[44,320,344–346] A few recent studies have also used MKM to understand the complex reaction network for the formation of C_1 and C_2 hydrocarbon and alcohol products (see for instance Ref. 347), thus the review mainly focuses on these works which go beyond assessment of CO formation.

As discussed in Section 2.1, Hori's work on Cu surfaces showed that the pH dependence is different for C_1 and C_2 product formations,[37] indicating that the RDS for methane and methanol involves a proton-coupled electron transfer while the RDS for C_2 products involves an electron transfer.[16,141,143] Further, the obtained Tafel slopes are usually smaller for C_1 products as compared to the C_2 products (see Figure 16a), even though Tafel slope analysis may be not always statistically relevant due to physical non idealities, *e.g.* charge transfer, electrostatic screening of adsorbates, etc.[348] To explain the differences in Tafel slope and pH dependence for the formation of C_1 vs C_2 products from CO, Chen and co-workers performed microkinetic modeling for CORR on Cu(211).[349] The insights on the rate determining steps were used to obtain analytical expressions for polarization curves, which aided the interpretation of the MKM results. Using free energy diagrams, the authors predicted that the first proton-electron transfer of OCCO* intermediate is rate-determining for the formation of C_2 products at low potentials (-0.5 V vs RHE), while the third PCET along CO reduction, *CHOH formation, is rate determining for C_1 products (Figure 16b). This led to a difference

in Tafel slopes for the two classes of products (C_1 vs C_2) based on Equation 21 , where n here corresponds to the number of PCETs which occur before the RDS, U is the potential vs SHE, and k is the reaction rate based on Butler-Volmer kinetics. At high negative potentials (-1 V vs RHE), the RDS step changes from PCET to *OCCOH to CO dimerization toward C_2 products, while the first proton-electron step is defined as the RDS for C_1 product formation. This led to an increase in Tafel slope for C_1 products, while for C_2 products the current density decreases, as the rate has second order dependence on CO coverage, which depletes as the products are formed.

$$\frac{\partial U}{\partial log(k)} = -\frac{2.3 \mathrm{k_B} T}{(n+\beta)e} \tag{21}$$

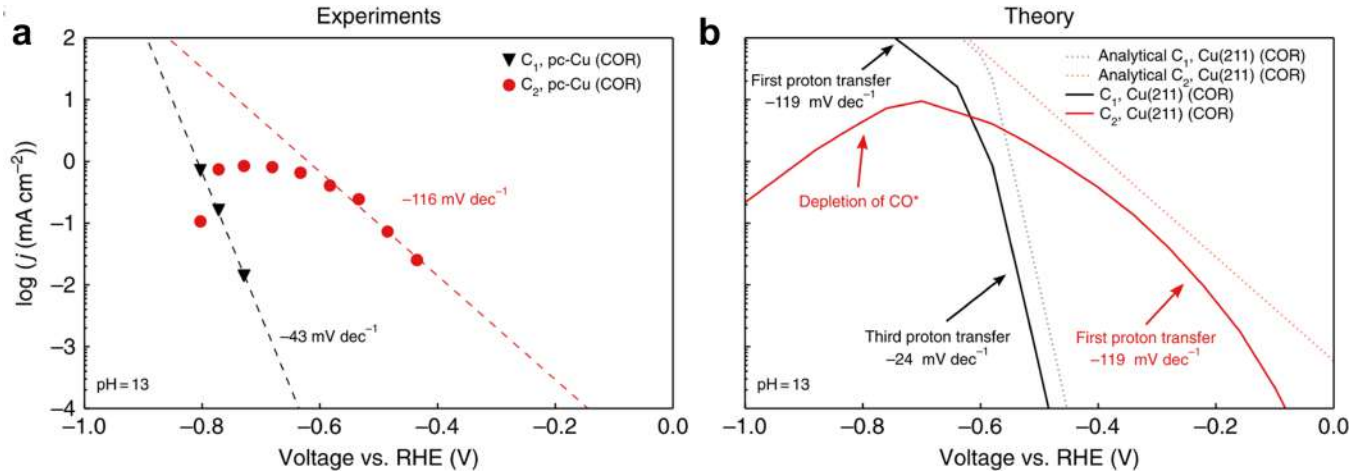

Figure 16: **a**, Experimental polarization curves on polycrystalline Cu for CO reduction toward C_1 and C_2 products at pH = 13. Data are taken from Ref. 350. **b**, Polarization curves predicted by the full microkinetic model and the associated analytical approximation on Cu(211) for CO reduction toward C_1 and C_2 products at pH = 13. Adapted with permission from Ref. 349 (Copyright 2020 Springer Nature under Creative Commons Attribution 4.0 International License[157]).

In terms of pH dependence, experiments showed that there is a drastic decrease in onset potential for formation of C_2 products as we move towards alkaline conditions, while no relevant impact is observed for C_1 products.[350] This was again rationalized by MKM-based analytical expressions derived for current densities, which showed that the earlier the RDS

along the pathway, the larger the decrease in onset potential with pH. Since the RDS for C_2 products involves a PCET which occurs at an earlier stage than the C_1 products, this motivates the stronger impact of pH on overpotentials for C_2 products. Finally, the authors suggested as well depletion of C_2 products at high potentials for alkaline conditions using the microkinetic model.

Peng, Tang, and coworkers also performed microkinetic modeling on Cu(100) for CORR to understand the dominant pathways that lead to the formation of methane and ethylene, used in the study as proxy for C_1 and C_2 product formations.[326] The major focus of the paper was to build mechanisms for C_1 and C_2 formations using surface carbon (C*) as a plausible intermediate. Through their MKM results, they found that for wide potential and pH windows methane is formed through the COH* pathway, which followed through a *C intermediate. As for the ethylene pathway, at neutral pHs and potential windows of interest for C_{2+} products (from -0.4 to -1 V vs RHE), the OC-C* route is the dominant pathway, which shifts to the traditional OCCOH pathway at alkaline pHs.

Furthermore, the MKM analysis at neutral pHs illustrated that the protonation of C* and the C*-CO coupling are the bifurcation points which ultimately determine the competition between C_1 and C_2 products. Using these insights, a simplified rate expression was derived for ratio of rates for C_1 vs C_2 formations in terms of the barriers for C* protonation and C*-CO coupling. This analytical expression was then used to delineate the trends across different Cu facets. The trend in predicted C_2/C_1 products selectivities was calculated as follows: Cu(511)>Cu(100)>Cu(211)>Cu(111), observation which is in good agreement with experiments by Hori *et al.* on single crystal surfaces (Section 2.1).[35,36]

While microkinetic modeling only considers processes which occur at the surface, transport equations need to be integrated to estimate the concentration of species near the electrode. For pathways involving reaction intermediates in solution, these mass transfer effects can ultimately determine which reaction pathways have the highest rates. In the following lines, we focus on two studies where mass transfer has been proved to play a pivotal role

towards defining which reaction mechanism is favored among various plausible alternatives.

Singh *et al.* used multi-scale modeling approaches to look at CO formation from CO_2 on Ag(110) surface by including mass transfer effects.[351] They considered three reaction mechanisms (RM) for the formation of COOH* and CO* in which the proton donor is either H*, H_2O*, or H_2O in solution (denoted as RM-1, RM-2 and RM-3). Remarkably, RM-3 was the only pathway which involved $*CO_2^-$ as a plausible surface intermediate in the reaction mechanism. The DFT energetics were inputted into the microkinetic model and the appropriate rate equations for the surface reactions were solved. Next, the current densities from the microkinetic model and the diffusion coefficients of species in the electrolyte were inputted into the continuum transport model and the equations were solved iteratively till the bulk pH and CO_2 concentration converged. Through this systematic approach, the authors found that even though the RM-3 pathway had the highest activation energies for the CO formation, only this reaction scheme could reproduce the experimental correlation observed between current densities and CO_2 partial pressure.[352] Further, the most abundant adsorbed species were found to be *COOH and $*CO_2^-$ which is in agreement with the spectroscopic observations on silver catalysts. Finally, the authors concluded that explicit assessment of mass transfer effects enable better reproduction of the experimental trends of CO and H_2 partial current densities vs applied potential.

More recently, Chan and co-workers used a coupled microkinetic and transport model to study the mechanism for acetate formation on Cu surfaces.[336] The authors proposed a reaction scheme where the surface intermediate ketene (CH_2CO*) desorbs and reacts with OH^- in solution. Overall, two possible selectivity-determining steps (SDS) for acetate formation were envisioned (Figure 17): (1) reaction of H_2COO (aq) with OH^- vs readsorption of this species (SDS-1) (2) desorption of H_2CO* into solution vs further proton electron steps to form other C_2 products (SDS-2). It is important to note that the SDS-1 only involves chemical steps, while the SDS-2 involves both a chemical and a PCET step. Energetics and initial concentrations of the reactants were then inputted in the integrated multi-scale model,

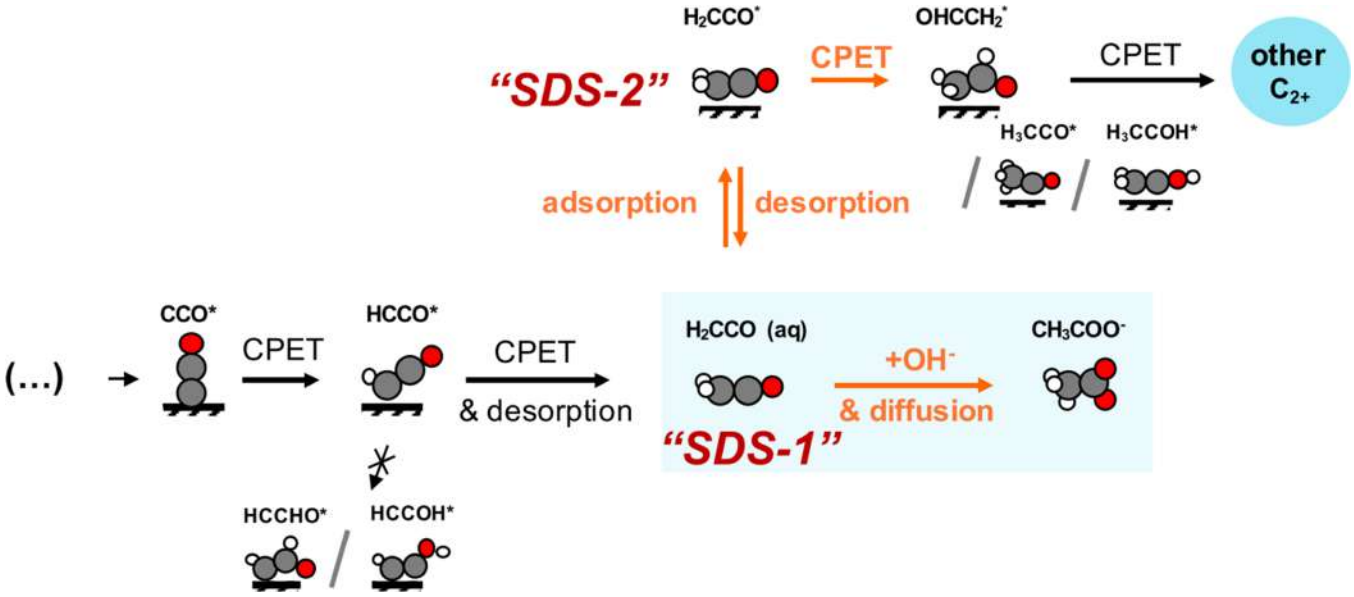

Figure 17: Schematic of the ketene pathway, including the two selectivity-determining steps towards acetate, either *via* a reaction in solution (SDS-1), or further reduction of the adsorbed ketene (H_2CCO^*) to form other C_2 products (SDS-2). The excluded alternative reduction steps are reported in the bottom left. Adapted with permission from Ref. 336 granted by the authors under Creative Commons Attribution-NonCommercial-NoDerivatives 4.0 International License.[353]

which showed that acetate selectivity followed a U-shaped dependence on applied potential vs SHE, in agreement with experimental data. At low overpotentials, the PCET step towards the formation of H_2COO^* from the ketene intermediate is limiting. As the potential shifts to more negative values, this PCET step becomes more favorable, consequently leading to decrease of acetate selectivity (SDS-2). Finally, at very high overpotential, H_2COO^* formation is now facile and acetate selectivity is now ruled by the competition between H_2COO^* reduction or desorption and further reaction with OH^- in solution (SDS-2). Thus, the formation of acetate is now dependent on local OH^- concentration (SDS-1), which increases at more negative potentials due to water and CO_2 reduction, leading again to a U-shaped dependence on applied potential. Moreover, the effects of pH and surface roughness are also confirmed by specific experiments. Intriguingly, this solution phase mechanism are at odds with other proposed mechanisms for acetate formation[125] (Section 5.2), consequently the authors proved the power of an integrated transport/kinetic framework for finding the

dominant reaction pathways which drive the formation of a specific product.

7 Modeling electrolyte and bulk mass transfer effects

In addition to Faradaic processes at the surface, phenomena occurring within the diffusion layer are crucial in electrocatalysis.[2] As shown in Section 3.3, a proper understanding of local electrolyte effects can be employed to enhance the performance of eCO_2R and HER.[15,42,161,354] Explicit cation effect are well-known to promote the overall activity and selectivity of these reactions,[32,161] whilst surface poisoning from electrolyte anions have the opposite effect.[174–176] Besides, mass transfer within the diffusion layer is also instrumental for the industrial exploitation of eCO_2, motivating the need for optimized configurations such as gas diffusion electrodes.[355,356] Lastly, chemical reactions within the diffusion layer must be properly accounted, since they can limit the overall performance of electrocatalytic devices[357] or tune product distributions through chemical instead of electrochemical steps.[94,358] For instance, the conversion of CO_2 and OH^- to CO_3^{2-} is the main source of energy loss in CO_2 reduction under neutral to basic bulk pH.[357] Consequently, industrially relevant single-pass CO_2 utilization and conversion/energy efficiency can be achieved only at acidic pH, as demonstrated independently by Huang *et al.*[179] and Monteiro *et al.*[359] As further examples of chemical steps within the diffusion layer, formation of carboxylic acids and alcohols during CO_2 reduction conditions was demonstrated to occur through disproportionation of aldehydes due to high alkaline surface pH instead of direct eCO_2R.[358] Besides, eCO_2R to 1-butanol (F.E. = 0.056%, $j = -0.080$ mA cm^{-2} at -0.48 V vs RHE) on a oxide-derived copper catalyst was proposed to happen through a final chemical step, *i.e.* hydrogenation of 1-hydroxybutyl formed from acetaldehyde reduction (for further details on the mechanism, see Section 5.2).

7.1 Cation effects

Electrolyte effects are known in eCO_2R since the initial observations by Hori *et al.* illustrating higher activity for larger ionic radius alkali cations (Section 2.1).[33,170,171,360] Following Frumkin's theory,[361] the authors attributed this enhancement to modification of the local electrostatic field within the electrical double layer through specific cation adsorption. In particular, weakly hydrated cations can better accumulate at the Outer Helmholtz plane (OHP), thus leading to a more intense electrostatic field.[33] However, the occurrence of specifically adsorbed cations under CO_2 reduction conditions is a topic of vivid debate in the field.[362]

Mills *et al.* employed density functional theory to estimate the equilibrium potential U_0 for cation adsorption on fcc(111) facets of Ag, Au, Ni, Pd, Pt, Equations 22 and 23.[363] $G_{*\mathrm{cat}}$, G_*, and G_{cat^+} are the Gibbs free energies for the metal/water/cation system, metal/water, and solvated cation alone, respectively. G_{cat^+} was estimated from the free energy of cation in gas phase, corrected by experimental solvation energy at 1 M solution. The term which depends on potential at PZC (U_{pzc}) and cation (system) electric dipole moment, $|\vec{p}_{*\mathrm{cat}}|$ ($|\vec{p}_*|$), is included to account for the partial positive charge retained by the cation upon solvation, which generates a dipole moment along the surface normal direction. Finally, d represents the thickness of the electrical double layer.

$$* + \mathrm{cat}^+_{\mathrm{aq}} + \mathrm{e}^- \rightarrow *\mathrm{cat} \tag{22}$$

$$U_0 = \frac{-G_{*\mathrm{cat}} + G_* + G_{\mathrm{cat}^+} + U_{\mathrm{pzc}} \frac{|\vec{p}_{*\mathrm{cat}}| - |\vec{p}_*|}{d}}{|\mathrm{e}^-| + \frac{|\vec{p}_{*\mathrm{cat}}| - |\vec{p}_*|}{d}} \tag{23}$$

By referring Equation 23 to the Normal Hydrogen Electrode reference and carrying out benchmarks with different numbers of water molecules within the solvation layer, the authors estimated equilibrium adsorption potentials for cations more negative than -0.80 V vs NHE (Cs^+ adsorption on Pt) and far from CO_2 reduction conditions for Ag and Au ($U_0 < -2.0$ V vs NHE) (Table 1).[363] Although these equilibrium adsorption potentials are significantly more negative than cathodic bias for eCO_2R, we note that the role of near-surface solvent or

other electrolyte effects may further stabilize cation specific adsorption on metals. Thus, this process should not be disregarded. In a successive study from the same authors, iodine and potassium co-adsorption was suggested to occur on copper under CO_2 reduction conditions at low cation coverage (θ = 0.11 ML) and alkaline pH, leading to a preferential increase of binding energy of O-terminated species.[225] In line with such prediction, recently a Total Reflection Surface Enhanced Infrared Absorption Spectroscopy (ATR-SEIRAS) study of CO adsorption configurations on Pt and Au revealed that at low cathodic bias the band for linearly-bond CO disappears, likely due to displacement by K^+ at the OHP.[364]

Table 1: Estimated equilibrium potential U_0 (V vs NHE) for cation adsorption on fcc(111) electrode surfaces. Data taken from Ref. 363

system	H^+	Li^+	Na^+	K^+	Cs^+	Ba^{2+}
Pt(111)	−0.07	−1.30	−0.90	−0.98	−0.80	−1.31
Pd(111)	+0.09	−1.63	−1.19	−1.35	−1.09	−1.43
Ni(111)	+0.05	−2.06	−1.61	−1.85	−1.68	−1.86
Au(111)	−1.29	−2.76	−2.40	−2.74	−2.64	−2.46
Ag(111)	−0.65	−2.63	−2.11	−2.52	−2.44	−2.62

Following our overview on cation effects, an increasing number of experimental reports attributed the trends on eCO_2R activity and selectivity to non electric fields effects, such as cation coordination with intermediates at the surface,[365] or increased polarizability of adsorbates.[366] To unveil this phenomenon, Singh *et al.* employed a 1D mathematical model for an electrochemical cell for eCO_2R with anolyte, catholyte, Pt anode, Cu (and Ag) cathode, a anion-exchange membrane to separate anolyte and catholyte, and different species within the electrolyte: CO_2, HCO_3^-, CO_3^{2-}, H^+, OH^- and alkali metal cations (Li^+, Na^+, K^+, Rb^+, Cs^+).[172,367] This model was solved using the COMSOL multiphysics software and including ion migration, diffusion, acid-base equilibrium, gas-liquid transport of CO_2, hydrolysis of cations, and kinetics for both OER and CO_2.[172] Since the pK_a for an hydrated cation represents the ease to undergo hydrolysis, the authors estimates this parameter in the bulk electrolyte and in the proximity of the Cu and Ag cathodes at −1.0 V vs RHE, respectively. Whilst cation pK_a at the bulk increases following the ionic radius, since larger

ionic radius cations exhibit lower electrostatic interaction with neighboring water molecules, this trend overturns near the cathode surface due to the higher electrostatic field generated by weakly hydrated cations (larger ionic radius), Table 2. The authors derived an analytical equation to estimate the pK_a for cation hydrolysis at the cathode, which is proportional to both cation/water and cation/cathode electrostatic interactions. These terms are shown in Equation 24, where z is the effective charge of the hydrated cation, σ the surface charge density, $r_{\text{M-O}}$ the sum of cation (M) and oxygen (O, from water) radii, and $r_{\text{H-El}}$ the distance between hydration shell and cathode surface. Equation 24 was verified experimentally by measuring the pK_a of monovalent alkali metal cations through potentiometric titration, thus A and B were calculated by fitting the analytical equation to the experimental data.

$$\text{p}K_a = -A\left[\frac{z^2}{r_{\text{M-O}}} + 2\pi\sigma z r_{\text{H-El}}\left(\sqrt{1+\frac{r_{\text{M-O}}^2}{r_{\text{H-El}}^2}}-1\right)\right] + B \tag{24}$$

Since pH at the surface is rather alkaline under CO_2 reduction conditions in a neutral bulk electrolyte,[16] then K^+, Rb^+, Cs^+, having low pK_a,[367] can undergo hydrolysis, thus leading to pH buffering and consequent higher concentrations of CO_2 at the surface. In absence of alkali cations, an alkaline pH at the surface involves rapid neutralization of CO_2 by a neighboring OH^- to form carbonate, so that CO_2 surface concentration decreases significantly with consequent mass transfer limitations on eCO_2R activity. Hence, the well-known cation effect on eCO_2R was solely rationalized through hydrolysis of electrolyte cations, suggesting that weakly hydrated cations have a lower pK_a at the surface, thus they allow for an increased pH buffering and higher CO_2 availability. The continuum model employed resulted in remarkable agreement with experimentally measured current densities on Cu and Ag at -1.0 V vs RHE for the different cations assessed. However, a recent study estimated CO_2 concentration at a Au electrode from ATR-SEIRAS measurements and demonstrated a negative correlation of this parameter with cation ionic radius,[368] since weakly hydrated cations promote CO_2 reduction to a larger extent, thus leading to higher CO_2 consumption

and lower local concentration. Instead, the prediction of higher pH buffering for cations with larger ionic radius was confirmed by ATR-SEIRAS characterization, where the authors probed pH at a gold/electrolyte interface from the CO_2/HCO_3^- bands ratio.[369]

Table 2: pK_a for cation hydrolysis in the bulk electrolyte (bulk) and at the surface layer of copper (Cu) and silver (Ag) cathodes at −1.0 V vs RHE,[172] obtained by solving Equation 24. Data taken from Ref. 172

cation	bulk	Cu (Surf)	Ag (surf)
Li^+	13.6	11.64	13.16
Na^+	14.2	10.26	11.44
K^+	14.5	7.95	8.49
Rb^+	14.6	6.97	7.23
Cs^+	14.7	4.31	4.32

Some of the proponents of the hydrolysis hypothesis carried out a follow up study with lower applied potentials, so that mass transfer contributions to eCO_2R activity and selectivity could be neglected. Specifically, Resasco *et al.* demonstrated that Faradaic efficiencies for eCO_2R on Cu(100) vary by increasing the CO_2 flow rate for potentials more negative than −1.1 V vs RHE,[170] thus suggesting the critical role of CO_2 diffusion under the regime of their previous study.[172] Overall, production rates of formate, ethylene, and ethanol showed a positive correlation with the ionic radius of alkali cations for Cu(100) and Cu(111), whilst hydrogen, carbon monoxide, and methane formations were not affected. Similarly, both CO and $HCOO^-$ partial current densities on Ag and Sn increased following the trend of cation ionic radius. Small additions of larger size cations on a 0.1 M $LiHCO_3$ electrolyte with constant ionic strength suddenly changed the partial current density toward ethylene, ethanol, and formate on Cu(100), suggesting that larger cations accumulate more at the surface/electrolyte interface. To rationalize the last evidence, the authors employed a simplified model for a Cu/electrolyte interface: a Cu(111) supercell with two ice-like water bilayers, one solvated cation, 12 Å of vacuum, and explicit electric potential.[44,170] Constrained minima hopping (CMH)[268] was carried out on the system to optimize cation solvation shell. Finally, the thermodynamic driving force for each cation to accumulate at a distance of 6.25

Å from Cu(111) was estimated from the lowest energy configurations of the solvated cations and the cation reduction potentials.[91] In fact, the energy of the cation/electron pair in the bulk electrolyte $G_{\mathrm{cat^+ + e^-,bulk}}$ can be derived by applying the CHE[8] formalism to cation reduction (Equation 25), where cat and solv stand for cation and explicit solvent molecules within its coordination shell. At the equilibrium potential for cation reduction, U_0, both processes are in equilibrium, thus the energies of products and reactants are equivalent. Thus, $E_{\mathrm{cat^+ + e^-,bulk}}$ at a given potential U can be calculated from Equation 26. Since the energy of the cation/electron pair at the OHP, $E_{\mathrm{Cat^+ + e^-,OHP}}$, can be estimated from the CMH simulations, the thermodynamic driving force for cation accumulation is given by Equation 27.

$$\mathrm{cat^+_{solv} + e^- \rightarrow cat + solv} \tag{25}$$

$$E_{\mathrm{cat^+ + e^-,bulk}} = E_{\mathrm{cat}} - |\mathrm{e^-}|(U - U_0) \tag{26}$$

$$\Delta E_{\mathrm{cat,OHP}} = E_{\mathrm{cat^+ + e^-,OHP}} - E_{\mathrm{cat^+ + e^-,bulk}} \tag{27}$$

The dependence of $\Delta E_{\mathrm{cat,OHP}}$ on potential U (vs SHE) is derived from the work function ϕ of the interface referred to the work function of the SHE electrode and it is scaled through the partial electron transfer to the cation upon migration from bulk electrolyte to the OHP.[170] Taking $\Delta E_{\mathrm{cat,OHP}}$ for Li^+ as a reference, accumulation is more exothermic for larger size cations (Figure 18a), thus suggesting that cation trend on eCO_2R is mainly due to larger concentrations at the OHP of K^+ and Cs^+ versus Li^+ and Na^+, respectively. The hypothesis of the preminent role of accumulation to drive eCO_2R activity was further confirmed by an almost equivalent cation-induced electric field near a CO molecule adsorbed on Cu(111), independent from the cation species in the vicinity.[170] Higher accumulation at the surface for cations with larger ionic radius was confirmed independently in a recent theoretical study solving generalized modified Poisson-Nernst-Planck equations for a CO_2 reduction system.[164] The mathematical details behind the model will be discussed in Section 7.3. For a cathodic bias of -0.32 V vs PZC, Li^+, Na^+, K^+, and Cs^+ concentration at the OHP accounted for

$\sim$ 4 M, $\sim$ 4.5 M, $\sim$ 6 M, and $\sim$ 6 M respectively.

As for specific cation effects, an earlier study by Chen *et al.* rationalized the local stabilization of reaction intermediates through the dependence of adsorbate formation energy on its electric dipole moment $\vec{p}$ and polarizability α, as well as on the electric field $\vec{E}$, Equation 28.[44] By calculating CO_2 adsorption energy versus the applied electric field $\vec{E}$, induced either by an external dipole potential under vacuum,[231] or insertion of solvated cations close to the surface (K^+ and 1-ethyl-3-methylimidazolium, $EMIM^+$), the authors proved the correctness of the former hypothesis.[44] The presence of a solvated cation close to the surface leads to very localized electric field in the order of -1.0 V Å^{-1}, which quickly decays beyond a radial distance of 5 Å (Figure 18b). The electric field at a given radial distance $\vec{r}$ from the cation was derived from the variation of electrostatic potential due to charged species, Equation 29, where surf, solv, and cat stand for surface, solvent molecules, and cation respectively. Hence, the cation-induced electric field, $\vec{E}_{\text{cat}}$, is given by Equation 30, where $\vec{r}_{\text{ads}}$ and $\vec{r}_{\text{cat}}$ are the coordinates of adsorbate and alkali cation. The additional negative sign highlights that the electric field is estimated for a negative unit charge.

$$E(\vec{E}) = E(\vec{E} = 0 \text{ VÅ}^{-1}) + \vec{p} \cdot \vec{E} - \frac{\alpha |\vec{E}|^2}{2} \tag{28}$$

$$U(\vec{r}) = U_{\text{surf/solv/cat}} - U_{\text{surf}} - U_{\text{solv}} - U_{\text{cat}} \tag{29}$$

$$-\vec{E}_{\text{cat}} = -\left(-\frac{U(\vec{r}_{\text{ads}}) - U(\vec{r}_{\text{cat}})}{\|\vec{r}_{\text{ads}} - \vec{r}_{\text{cat}}\|}\right)\hat{r} \tag{30}$$

Recently, we applied the formalism mentioned above (Equations 29, 30) to demonstrate that cation-induced electric field strongly depends on cation coordination shell and cation-adsorbate distance (Figure 18c). In general, electric field is more intense for low cation-water coordination numbers and short distances, in excellent agreement with a recent experimental study of cation effect on eCO_2R on Au.[370] The employment of a more accurate model of the catalyst/electrolyte interface revealed an additional chemical effect of the cation in addition

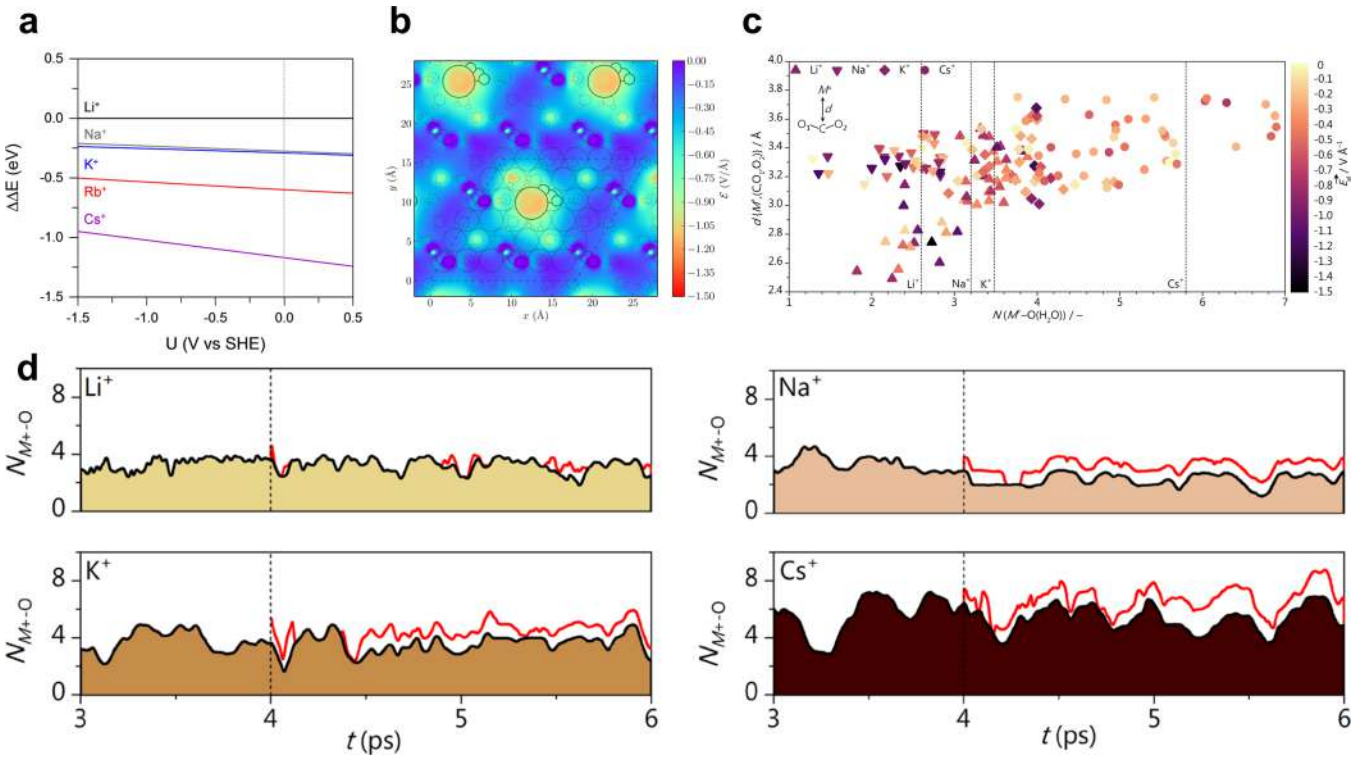

Figure 18: Role of metal cations in eCO_2R. **a**, The thermodynamic driving force for cation accumulation at the OHP of a Cu(111) electrode is stronger for alkali cations with larger ionic radius.[170] **b**, Cation-induced electric field on the z-plane corresponding to a CO_2 adsorbed on a (6×6) Ag supercell. K^+ coverage account for $\frac{1}{36}$ ML. Solvent atoms are indicated as dashed circles, whilst cation, CO_2, and Ag atoms are highlighted as black circles.[44] **c**, Dependence of alkali cation-induced electric field on solvation shell (x-axis) and cation-adsorbate average distance (y-axis).[45] **d**, Cation-water (filled area) and cation-CO_2 (red line) coordination number during 2 ps of AIMD simulations on a 4-layer $(3\sqrt{3}\times3\sqrt{3})$ Au(111) model with 72 water molecules and 1 alkali cation.[45] Adapted with permission from Ref. 170 (Copyright 2017 Americal Chemical Society), Ref. 44 (Copyright 2016 Americal Chemical Society), and Ref. 45 (Copyright 2021 Springer Nature) respectively.

to the mean-field electrostatic stabilization previously discussed (Equation 28).[44,171] In fact, we applied AIMD simulations on a $(3\sqrt{3}\times3\sqrt{3})$-$R30°$ Au(111) supercell with 72 explicit water molecules pre-optimized for a Pt(111)/water system (20 ps).[22,45] The Au/water system underwent an initialization of 2 ps AIMD simulation (1 fs time step) to optimize the solvation layer, then an additional 2 ps upon introduction of an alkali cation (Li^+, Na^+, K^+, and Cs^+) close to the surface, and a final optimization for 2 ps upon adsorption of a CO_2 molecule in the vicinity of the cation. The datasets related to this work are available on the ioChem-BD

database.[371]

By assessing the cation-oxygen radial distribution function and defining cation local coordination shell during the AIMD simulations on the Au/water/cation/CO_2 system, we observed a local coordination between cation and adsorbate (Figure 18d), which was more frequent for weakly hydrated cations, such as K^+ and Cs^+.[45] Upon coordination, a short-range $cat^+ \cdots O(CO_2)$ interaction occurs, which accounts for a stabilization of CO_2 adsorption by 0.5 eV. This promotional effect is rather independent of the cation species, thus this evidence confirms that CO_2 reduction activity trends must be attributed to accumulation processes rather than distinct cation stabilization.[170] While CO_2 adsorption is endergonic by $\sim +0.8$ eV for the cation-free case, this process becomes almost exergonic if facilitated by a neighboring cation, thus supporting the experimental results from Prof. Koper's group that metal cations are key to enable eCO_2R on gold, silver, and copper. The promoting effect of cation is highlighted as well by (1) the decrease of the O-C-O angle, $\alpha \sim 130°$, which indicates activation of the CO_2 molecules, (2) and the enhancement of the first electron transfer from the surface. As a consequence of the theoretical and experimental evidences reported in the study,[45] an updated mechanism for CO_2 reduction to CO was proposed, involving the instrumental role of cation in stabilizing the CO_2^- intermediate at the surface prior to protonation to COOH. Besides, cation-CO_2 coordination number was proposed as a unique descriptor for eCO_2R activity and very recently its validity was extended to bi- and trivalent cations as well.[42] In addition to CO_2 adsorption, cation stabilization effect may be crucial for C-C coupling as well.[147]

Overall, cation accumulation at the OHP,[170] mean-field effects,[171] and localized electrostatic stabilization[44,45] are the three main phenomena ruling cation effect on CO_2 reduction, and must be properly accounted in theoretical modeling. While accumulation and mean-field effects rule CO_2 reduction activity and any trends based on cation ionic radius, local electrostatic interactions are key for enabling the overall process by stabilizing crucial reaction intermediates. These considerations support the accuracy of semi-quantitative predictions

on eCO_2R activity trends from theoretical models based solely on concentration and mean-field phenomena. For instance, Ringe *et al.* applied a 1-dimensional continuum electrolyte model,[171] the size-modified Poisson Boltzmann approach,[372] to describe the induced charge density at the density at a given cation concentration and applied potential, Equations 31, 32. ϵ_{bulk} is the bulk dielectric permittivity, z_i and C_i are respectively ionic charges and concentrations (negative sign for anions, positive for cations), F and R the Faraday and Ideal Gas constant, T the temperature, and Φ the electrostatic potential within the electrical double layer. χ_0 represents the ion-occupied volume fraction given by $2C_{\text{bulk}}a^3\text{N}_\text{A}$ where N_A stands for the Avogadro constant and a is the lattice cell length in the statistical model, *i.e.* the ion diameter in this case. Equation 32 can be solved applying Dirichlet boundary conditions at the end of the diffusion later ($\Phi = 0$ for $x = x^\infty = 80$ μm) and Robin boundary condition at the electrode surface, Equation 33, where σ is the cation-induced surface density, Φ^M and $\Phi^{\text{M,PZC}}$ are respectively the electrode potential of the metal relative to the bulk electrolyte and its potential at the PZC. C_{gap} stands for the interfacial Helmholtz capacitance. By solving Equations 31, 32, and 33 the authors derived the dependence of surface density σ on potential Φ and ion size a. The variation of Gibbs free energy of CO_2 and OCCO adsorption driven by the increased electronic density at the surface (Equation 28) was obtained through density functional theory, so it was possible to estimate CO and C_2 partial current density as a function of σ. Finally, by coupling continuum model and DFT, the authors mapped the dependence of eCO_2R activity and C_2 selectivity on the ion size a for silver and copper, showing excellent agreements with experimental reports.[171]

$$\epsilon_{\text{bulk}}\frac{\text{d}^2\Phi}{\text{d}x^2} = \sum_i z_i C_i[\Phi] \tag{31}$$

$$C_\pm[\Phi] = C_{\text{bulk}}\frac{\text{e}^{\pm\frac{z_i\text{F}\Phi}{\text{R}T}}}{1-\chi_0+\chi_0\cosh\left(\frac{z_i\text{F}\Phi}{\text{R}T}\right)} \tag{32}$$

$$\sigma = \epsilon_{\text{bulk}}\frac{\text{d}\Phi}{\text{d}x} = C_{\text{gap}}[\Phi^\text{M} - \Phi^{\text{M,PZC}} - \Phi(x=0)] \tag{33}$$

In addition to CO_2 reduction, cation effects have been reported as well for hydrogen evolution at alkaline pH, albeit showing different trends depending on the catalysts. HER has been observed to decrease following the alkali group for Pt and Ir, whilst this trend overturns for Au and Ag.[373] Prof. Koper and his research group recently proposed a novel mechanism to rationalize such effect on transition metals, based on theoretical and fundamental insights.[42,160,161,374,375] By increasing cation concentration at a constant bulk pH, a reaction order ~ 0.6 of HER on cation concentration was observed at bulk pH = 11 on a gold electrode. However, such dependence turned negligible (reaction order ~ 0) for pH = 12 and lead to a negative reaction order of around -1 at pH = 13. Besides, *in situ* SERS detected a red shift of the vibrational band related to H adsorption on gold when the bulk pH increases, thus suggesting changes in hydrogen binding energies. Thus, both evidences hint at the occurrence of a convoluted effect between electrolyte pH and cation concentration, where both parameters enhance water reduction to a certain extent.[160] Overall, Goyal *et al.* proposed cation to promote the rate-determining Volmer step for water reduction on gold, Equation 34, by stabilizing the transition state associated with the reaction as in Equation 35. Later, McCrum *et al.* extended the validity of this scheme as well to Pt, for which Na^+ enhances water dissociation as well.[374] In the same study, the authors unveiled the role of OH^- binding energy to tune HER activity, predicting a 3-D volcano plot for HER activity using $\Delta G_{*\mathrm{OH}}$ and $\Delta G_{*\mathrm{H}}$ as suitable descriptors.

To rationalize the convolution between cation and pH effects, Goyal *et al.* assumed enhancement of HER at pH = 11, saturation of such effect at pH = 12 due to achievement of maximum concentration of cations at the surface, and a site blocking effect for pH = 13, motivating the negative reaction order of ~ -1.[161] Based on these hypothesis, the authors derived a general empirical rate (ν) law, Equation 36, where k is the rate constant (we employ here the standard notation, even though the rate depends on the temperature), α the transfer coefficient, F and R the Faraday and Ideal gas constants, U the applied potential vs the standard potential of the reaction, T the temperature, $\Gamma_{\mathrm{cat,surf}}$ and $\Gamma_{\mathrm{cat,max}}$ respectively

cation surface concentration and its saturation value, and γ an empirical reaction order of HER on $\Gamma_{\mathrm{cat,surf}}$. Hence, for low cation concentrations at the surface, *i.e* $\Gamma_{\mathrm{cat,surf}} \ll \Gamma_{\mathrm{cat,max}}$, Equation 36 correctly reproduces en empirical reaction order of γ. Instead, the correlation between pH and cation surface coverage can be described through the dependence of cation coverage on the effective potential U_{eff} and the bulk cation concentration $C_{\mathrm{cat,bulk}}$, assumed to follow a Frumkin isotherm in Equation 37. In this equation, K is the standard equilibrium constant for cation adsorption at the surface and g is the Frumkin interaction parameter, higher than 0 in case of repulsion between adsorbates. Since experimental results were obtained at constant potential U vs the RHE, the potential at the PZC for the Au electrode, U_{pzc}, shifts positively for increasing surface pH ($\mathrm{pH_{surf}}$), thus U_{eff} exhibits a negative pH-dependent offset, Equation 38. Recently, Monteiro *et al.* rationalized experimental evidences of cation effects on Pt and Au by defining a generalized cation promotion/inhibition scheme based on the interaction between specific transition metal and alkali cation.[375]

$$* + \mathrm{H_2O} + \mathrm{e^-} \rightarrow *\mathrm{H} + \mathrm{OH^-} \tag{34}$$

$$* + \mathrm{H_2O} + \mathrm{e^-} + \mathrm{cat^+} \rightarrow *\mathrm{H} - \mathrm{OH}^{\delta-} \cdots \mathrm{cat^+} + (1-\delta)\mathrm{e^-} \rightarrow *\mathrm{H} + \mathrm{OH^-} + \mathrm{cat^+} \tag{35}$$

$$\nu = k\left(1 - \frac{\Gamma_{\mathrm{cat,surf}}}{\Gamma_{\mathrm{cat,max}}}\right)\mathrm{e}^{-\frac{\alpha \mathrm{F} U}{\mathrm{R}T}}\Gamma_{\mathrm{cat,surf}}^{\gamma} \tag{36}$$

$$\frac{\Gamma_{\mathrm{cat,surf}}}{\Gamma_{\mathrm{cat,max}} - \Gamma_{\mathrm{cat,surf}}} = K\mathrm{e}^{\left(-\frac{\mathrm{F}(U-U_{\mathrm{pzc}})}{\mathrm{R}T}\right)}\mathrm{e}^{\left(-g\frac{\Gamma_{\mathrm{cat,surf}}}{\Gamma_{\mathrm{cat,max}}}\right)}C_{\mathrm{cat,bulk}} \tag{37}$$

$$U_{\mathrm{eff}} = U - U_{\mathrm{pzc}} = U - U_{\mathrm{pzc}}(\mathrm{pH} = 0) - \mathrm{k_B}T\ln 10\mathrm{pH_{surf}} \tag{38}$$

Finally, a collaborative experimental-computational study between our and Prof. Koper's research groups extended the previous insights on alkali cations to multivalent species, assessing cation effects on both $\mathrm{eCO_2R}$ and HER on polycrystalline gold at pH = 3. The DFT datasets related to this work are available on the ioChem-BD database.[376] Experimentally, activity and onset for water reduction were observed to correlate with cation acidity, defined

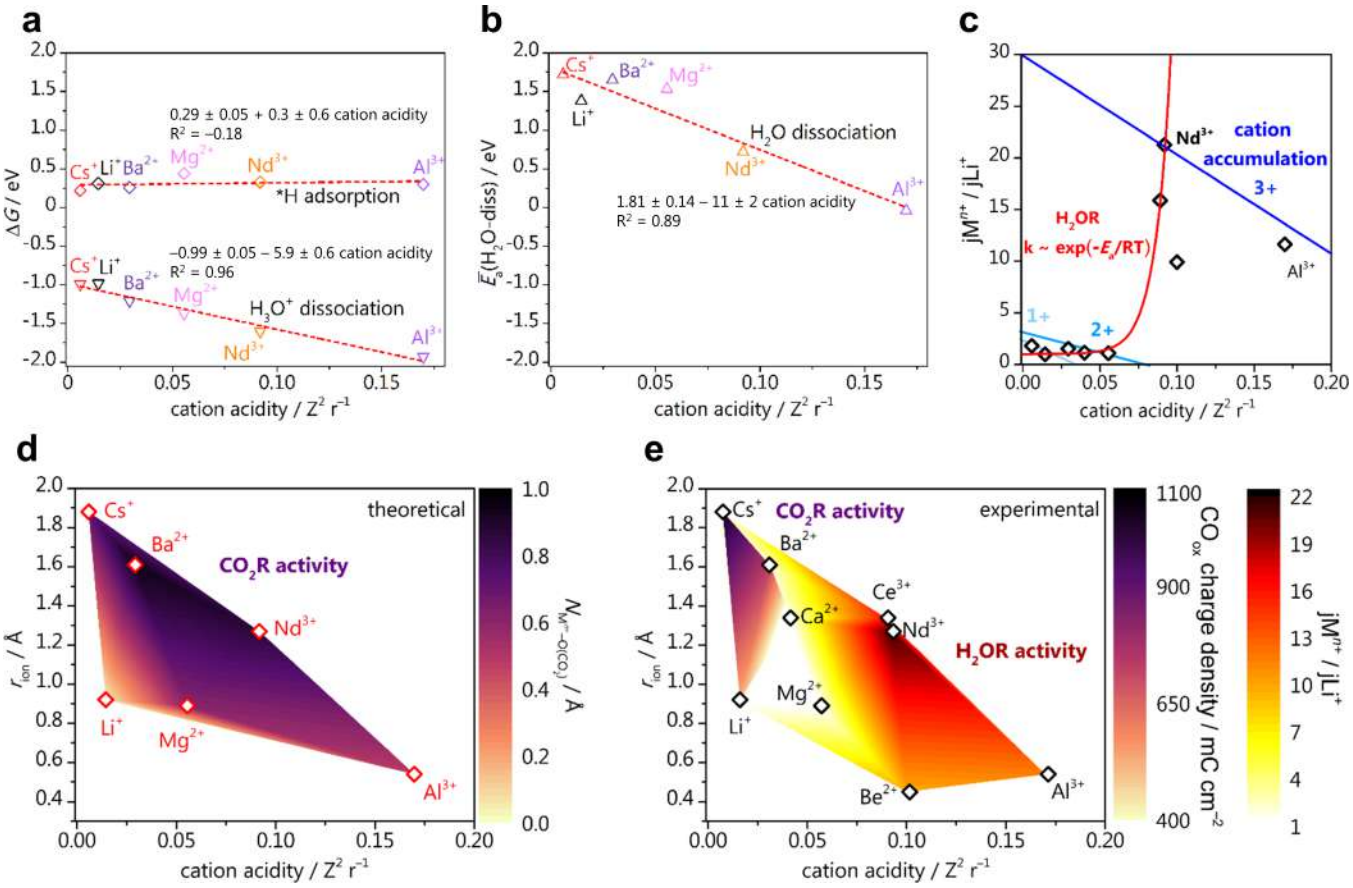

Figure 19: **a**, Gibbs free energy for *H adsorption (diamonds) and H_3O^+ dissociation (down-pointing triangles) vs cation acidity. **b**, Activation barrier for water dissociation (up-pointing triangles) vs cation acidity. **c**, Normalized activity for water reduction estimated from experimental data vs cation acidity. The qualitative fit decouples the contributions from water dissociation kinetics (red) and cation accumulation (shades of blue) for alkali (1+), divalent (2+), and trivalent (3+) species. **d**, Theoretical prediction of eCO_2R performance for different cationic species using cation-CO_2 coordination number as activity descriptor. **e**, Heat map of CO_2 reduction (purple shades) and H_2O reduction (red shades) performances at high overpotential vs cation ionic radius and cation acidity.[42] Adapted with permission from Ref. 42 (Copyright 2022 American Chemical Society).

as the ratio of charge and ionic radius, while no effect was found on proton reduction. Thus, significant eCO_2R activity in presence of acidic cations was reported only at low applied potential, for negligible water reduction, while Ba^{2+} and Cs^+ accounted for the highest CO formation rates at high overpotential. To rationalize these evidences, we applied a similar computational framework as for our previous study,[45,371] *i.e.* AIMD simulations at $T = 300$ K on a gold supercell with explicit solvation previously optimized and different cations (Li^+,

Cs^+, Mg^+, Ba^{2+}, Al^{3+}). Electric field effects ($\vec{E} = -0.3$ V Å^{-1}, roughly corresponding to -0.7 V vs SHE) and realistic cation concentration (2 cations, 0.07 ML coverage, 1.0-1.6 M) were assumed in the model, which was validated by comparing experimental and theoretical values for cation coordination shell and hydrated radius.[362,377]

The explicit insertion of electric field effects enables the observation of electrostatic repulsion among acidic cations, suggesting that nonacidic cations accumulate more at the interface. Specifically, we observe that the gradient of the thermodynamic driving force for cation accumulation correlates with cation acidity, which then acts as a proper descriptor of cation trends among different species. As for the rationale behind specific cation promotion of hydrogen evolution, we assessed the energetics related to the dissociation of H_3O^+ and H_2O, expected to be the proton sources at acidic and neutral/alkaline surface pH,[41] and *H adsorption, typically assumed as the key descriptor for HER activity.[11] H_3O^+ dissociation is kinetically barrierless and thermodynamically favored for any assessed cation, and the Gibbs free energy related to this step scales linearly with cation acidity, Figure 19a. Instead, *H adsorption is not affected by the change of cation (Figure 19a), thus both these evidences motivate the absence of any specific cation effect on proton reduction. The activation energy for water dissociation strongly correlates with cation acidity, ranging from E_a larger than 1.5 eV for Cs^+ till negligible activation on acidic cation (Figure19b). Thus, cation acidity rules water reduction due to its impact on cation accumulation and water dissociation kinetics, leading to the definition of a HER activity volcano plot (Figure 19c). Alkali and bivalent cations exhibit similar HER activity since they account for low water dissociation rate, thus cation accumulation at the interface has a negligible promoting role due sluggish kinetics. Instead, acidic cations enable high H_2O dissociation rates, thus HER activity is mainly driven by the cation accumulation trend within the trivalent group, motivating the highest performance for Nd^{3+}, present at higher surface concentrations than Al^{3+}. In addition to defining a general mechanism for cation effect on water reduction, this study highlights the interplay between promotional effects on CO_2R and HER and the need for an

integrated assessment of both contributions. In fact, even though the validity of cation-CO_2 coordination number was here generalized to multivalent cations (Figure 19d) it serves its scope only at low overpotential, where water reduction was negligible, Figure 19e.

7.2 Anion effects

Anion species in the electrolyte can poison the electrode surface under cathodic conditions,[174,175] limiting the performance of optimized devices such as Gas Diffusion Electrode due to salt formation at the catalyst layer.[15,176] Prof. Rossmeisl and his group have successfully employed the GCHE framework (Section 2.2)[57,58] to quantify poisoning effects in CO_2 reduction and identify the stability region of adsorbed species vs applied potential and bulk pH,[174,175] showing excellent agreement with experimental reports.[378]

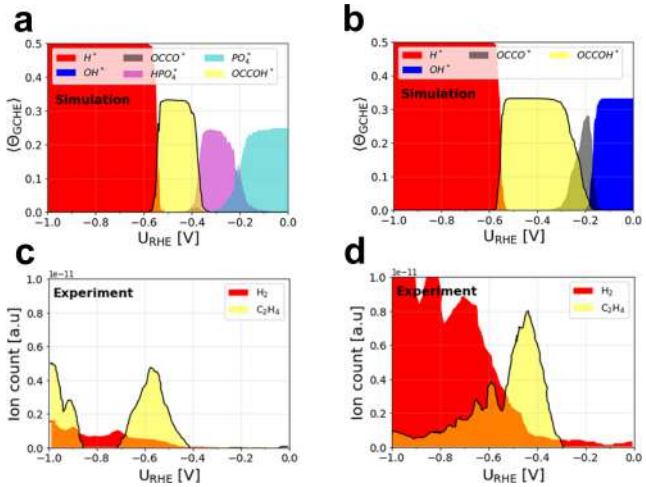

Figure 20: Surface poisoning of anions during electrocatalytic reactions. **a-b**, Simulated coverage for adsorbed species on Cu(100) at pH = 7 (left) and pH = 13 (right) derived from interface phase diagrams estimated *via* the GCHE formalism.[57,58] **c-d**, CO reduction products on Cu(100) in a H_3PO_4 (pH = 7, left) and NaOH (pH = 13, right) electrolyte, respectively measured by Online Electrochemical Mass Spectrometry (OLEMS).[378] Adapted with permission from Ref. 174 (Copyright 2019 American Chemical Society).

The first application of the GCHE to assess explicit electrolyte effects aimed at rationalizing the pH dependence of CO reduction on copper and its lower onset potential than HER, reported in a previous experimental work for phosphate (pH = 7) and NaOH (pH

= 13) aqueous electrolytes.[378] The authors carried out AIMD simulations on copper facets with explicit water molecules, electrolyte species, and reaction intermediates.[174] Different *H and *OH coverages were sampled from zero to half coverages, while *H_xPO_4, *OCCO, and *OCCOH were introduced individually in the supercell. The resulting configurations generated by AIMD were then screened through a Boltzmann weighting of the energies, thus allowing to estimate key parameters. In general, *OCCO was reported stable only on Cu(100), because of large stabilization by the solvent. Besides, *OCCO protonation to *OCCOH or *OCCHO was reported more favorable than *H adsorption, thus motivating the lower onset potential for ethylene formation rather than HER. As for the dependence of ethylene selectivity on bulk electrolyte pH, both pH and applied potential were included in the energy of all the AIMD configurations through the GCHE scheme to define interface phase diagrams of the adsorbed species (Figure 20a,b). Besides showing excellent agreements with experimental results at pH = 7 (Figure 20c) and pH = 13 (Figure 20d),[378] simulations suggested that ethylene formation is limited by adsorption of anions (*OH, *HPO_4, *PO_4) in the low overpotential region. Instead, at high overpotential, *OCCOH adsorption is hampered by an increased *H coverage. In the same study, carbonate poisoning was suggested to have a similar role for CO_2 reduction, although carbonate blocked copper facets until larger overpotential than that required for *OH adsorption, thus motivating the difference in activity for CO and CO_2 reduction.[350] As a last conclusion from their study, the authors proposed that the experimental difficulty in observing the $OCCO^-$ intermediates are due to the very tiny potential window where this intermediate is stable before his protonation to *OCCOH. Recently, the same authors carried out a similar investigation of the CO reduction process on Cu(100) and Cu(111), combining voltammetric CO-displacement measurements and AIMD to characterize the Cu/electrolyte interface and the role of phosphate poisoning in tuning CO adsorption properties.[175] *HPO_4 and *PO_4 were suggested as the predominants adsorbed species on Cu(100) and Cu(111) respectively, limiting CO adsorption to more negative potentials.

7.3 Surface pH and bulk mass transfer

The Computational Hydrogen Electrode is a powerful tool to account for bulk pH effects, since this term is explicitly accounted through a linear correction to adsorption energies of intermediates (Section 2.2).[8] Hence, this framework has proven effective in rationalizing experimental evidences from Tafel plot analysis[379] and derive fundamental insights on reaction mechanisms.[349] However, recent technological and conceptual advances allow to measure experimentally the pH within the diffusion layer (the so-called "surface pH" or "local/localized pH"),[380] through the Scanning Electro-Chemical Microscopy (SECM) setup[381,382] (even time resolved),[383] spectroscopic strategies (e.g HCO_3^-/CO_3^{2-} vibrational bands),[369,384] and Rotating Ring-Disc Electrode (RRDE) voltammetry.[385] For cathodic reaction such as CO_2 reduction, pH at the surface was reported to vary up to 5 units from the bulk value due to proton consumption or OH^- generation from eCO_2R and HER,[16] depending on the overall currently density.[384–386] Variation of pH at the surface is only one of the relevant mass transfer effects occurring under electrocatalytic conditions,[387,388] thus models based on solving numerically the Nernst-Plack equations have been developed since the seminal work of Gupta *et al.*[163] Currently, two main theoretical approaches are employed to assess mass transfer within the diffusion layer and its influence on reaction activity and selectivity: (1) numerical solution of modified Poisson-Nernst-Planck (PNP) equations,[164] and (2) multiphysics modeling with finite element methods.[167,389]

As an example of the first framework, Bohra *et al.* investigated the CO_2 reduction process on CO-producing catalysts, such as CO and Au, through a 1D model based on generalized solution of modified PNP equations.[164] Such generalization was needed to account for steric effects happening at realistic electrolyte concentrations. The authors only accounted for CO_2 and H_2O reduction as Faradaic processes at the surface, while water dissociation and bicarbonate/carbonate/CO_2 chemical equilibria reactions were considered within the diffusion layer. The bulk concentration of electrolyte species was assumed constant and estimated from experimental values. Three generalized modified Poisson-Nernst-Planck equations were

considered to model mass transfer within the diffusion layer, Equations 39-41. C_i, $\vec{J_i}$, z_i, D_i, ans a_i are respectively concentration, flux, charge, diffusion coefficient, and effective solvated diameter of the species i. R_i is the rate of production of species i from a p homogeneous reactions between water dissociation and bicarbonate/carbonate/CO_2 equilibria. R, F, N_A are respectively Ideal Gas constant, Faraday constant and Avogadro number, while Φ and T stand for potential vs the point of zero charge of the electrode and temperature. ϵ_0 and ϵ_r are the vacuum and dielectric permittivity of the electrolyte, and ϵ_r is approximated by a continuous function ranging from 80.1 (value for water at room temperature) to 6 (value for water at dielectric saturation).[16]

$$\frac{\partial C_i}{\partial t} = \nabla \cdot \vec{J_i} + \sum_p R_p \tag{39}$$

$$\vec{J_i} = -D_i \nabla C_i - \frac{D_i C_i z_i \mathrm{F}}{\mathrm{R}T} \nabla \phi - D_i C_i \left(\frac{\mathrm{N_A} \sum_{i=1}^{n} a_i^3 \nabla C_i}{1 - \mathrm{N_A} \sum_{i=1}^{n} a_i^3 C_i} \right) \tag{40}$$

$$\nabla \cdot (\epsilon_o \epsilon_r \nabla \phi) = -\mathrm{F} \sum_{i=1}^{n} z_i C_i \tag{41}$$

Equations 39-41 were then numerically solved, assuming the electric field at the OHP as Neumann and Dirichlet boundaries conditions and the predictions from the GNPNP scheme were benchmarked with state-of-the-art models (reaction-diffusion and Poisson-Nernst-Planck). Several key parameters were calculated as continuous functions of applied potentials vs PZC and distances from the OHP: the effective potential, pH, CO_2, cation concentrations, etc.[164] Overall, significant variations of pH were reported already for low current densities ($j = 10$ mA cm^{-2}) together with very intense electric fields at the OHP (-0.7 V Å^{-1}) and low water relative permittivity ($\epsilon_r = 50$) even at mild applied potential (-0.32 V vs PZC).[164]

Veenstra *et al.* mapped CO_2 product distribution with surface pH and applied potential through a joint experimental/computation study.[167] First, they synthesized well-defined microstructured CuO electrodes, generating surface cavities with tunable length through Laser ablation ($L = 0$, 20, 40, 60, 100, 130 μm). Using these cavities as micro-probes for surface

pH, they characterized CO_2 selectivity in a 0.1 M $KHCO_3$ electrolyte. Then, they employed structural geometries and eCO_2R performances as input data for multiphysics 3D modeling through the COMSOL platform to target concentrations and fluxes of key intermediates depending on the local morphology of the electrode. The computational scheme included eCO_2R and HER, chemical equilibria for carbonate species, and diffusion, as in previous models.[163,390] Besides, the model explicitly considered the buffering role of cation hydrolysis suggested by Resasco *et al.*[170] The simulation accounted for three regions: (1) the volume of the surface cavity, (2) eight adjacent cavities to encompass potential contributions from surrounding environment, (3) a diffusion layer with tunable thickness depending on the mass transfer regime, initially set to 50 μm. Bulk concentrations and zero flux for non-reactive species were imposed as boundaries conditions beyond the diffusion layer. Since CO_2 and pH did not show significant variation across the (x, y) planes, the initial 3D model was simplified to a 1D setup, only considering the z-direction. A pH increase up to 3 units was calculated at the end of the cavities, and this effect strongly depended on applied potential and length of the micro-probes. By relating computational estimations with experimental results for eCO_2R selectivity, the authors generated selectivity maps for different reaction products, unveiling the role of surface pH and average CO_2 concentration at the electrode (Figure 21a highlight the case of carbon monoxide and ethylene). These separate analysis were later combined into a general selectivity maps, which lead to remarkable fundamental insights on reaction mechanisms toward C_1, C_2 and C_3 on copper.[167]

Kas *et al.* employed an analogous multiphysics framework to model CO_2 reduction on a GDE with Ag catalyst layer.[389] The 2D model accounted for Butler-Volmer kinetics for both eCO_2R and H_2O,[2] as well as CO_2/bicarbonate/carbonate equilibria reactions within the electrolyte. The input parameters for modeling the GDE were retrieved from experimental characterization.[391] Overall, significant variations of CO_2 concentrations and partial current densities were estimated within the GDE area, both across (x-direction) and along (y-direction) the flow channel (Figure 21b). Whilst the first variation is driven by concentra-

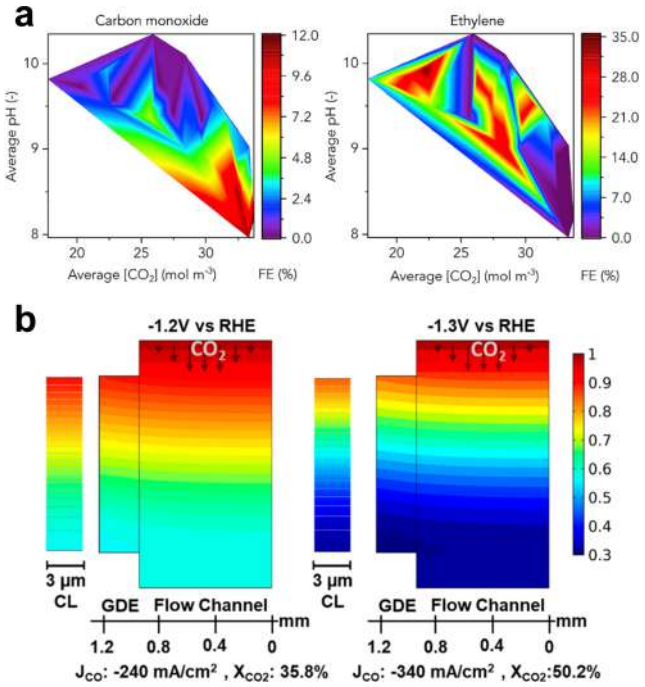

Figure 21: Surface pH and mass transfer effects in electrochemical CO_2 reduction. **a**, Heat maps for CO and C_2H_4 F.E. vs surface pH and CO_2 concentration.[167] White areas correspond to pH/[CO_2] pairs not allowed under the given reaction conditions. **b**, Heat plots of gaseous CO_2 mole fraction in the gas flow channel and gas diffusion electrode for different applied potentials, 5 mL min^{-1} flow rate, and 1 cm^2 electrode area. Data employed in the model, (partial current density j_{CO} and single-pass conversion X_{CO_2}) are defined below each panel, whilst gaseous mole fractions of CO_2 in the catalyst layer (CL) are reported in the inset.[389] Adapted with permission from Ref. 167 (Copyright 2020 Elsevier) and Ref. 389 (Copyright 2021 American Chemical Society).

tion gradients due to CO_2 consumption at the catalyst layer, the second is due to the forced convective flow from the inlet. Instead, CO_2 concentrations and partial current densities were almost constant within the catalyst layer due to its small thickness (3 μm). Nevertheless, dramatic pH variations were calculated within the catalyst layer, leading to pH $\sim$ 13 for current densities higher than 200 mA cm^{-2} and reduction of anions diffusion thickness from 200 μm to few μm. Finally, the COMSOL model highlighted the existence of an interplay between applied potential, current density, and outlet concentrations. While high CO_2 flow rate leads to increased production rate due to enhanced mass transfer, it also determines larger ohmic loss and operational costs and lower single-pass conversions, thus limiting the industrial exploitation of such operating conditions.[199]

As a final remark in this section, we highlight that mass transfer effects can be crucial under well-defined conditions and may determine selectivity shifts due to interplay between different reaction precursors. Recently, Marcandalli *et al.* rationalized the Bell-shaped Faradaic efficiency of eCO_2R to CO by identifying three different HER regimes (Figure 22a).[339] Through mechanistic investigations by a RRDE voltammetry, HER was suggested to occur through carbonic acid reduction at very low overpotentials. At more negative potential H_2CO_3 reduction is presumably diffusion-limited, hence bicarbonate becomes the relevant proton donor. Until -0.5 V vs RHE, CO_2 reduction to CO is increasingly promoted, due to the higher kinetics for this process than for HER. Lastly, water reduction initiates at more negative potentials and HER increases to the detriment of eCO_2R, due to the higher kinetics for HER in this regime. Thus, ideal catalysts for eCO_2R should be optimized within the low overpotential region (≤ -0.5 V vs RHE), where this process is significantly more favorable than HER from bicarbonate and carbonic acid reductions.

In addition to this elegant work, the same research group demonstrated by Differential Electrochemical Mass Spectroscopy (DEMS) that HER can be entirely suppressed on gold under mildly acidic pH due to proton consumption by OH^- generated by eCO_2R (Figure 22b).[340] Hence, Faradaic efficiencies close to 100% can be achieved by carefully tuning CO_2 and H^+ surface concentrations so that excess OH^- from eCO_2R is fully neutralized by protons and does not undergo CO_2/CO_3^{2-} homogeneous reaction. Both fundamental approaches propose mass transfer optimization strategies which are scalable to industrial devices, as demonstrated in Refs. 179,359, thus highlighting even further that these are crucial parameters in electrocatalytic reactions and must be properly accounted for.

8 Application of Machine Learning

Since the advent of machine learning (ML) in the field of catalysis, over the past few decades this technique has been been used to address shortcomings of atomistic simulations, such as

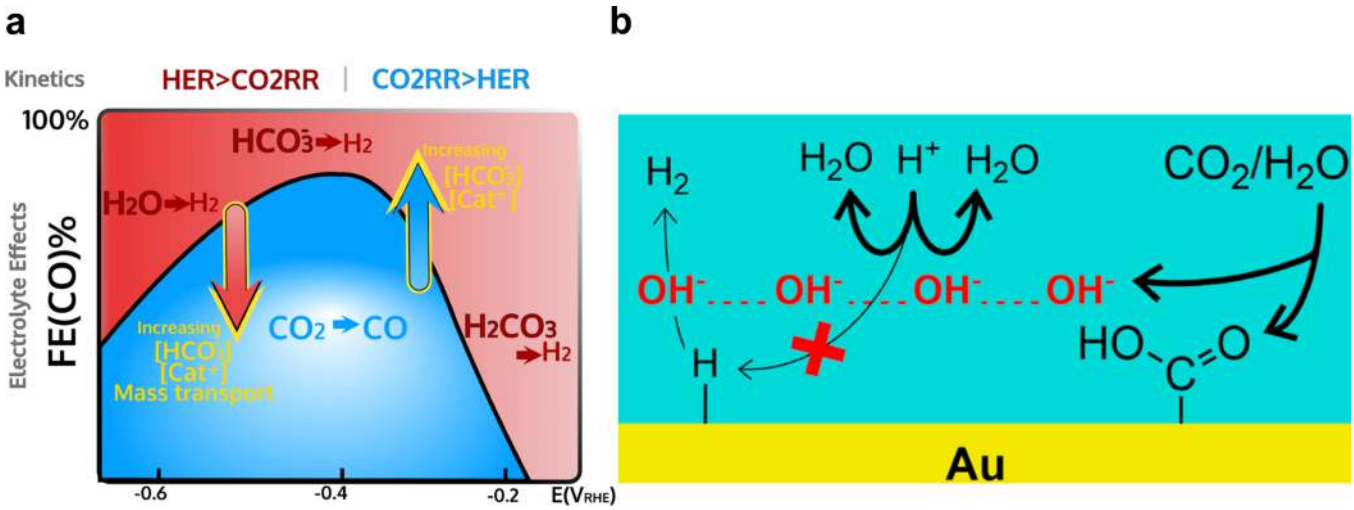

Figure 22: **a**, Bell-shaped Faradaic efficiency of CO_2 reduction to CO on a gold electrolyte versus applied potential on bicarbonate electrolyte. Depending on the cathodic bias, carbonic acid, bicarbonate, and water are the main protons donors for HER.[339] **b**, CO_2 partial pressure suppresses hydrogen evolution by consuming protons at the surface to form water, leading to F.E close to 100% for CO_2 reduction on gold in acidic pH.[340] Adapted with permission from Ref. 339 (Copyright 2021 American Chemical Society) and Ref. 340 (Copyright 2021 American Chemical Society).

quantum mechanical (QM) and molecular mechanics (MM) methods.[392] On one hand, QM-based simulations are accurate and transferable, yet they are applicable only to small system sizes and short time scales. On the other hand, empirical MM-simulations are developed *ad hoc* for specific systems and thus are typically not transferable. As defined by Morawietz and Artrith in a nice recent review,[392] QM-based machine learning aims at increasing the computational efficiency of QM-based methods, without losing their transferability. Applications of machine learning to electrocatalysis usually falls into one of these four scopes:

1. Prediction of catalytic properties from datasets obtained through QM-based methods. This strategy consists of the automatic generation and analysis of QM data through ML or training of ML methods over QM data to predict relevant parameters and trends.

2. Extension of the range of applicability of QM-based methods to reach larger simulation cell size and time scale. This approach is based on the development of machine learning atomistic potentials to achieve analogous accuracy as QM-strategies.

3. Inverse Design, inversion of atomistic simulations (or experimental data) to extract atomic structures from a given set of properties.

To date, application of ML in the field of eCO_2R has been mainly devoted to pursuing strategy (1), *i.e.* material discovery and data analysis, as we will briefly mention below. As a successful example of integration of both approaches, we cite the work by Ulissi *et al.*,[393] where thermodynamic/kinetic Linear Scaling Relationships and automatic identification of rate-determining steps were applied to study reaction of syngas to CO_2, water, methane, methanol, acetaldehyde, and ethanol. For additional examples and a more in-depth review over these topics, we refer the readers to two recent reviews by Zhang *et al.*[394]and Mistry *et al.*[262] Instead, we here focus on the development of ML potentials to enhance the space and time scales of QM-simulations, strategy (2) discussed in Section 8.2), and data-driven structural analysis, strategy (3) discussed in Section 8.2. Finally, in Section 8.4 we give a short outlook on the future challenges in the field.

8.1 Material discovery and data analysis

In one of the first application of ML to eCO_2R, Li *et al.* designed a framework to predict limiting potential for CO_2 reduction to C_1-C_2 products from $\sim$ 250 *ab initio* CO adsorption energies on (100)-terminated multimetallic Cu catalysts.[395] The properties of the adsorbing sites were parameterized based on their electronegativity and generalized coordination numbers and these parameters plus *ab initio* data were employed as input for a neural network with 75% of the dataset as training set and 25% for testing the model. Finally, linear scaling relationships were used to estimate binding energies of other C_1-C_2 intermediates from CO adsorption energy and consequently to define a list of promising alloys with mild CO adsorption, as Cu-Ni-Cu_3Y, Cu-Ni-Cu_3Sc, Cu-Rh_3Ti, Cu-Rh-Cu_3V, and Cu-RH-Cu_3Mo.[395] The same research group applied a similar approach to screen over 1000 model alloys and calculate *CO and *OH binding energies on these structures, which were later used to predict reactivity towards methanol oxidation.[396] Independently, Ulissi, Sargent, and co-workers ap-

plied ML methods to screen through large number of intermetallic alloy compositions using CO binding energy as a descriptor for catalytic activity,[397] and eventually predicted Cu-Al alloys to contain multiple surface orientations with almost optimal CO binding energies.[398] The proposed Cu-Al compositions were then tested under eCO_2R conditions and showed very high Faradaic efficiencies for ethylene, close to 85%.

8.2 Development of machine learning atomistic potentials

Since the pioneering works of Behler, Parrinello, and co-workers,[399,400] atomistic potentials generated through neural network have been successfully employed in electrocatalysis, as nicely reviewed in Ref. 392. Representation through Neural network of potential-energy surfaces as a function of the atomic positions has enabled faster assessment of different electrocatalysts, such as supported metal nanoparticles,[401]metal clusters on oxides,[400] Cu/Au nanoparticles.[402,403] This approach has been extended to fully ML-based[211] or hybrid molecular dynamics simulations,[403] in which ML is employed on limited numbers of MD snapshots to predict relevant properties of the system.[404] In this section, we highlight one of the first applications of neural network atomistic potentials to large size ternary system as Cu/ZnO,[400] while we refer the reader to two reviews by Behler for detailed insight into the mathematical formalism.[405,406]

Cu/ZnO materials have been extensively studied due to their reactivity for thermal CO_2 hydrogenation to methanol[407] and selectivity for eCO_2R toward ethanol.[408,409] Nevertheless, an adequate computational assessment of defects, atomic rearrangements, and local stoichiometry is hindered by the large configuration space required and the low computational efficiency of DFT simulations. Thus, Artrith, Hiller, and Behler developed a framework to obtain neural network atomistic potentials from DFT energies of about 100000 well-defined Cu and ZnO structures, such as clusters, bulk, and surfaces. Their approach was validated first individually on Cu and ZnO. Surface energies estimated through NN-potentials for low index Cu facets laid within less than 5 meV $Å^{-2}$ from DFT values and bulk properties of

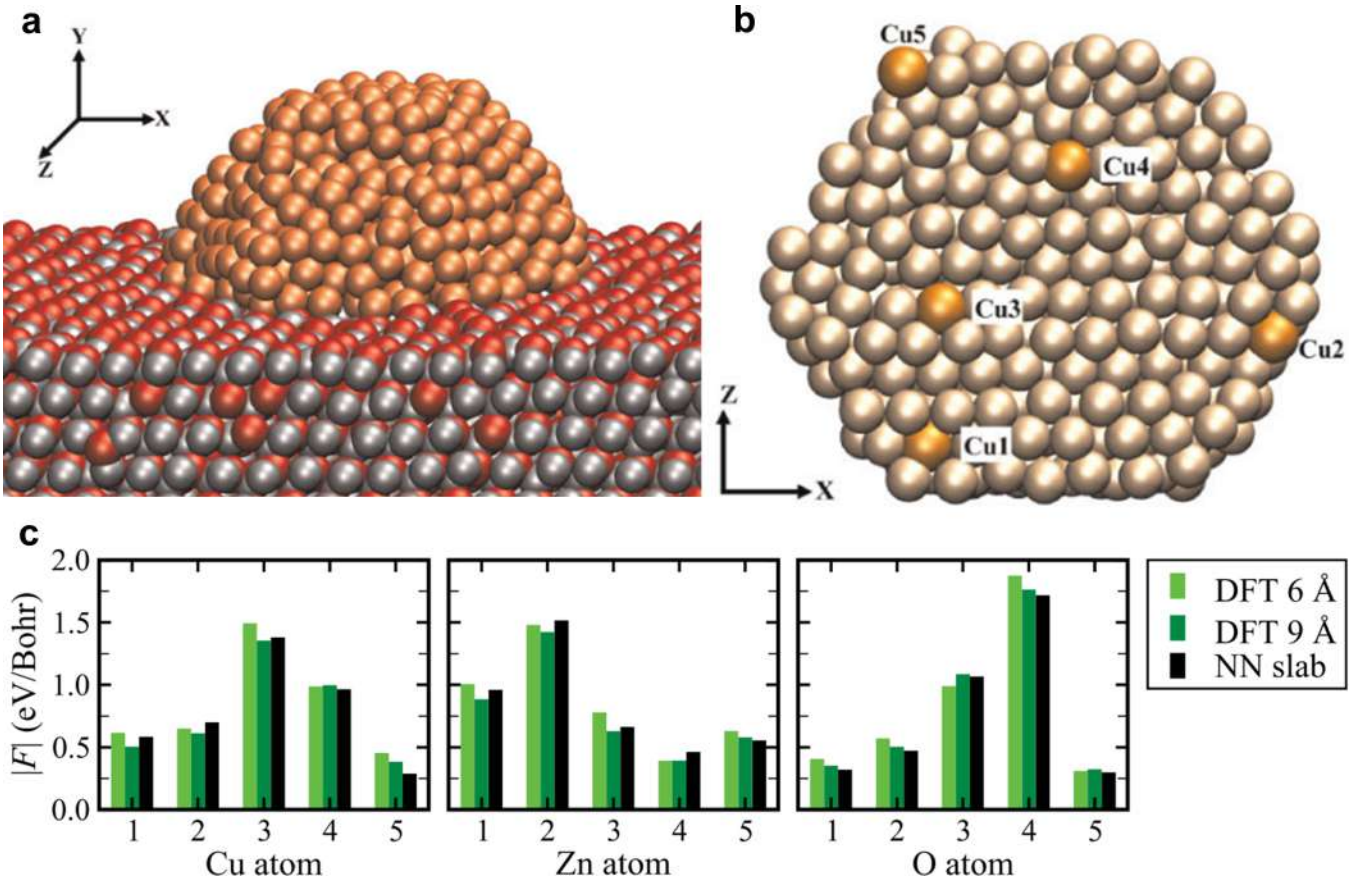

Figure 23: **a**, Snapshot of molecular dynamics simulation at $T = 1000$ K of Cu_{612} cluster on $ZnO(10\bar{1}0)$ surface. **b**, bottom-view of Cu cluster and selected sites at the Cu/ZnO interface. **c**, Neural network forces acting on selected atoms at the $Cu(111)/ZnO(10\bar{1}0)$ vs DFT forces obtained for clusters centered at these atoms with radius of 6 Å and 9 Å respectively.[400] Adapted with permission from Ref. 400 (Copyright 2013 Wiley-VCH).

ZnO were reproduced in excellent agreement as well. Besides, NN- and DFT-forces were equivalent for both systems. After benchmarking the neural network model, the potentials developed along the study were employed to simulate the interface between Cu and ZnO, modeled as a Cu_{612} adsorbed on $ZnO(10\bar{1}0)$, Figure23a. Since the overall system contained 7524 atoms, its assessment through standard DFT would have been prohibitive instead. Local distortion was obtained through a NVT molecular dynamics simulation at 1000 K and five atoms at the interface were selected for each species (Cu, Zn, O), as shown in Figure23b for Cu. Comparison between NN-potential forces and DFT-forces for these sites confirmed once more the robustness of the framework (Figure 23c), suggesting a potential generalization

beyond ternary systems toward the inclusion of adsorbates.[400]

8.3 Inverse Design to extract structural data

As introduced before, machine learning can assist the assignment of fingerprints from *in situ Operando* characterization techniques and the consequent derivation of key structural properties for disordered systems,[410] thus is increasingly employed in materials science.[411] To mention a meaningful example of this *inverse design* strategy, Timoshenko *et al.* applied

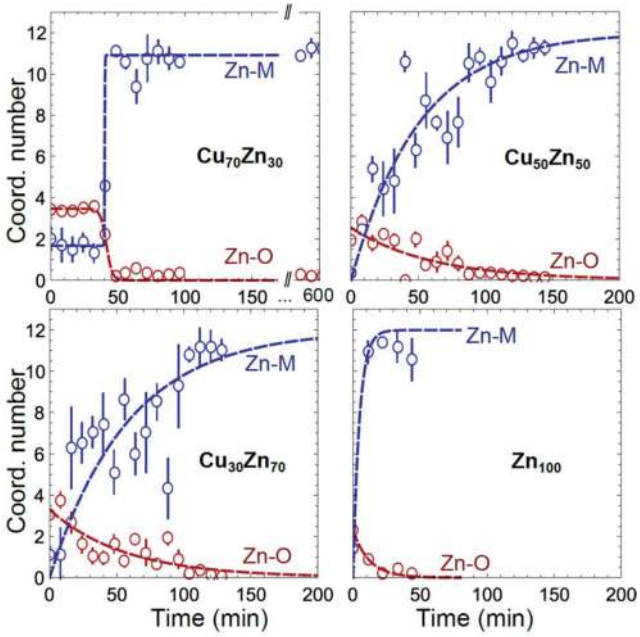

Figure 24: Time-dependent Zn-O and Zn-M (M=Zn-Cu) coordination numbers as extracted by neural network from time-dependent Zn K-edge EXAFS data for CuZn and Zn_{100} nanoparticles.[412] Adapted with permission from Ref. 412 (Copyright 2020 The Royal Society of Chemistry with Creative Commons Attribution 3.0 Unported Licence[413]).

neural network to a set of Extended X-ray Absorption Fine Structure (EXAFS) data to extract structural information for CuZn nanoparticles under CO_2 reduction.[412] By training the NN with theoretical spectra for a copper foil, Cu_2O, CuO, and $Cu(OH)_2$, the authors could reproduce experimental radial distribution function with excellent accuracy. After having validated the methodology, Cu-O, Cu-Cu, and Cu-Zn radial distribution functions were extracted from experimental Cu K-edge EXAFS spectra recorded for as-synthesized

CuZn nanoparticles and catalyst after 1-7 hours of continuous CO_2 reduction. The authors tracked the variation of Cu-Cu/Zn distances over time as well as the coordination number for Zn-Cu/Zn and Zn-O (Figure24). These structural properties were finally employed to rationalize the overall performance of the catalyst.[414]

8.4 Outlook on machine learning

Even though ML techniques are certainly promising in the field of computational modeling of eCO_2R reaction, its application is still limited. Thus, further efforts are needed to employ these novel techniques within a consistent and benchmarked framework. Since the development of a general set of protocols facilitates future potential advances, we endorse here the list of best practices proposed in a recent perspective article by Artrith *et al.*[415] For simplicity, we report the main points below.

1. **Data sources**. The available data sources should provide high quality, quantity, and diversity. Datasets should be stored on FAIR databases (see for instance ioChem-BD[416–418] the Materials Project[419] and CatApp[420]).

2. **Data cleaning**. Data upload on accessible databases should involve cleaning steps to ensure that all the stored data are reusable. The cleaning steps should be properly described and preferentially applied through a semi/full automatic workflow.

3. **Data representation**. Different data representations should be considered to select a model and the choice should be properly described, motivated, and validated vs standard features sets.

4. **Model selection**. Since different approaches exist in ML, they should be properly accounted for and the choice of the model should be validated through baseline comparisons with simpler schemes.

5. **Model training and validation**. Parameters for training, validation, and test of the

model should be clearly stated. Besides, data splitting into the three categories should prevent data leakage.

6. **Code and Reproducibility**. The workflow should be reproducible, thus codes and related materials should be freely available in adequate long-term archiving.

Further, in terms of the four scopes previously introduced, material discovery for selective reduction of CO_2 to C_{2+} hydrocarbons and alcohols should proceed hand in hand with determination of reaction mechanisms through multi-scale methods as microkinetic modeling. Successive high throughput screening studies should follow this preliminary assessment of the key reactions steps and intermediates. In our opinion such multi-scale approaches can greatly help the identification of generalized descriptors and increase the success rates towards finding better catalysts and improving the Faradaic efficiencies of various hydrocarbon products. As for the development of atomistic potentials, long-term MD simulations (of the order of nanoseconds) play a crucial role in determining active sites evolving under reaction conditions due to *Operando* restructuring of the catalyst (see Section 3.1). Since assessment of this process through *ab initio* MD simulations is limited to simplified models,[205,210] and may be affected by intrinsic inaccuracies[212] then accelerated ML-MD techniques will likely be determinant. The work from Behler, Artrith, and co-workers towards using artificial neural networks to simulate the potential energy surfaces is a major step in this direction.[392,405,406] Finally, novel techniques from data extraction and inverse design will significantly lower the impact of human biases in analysis of experimental data, thus increasing the overall accuracy of the resulting insights.

9 Conclusion and future challenges

The increasing accuracy of experimental methodologies to characterize electrochemical processes require significant progresses in computational modeling to mimic the full stack or device operation. In line with a terminology previously introduced,[123] *the eCO_2R field needs*

the development of an Operando modeling framework.

On one side, the equations to obtain energies and chemical potentials from first principles simulations need to be more general, including promotional effects as external magnetic fields,[421,422] local surface polarization,[97,210] and specific stabilization from the electrolyte.[45] On the other hand, several issues need to be addressed regarding the materials and operation gap. In many cases, new techniques based on machine learning[423] can help integrate the different scales of the electrochemical processes and can provide strategies for dimensionality reduction, allowing unambiguous determination of descriptors for activity.[424]

Reconstruction, phase transitions, dissolution, and re-precipitation of species evolving from the as-synthesized compound requires the development of new computational models that are able to describe the effects related to stability. Novel methods will certainly benefit from the fast development of ionic potentials and artificial neural networks which will be crucial towards large scale molecular dynamics. The initial results in this field are very promising but the introduction of solvent and electrolyte has not been successfully implemented yet. Moreover, the characterization of pattern distribution and ensembles through graph theory and other ML approaches will be fundamental to identify the most active and selective sites.

Detailed modeling of complex reaction mechanisms, as CO_2 reduction to C_{3+} products, requires significant computational advances toward the automatic generation of reaction networks, through graphs and autonomous energy evaluations with robust workflows which include human analysis of ambiguous calculations (from our own experience these ill-defined datasets account for about 15% of the total). Such frameworks should be preferentially integrated into multi-scale modeling techniques as microkinetic modeling to evaluate the most abundant surface intermediates and selectivity determining steps. Rationalization of pathways and fast evaluation of barriers linking key intermediates are crucial for further analysis of complex reaction networks. ML-based dimensionality reduction schemes can be employed to simplify the overall complexity and go beyond the standard definition of

catalytic descriptors.

Under electrocatalytic conditions, once the potential is applied, the material reacts and the applied bias also affects the solvent/electrolyte. Apart from cathodic/anodic potential, surface polarization is further influenced by the explicit interactions between cations and anions in the electrolyte or by their crossover through the membrane between cathodic and anodic compartments. Mass transfer phenomena both at the electrode/electrolyte interface and at the bulk electrolyte need to be considered for an accurate modeling of the operational device. In this area, microkinetic codes require a better standardization along with the fluid dynamic approaches. However these two approaches currently are difficult to couple, since the engineering programs lack a successful integration of first principles results.

Mapping experiments to computational results and establishing robust structure-activity relationships can only be done through a much closer interplay between experiments and theory, moving from qualitative or semi-quantitative analysis (e.g DFT vibrations for spectroscopy) to more adequate fingerprint identifications. Bridging technologies, like data processing of both experimental and computational datasets through neural network, will be instrumental to merge all the structural information in a seamless framework, thus enabling a successful identification of the active sites.

All these developments can be further steered by storing theoretical and experimental output on FAIR databases to promote reproducibility and reuse of the data. This is much more advanced in the area of first principle modeling where our approach ioChem-BD[416–418] and other initiatives such as the Materials Project,[419] CatApp,[420] etc. are getting momentum, while FAIR storage of experimental data is currently lmited to few platforms (e.g. Zenodo? Generated datasets can be reused for heavy calculations or fast estimates, as we did for modeling the metal/electrolyte interface,[22,42,45] and then further rationalized through machine learning.[28]

Overall, the developments in the field during the last five years have been enormous and yet the main core questions remain open. A multidisciplinary approach, supported by new

researchers educated in the converging areas of Physics, Chemistry, Data, and Materials Sciences, will improve our understanding of the complexity of *Operando* electrochemical processes, hence enabling a full exploitation of fundamental insights in industrial devices.

Notes

The authors declare no competing financial interests.

Biographies

Federico Dattila Dr. Federico Dattila is a postdoctoral researcher in the Catalytic Reaction Engineering for Sustainable Technologies (CREST) group at the Polytechnic of Turin since March 2022. Previously, he worked in the group of Prof. Núria López at the Institute of Chemical Research of Catalonia (ICIQ, Barcelona Institute of Science and Technology, Tarragona, Spain) for FlowPhotoChem (grant-ID: 862453). His research focuses on modeling electrochemical CO_2 and CO reduction on transition metal catalysts. In 2020 he got his Ph.D. in Chemical Science and Technology at the Rovira i Virgili University under the co-supervision of Prof. Núria López and Dr. Rodrigo García-Muelas. During his Ph.D. he carried out two short stayings at the University of Leiden (Prof. Marc Koper's group) and at Avantium Chemicals BV (Dr. Klaas Jan P. Schouten's group). Prior to his Ph.D., he got a M.Sc. in Physics at the University of Turin in 2017, with a thesis on photoelectrochemical cells developed at Chalmers University of Technology (Gothenburg, Sweden).

Ranga Rohit Seemakurthi Dr. Ranga Rohit Seemakurthi is a PROBIST postdoctoral fellow working in the group of Prof. Núria López at Institute of Chemical Research of Catalonia (ICIQ) in Tarragona, Spain. His current work focuses on developing multi-scale models to study the mechanisms for electrocatalytic CO_2 reduction reaction on metal catalysts. He obtained his Ph.D. in 2021 from Chemical Engineering Department at Purdue University (West Lafayette, USA) under the supervision of Prof. Jeffrey Greeley. His thesis work focused on using DFT and microkinetic modeling analysis for improving the catalysts for selective conversion of shale gas to higher value products.

Yecheng Zhou Prof. Yecheng Zhou received the Ph.D. degree in Chemistry under the supervision of Dr. Angus Gray-Weale from The University of Melbourne, Australia, in 2017. After graduation, he has worked in the Department of Physics in Southern University of Science and Technology (Guangdong, China) as a research assistant professor and worked as a postdoctoral researcher in the group of Prof. Núria López at the Institute of Chemical Research of Catalonia (ICIQ), within the Barcelona Institute of Science and Technology (BIST) in Tarragona, Spain). At the end of 2019, he was appointed as an associate professor at Sun Yat-Sen University in China. His research interest is theoretical modeling of defect and surface chemistry in renewable energies, including perovskite and organic solar cells, and electrocatalysis.

Núria López Prof. Núria López has been active in the field of theoretical heterogeneous catalysis for the last 25 years. She obtained her Ph.D. at the University of Barcelona, Spain in 1999. Her post-doctoral studies were carried out in the group of Prof. Jens Nørskov at the Technical University of Denmark. Since 2005 she is group leader of the theoretical heterogeneous catalysis group at ICIQ. She has participated in about 250 publications in the areas of (Photo-Electro) Catalysis and collaborates with experimental groups worldwide.

Acknowledgement

FD and NL thank the financial support from the Spanish Ministry of Science and Innovation (Grants RTI2018-101394-B-I00, "Severo Ochoa Center", MCIN/AEI/10.13039/501100011033) and the European Union (project FlowPhotoChem 862453-FLOWPHOTOCHEM). RRS would like to acknowledge funding from the European Unions Horizon 2020 research and innovation programme under the Marie Skłodowska-Curie grant agreement No. 754510. The Barcelona Supercomputing Center (BSC-RES) and the ioChem-BD database[418] are further acknowledged for having provided generous computational resources and continuous access to generated datasets.

Abbreviations

DFT = Density Functional Theory

LSR = Linear Scaling Relationships

CHE = Computational Hydrogen Electrode

EXAFS = Extended X-ray Absorption Fine Structure

eCO_2R = Electrochemical CO_2 reduction

C_{n+} = Chemical compounds from CO_2 reduction with carbon number $\geq n$.

HER = Hydrogen Evolution Reaction

OER = Oxygen Evolution Reaction

RDS = Rate-Determining Step

ORR = Oxygen Reduction Reaction

SHE = Standard Hydrogen Electrode

RHE = Reversible Hydrogen Electrode

PCET = Proton-Coupled Electron Transfer

ET = Electron Transfer

EDL = Electrical Double Layer

GCHE = Generalized Computational Hydrogen Electrode

ORR = Oxygen Reduction Reaction

PB = Poisson-Boltzmann

kLSR = kinetic Linear Scaling Relationships

tLSR = thermodynamic Linear Scaling Relationships

* = adsorption site

*molecule = adsorbed molecule

PCA = Principal Component Analysis

XPS = X-ray Photoelectron Spectroscopy

EC-ESTM = ElectroChemical Scanning Tunneling Microscopy

pc-Cu = Polycrystalline Copper

OD-Cu = Oxide-Derived Copper

UHV = Ultra High Vacuum

TPD = Temperature Programmed Desorption

XAS = X-Ray Absorption Spectroscopy

COR = CO reduction

TR-SERS = Time-Resolved Surfaced Enhanced Raman Spectroscopy

F.E. = Faradaic Efficiency

GDE = Gas Diffusion Electrode

LEED = Low-Energy Electron Diffraction

NP = Nanoparticle

ML = Machine Learning

NN = Neural Network

MD = Molecular Dynamics

AIMD = Ab Initio Molecular Dynamics

SCC-DFTB = Self-Consistent Charge Density Functional Tight Binding

NVE = Microcanonical ensemble with no changes in moles, volume, and energy

NVT = Microcanonical ensemble with no changes in moles, volume, and temperature

ReaxFF = Reactive Force Field framework

PZC = Point of Zero Charge

ATR-FTIR = Attenuated Total Reflection Fourier Transform Infrared

FTIR = Fourier Transform Infrared

SEIRAS = Surface Enhanced Infrared Absorption Spectroscopy

ATR-SEIRAS = Total Reflection Surface Enhanced Infrared Absorption

PT = Proton Transfer

SDS = Selectivity-Determining Step

H_2OR = Water reduction

MMK = Microkinetic Modeling

CM = Quantum Mechanical

MM = Molecular Mechanics

CMH = Constrained Minima Hopping

OHP = Outer Helmholtz Plane

OLEMS = Online Electrochemical Mass Spectrometry

PNP = Poisson-Nernst-Planck

DEMS = Differential Electrochemical Mass Spectroscopy

FAIR = Findability, Accessibility, Interoperability, Reusability

References

(1) Maheshwari, S.; Li, Y.; Agrawal, N.; Janik, M. J. *Adv. Catal.*; Academic Press, 2018; Vol. 63; pp 117–167.

(2) Bard, A. J.; Faulkner, L. R. *Electrochemical methods: fundamentals and applications - 2nd edition*; John Wiley & Sons, Inc., 2001.

(3) Heptonstall, P. J.; Gross, R. J. K. A systematic review of the costs and impacts of integrating variable renewables into power grids. *Nat. Energy* **2021**, *6*, 72–83.

(4) De Luna, P.; Hahn, C.; Higgins, D.; Jaffer, S. A.; Jaramillo, T. F.; Sargent, E. H. What would it take for renewably powered electrosynthesis to displace petrochemical processes? *Science* **2019**, *364*, 350.

(5) Nitopi, S. et al. Progress and perspectives of electrochemical CO_2 reduction on copper in aqueous electrolyte. *Chem. Rev.* **2019**, *119*, 7610–7672.

(6) Ciamician, G. The photochemistry of the future. *Science* **1912**, *36*, 385–394.

(7) Hori, Y.; Kikuchi, K.; Suzuki, S. Production of CO and CH_4 in electrochemical reduction of CO_2 at metal electrodes in aqueous hydrogencarbonate solution. *Chem. Lett.* **1985**, *14*, 1695–1698.

(8) Nørskov, J. K.; Rossmeisl, J.; Logadottir, A.; Lindqvist, L.; Kitchin, J. R.; Bligaard, T.; Jónsson, H. Origin of the overpotential for oxygen reduction at a fuel-cell cathode. *J. Phys. Chem. B* **2004**, *108*, 17886–17892.

(9) Peterson, A. A.; Abild-Pedersen, F.; Studt, F.; Rossmeisl, J.; Nørskov, J. K. How copper catalyzes the electroreduction of carbon dioxide into hydrocarbon fuels. *Energy Environ. Sci.* **2010**, *3*, 1311–1315.

(10) Abild-Pedersen, F.; Greeley, J.; Studt, F.; Rossmeisl, J.; Munter, T. R.; Moses, P. G.; Skúlason, E.; Bligaard, T.; Nørskov, J. K. Scaling properties of adsorption energies for hydrogen-containing molecules on transition-metal surfaces. *Phys. Rev. Lett.* **2007**, *99*, 16105.

(11) Bagger, A.; Ju, W.; Varela, A. S.; Strasser, P.; Rossmeisl, J. Electrochemical CO_2 reduction: A classification problem. *ChemPhysChem* **2017**, *18*, 3266–3273.

(12) García de Arquer, F. P. et al. CO_2 electrolysis to multicarbon products at activities greater than 1 A cm^{-2}. *Science* **2020**, *367*, 661–666.

(13) Seitz, L. C. et al. A highly active and stable $IrO_x/SrIrO_3$ catalyst for the oxygen evolution reaction. *Science* **2016**, *353*, 1011–1014.

(14) Arán-Ais, R. M.; Scholten, F.; Kunze, S.; Rizo, R.; Roldan Cuenya, B. The role of in situ generated morphological motifs and Cu(I) species in C_{2+} product selectivity during CO_2 pulsed electroreduction. *Nat. Energy* **2020**, *5*, 317–325.

(15) Endrődi, B.; Samu, A. A.; Kecsenovity, E.; Halmágyi, T.; Sebk, D.; Janáky, C. Operando cathode activation with alkali metal cations for high current density operation of water-fed zero-gap carbon dioxide electrolysers. *Nat. Energy* **2021**, *6*, 439–448.

(16) Birdja, Y. Y.; Pérez-Gallent, E.; Figueiredo, M. C.; Göttle, A. J.; Calle-Vallejo, F.; Koper, M. T. M. Advances and challenges in understanding the electrocatalytic conversion of carbon dioxide to fuels. *Nat. Energy* **2019**, *4*, 732–745.

(17) Ismail-Beigi, S.; Arias, T. A. New algebraic formulation of density functional calculation. *Comput. Phys. Commun.* **2000**, *128*, 1–45.

(18) Sundararaman, R.; Arias, T. A. Efficient classical density-functional theories of rigid-molecular fluids and a simplified free energy functional for liquid water. *Comput. Phys. Commun.* **2014**, *185*, 818–825.

(19) Sundararaman, R.; Letchworth-Weaver, K.; Schwarz, K. A.; Gunceler, D.; Ozhabes, Y.; Arias, T. A. JDFTx: Software for joint density-functional theory. *SoftwareX* **2017**, *6*, 278–284.

(20) Abidi, N.; Lim, K. R. G.; Seh, Z. W.; Steinmann, S. N. Atomistic modeling of electrocatalysis: Are we there yet? *WIREs Comput Mol Sci.* **2021**, *11*, e1499.

(21) López, N.; Almora-Barrios, N.; Carchini, G.; Błoński, P.; Bellarosa, L.; García-Muelas, R.; Novell-Leruth, G.; García-Mota, M. State-of-the-art and challenges in theoretical simulations of heterogeneous catalysis at the microscopic level. *Catal. Sci. Technol.* **2012**, *2*, 2405–2417.

(22) Bellarosa, L.; García-Muelas, R.; Revilla-López, G.; López, N. Diversity at the water-metal interface: Metal, water thickness, and confinement effects. *ACS Cent. Sci.* **2016**, *2*, 109–116.

(23) Garcia-Ratés, M.; García-Muelas, R.; López, N. Solvation effects on methanol decomposition on Pd(111), Pt(111), and Ru(0001). *J. Phys. Chem. C* **2017**, *121*, 13803–13809.

(24) Sundararaman, R.; Schwarz, K. Evaluating continuum solvation models for the electrode-electrolyte interface: Challenges and strategies for improvement. *J. Chem. Phys.* **2017**, *146*, 084111.

(25) Rendón-Calle, A.; Builes, S.; Calle-Vallejo, F. Substantial improvement of electrocatalytic predictions by systematic assessment of solvent effects on adsorption energies. *Appl. Catal. B* **2020**, *276*, 119147.

(26) Ringe, S.; Hörmann, N. G.; Oberhofer, H.; Reuter, K. Implicit solvation methods for catalysis at electrified interfaces. *Chem. Rev.* **2021**, DOI: 10.1021/acs.chemrev.1c00675.

(27) Pérez-Ramírez, J.; López, N. Strategies to break linear scaling relationships. *Nat. Catal.* **2019**, *2*, 971–976.

(28) Pablo-García, S.; García-Muelas, R.; Sabadell-Rendón, A.; López, N. Dimensionality reduction of complex reaction networks in heterogeneous catalysis: From linear-scaling relationships to statistical learning techniques. *WIREs Comput Mol Sci.* **2021**, e1540.

(29) Teeter, T. E.; Van Rysselberghe, P. Reduction of carbon dioxide on mercury cathodes. *J. Chem. Phys.* **1954**, *22*, 759–760.

(30) Hori, Y.; Kikuchi, K.; Murata, A.; Suzuki, S. Production of methane and ethylene in electrochemical reduction of carbon dioxide at copper electrode in aqueous hydrogencarbonate solution. *Chem. Lett.* **1986**, *15*, 897–898.

(31) Hori, Y.; Murata, A.; Takahashi, R. Formation of hydrocarbons in the electrochemical reduction of carbon dioxide at a copper electrode in aqueous solution. *J. Chem. Soc., Faraday Trans. 1* **1989**, *85*, 2309–2326.

(32) Murata, A.; Hori, Y. Product selectivity affected by cationic species in electrochemical reduction of CO_2 and CO at a Cu electrode. *Bul. Chem. Soc. Jpn.* **1991**, *64*, 123–127.

(33) Hori, Y.; Murata, A.; Yoshinami, Y. Adsorption of CO, intermediately formed in electrochemical reduction of CO_2, at a copper electrode. *J. Chem. Soc. Faraday Trans.* **1991**, *87*, 125–128.

(34) Hori, Y.; Koga, O.; Yamazaki, H.; Matsuo, T. Infrared spectroscopy of adsorbed CO and intermediate species in electrochemical reduction of CO_2 to hydrocarbons on a Cu electrode. *Electrochim. Acta* **1995**, *40*, 2617–2622.

(35) Hori, Y.; Takahashi, I.; Koga, O.; Hoshi, N. Selective formation of C_2 compounds from electrochemical reduction of CO_2 at a series of copper single crystal electrodes. *J. Phys. Chem. B* **2002**, *106*, 15–17.

(36) Hori, Y.; Takahashi, I.; Koga, O.; Hoshi, N. Electrochemical reduction of carbon dioxide at various series of copper single crystal electrodes. *J. Mol. Catal. Chem.* **2003**, *199*, 39–47.

(37) Hori, Y.; Takahashi, R.; Yoshinami, Y.; Murata, A. Electrochemical reduction of CO at a copper electrode. *J. Phys. Chem. B* **1997**, *101*, 7075–7081.

(38) Hori, Y.; Konishi, H.; Futamura, T.; Murata, A.; Koga, O.; Sakurai, H.; Oguma, K. "Deactivation of copper electrode" in electrochemical reduction of CO_2. *Electrochim. Acta* **2005**, *50*, 5354–5369.

(39) Bagger, A.; Ju, W.; Varela, A. S.; Strasser, P.; Rossmeisl, J. Electrochemical CO_2 reduction: Classifying Cu facets. *ACS Catal.* **2019**, *9*, 7894–7899.

(40) Anderson, A. B.; Ray, N. K. Structures and reactions of H_3O^+, H_2O, and OH on an Fe electrode. Potential dependence. *J. Phys. Chem.* **1982**, *86*, 488–494.

(41) Dubouis, N.; Grimaud, A. The hydrogen evolution reaction: From material to interfacial descriptors. *Chem. Sci.* **2019**, *10*, 9165.

(42) Monteiro, M. C. O.; Dattila, F.; López, N.; Koper, M. T. The role of cation acidity on the competition between hydrogen evolution and CO_2 reduction on gold electrodes. *J. Am. Chem. Soc.* **2022**, *144*, 1589–1602.

(43) Anderson, A. B.; Kang, D. B. Quantum chemical approach to redox reactions including potential dependence: Application to a model for hydrogen evolution from diamond. *J. Phys. Chem. A* **1998**, *102*, 5993–5996.

(44) Chen, L. D.; Urushihara, M.; Chan, K.; Nørskov, J. K. Electric field effects in electrochemical CO_2 reduction. *ACS Catal.* **2016**, *6*, 7133–7139.

(45) Monteiro, M. C. O.; Dattila, F.; Hagedoorn, B.; García-Muelas, R.; López, N.;

Koper, M. T. M. Absence of CO_2 electroreduction on copper, gold and silver electrodes without metal cations in solution. *Nat. Catal.* **2021**, *4*, 654–662.

(46) Anderson, A. B.; Albu, T. V. Ab initio determination of reversible potentials and activation energies for outer-sphere oxygen reduction to water and the reverse oxidation reaction. *J. Am. Chem. Soc.* **1999**, *121*, 11855–11863.

(47) Anderson, A. B.; Albu, T. V. Catalytic effect of platinum on oxygen reduction An Ab Initio model including electrode potential dependence. *J. Electrochem. Soc.* **2000**, *147*, 4229–4238.

(48) Roques, J.; Anderson, A. B. Theory for the potential shift for OH_{ads} formation on the Pt-skin on $Pt_3Cr(111)$ in acid. *J. Electrochem. Soc.* **2004**, *151*, E85–E91.

(49) Roques, J.; Anderson, A. B. Electrode potential-dependent stages in OH_{ads} formation on the Pt_3Cr alloy (111) surface. *J. Electrochem. Soc.* **2004**, *11*, E340–E347.

(50) Tomasi, J.; Mennucci, B.; Cammi, R. Quantum mechanical continuum solvation models. *Chem. Rev.* **2005**, *105*, 2999–3093.

(51) Mathew, K.; Sundararaman, R.; Letchworth-Weaver, K.; Arias, T. A.; Hennig, R. G. Implicit solvation model for density-functional study of nanocrystal surfaces and reaction pathways. *J. Chem. Phys.* **2014**, *140*, 084106.

(52) Garcia-Ratés, M.; López, N. Multigrid-based methodology for implicit solvation models in periodic DFT. *J. Chem. Theory Comput.* **2016**, *12*, 1331–1341.

(53) Karlberg, G. S.; Jaramillo, T. F.; Skúlason, E.; Rossmeisl, J.; Bligaard, T.; Nørskov, J. K. Cyclic voltammograms for H on Pt(111) and Pt(100) from first principles. *Phys. Rev. Lett.* **2007**, *99*, 126101.

(54) Zhou, Y.; López, N. The role of Fe species on NiOOH in oxygen evolution reactions. *ACS Catal.* **2020**, *10*, 6254–6261.

(55) Nørskov, J. K.; Bligaard, T.; Rossmeisl, J.; Christensen, C. H. Towards the computational design of solid catalysts. *Nat. Chem.* **2009**, *1*, 37–46.

(56) Abidi, N.; Steinmann, S. N. How are transition states modelled in heterogeneous electrocatalysis? *Curr. Opin. Electrochem.* **2022**, *33*, 100940.

(57) Hansen, M. H.; Rossmeisl, J. pH in grand canonical statistics of an electrochemical interface. *J. Phys. Chem. C* **2016**, *120*, 29135–29143.

(58) Rossmeisl, J.; Chan, K.; Ahmed, R.; Tripković, V.; Björketun, M. E. pH in atomic scale simulations of electrochemical interfaces. *Phys. Chem. Chem. Phys.* **2013**, *15*, 10321–10325.

(59) Hansen, M. H.; Nilsson, A.; Rossmeisl, J. Modelling pH and potential in dynamic structures of the water/Pt(111) interface on the atomic scale. *Phys. Chem. Chem. Phys.* **2017**, *19*, 23505–23514.

(60) Kohn, W.; Lau, K.-H. Adatom dipole moments on metals and their interactions. *Solid State Commun.* **1976**, *18*, 553–555.

(61) Taylor, C. D.; Wasileski, S. A.; Filhol, J.-S.; Neurock, M. First principles reaction modeling of the electrochemical interface: Consideration and calculation of a tunable surface potential from atomic and electronic structure. *Phys. Rev. B* **2006**, *73*, 165402.

(62) Steinmann, S. N.; Michel, C.; Schwiedernoch, R.; Sautet, P. Impacts of electrode potentials and solvents on the electroreduction of CO_2: A comparison of theoretical approaches. *Phys. Chem. Chem. Phys.* **2015**, *17*, 13949–13963.

(63) Phan, T. H.; Banjac, K.; Cometto, F. P.; Dattila, F.; García-Muelas, R.; Raaijman, S. J.; Ye, C.; Koper, M. T. M.; López, N.; Lingenfelder, M. Emergence of potential-controlled Cu-nanocuboids and graphene-covered Cu-nanocuboids under operando CO_2 electroreduction. *Nano Lett.* **2021**, *21*, 2059–2065.

(64) Kohn, W.; Sham, L. J. Self-consistent equations including exchange and correlation effects. *Phys. Rev.* **1965**, *140*, A1133.

(65) Goodpaster, J. D.; Bell, A. T.; Head-Gordon, M. Identification of possible pathways for C–C bond formation during electrochemical reduction of CO_2: New theoretical insights from an improved electrochemical model. *J. Phys. Chem. Lett.* **2016**, *7*, 1471–1477.

(66) Pillai, H. S.; Xin, H. New Insights into electrochemical ammonia oxidation on Pt(100) from first principles. *Ind. Eng. Chem. Res.* **2019**, *58*, 10819–10828.

(67) Brönsted, J. N. Acid and basic catalysis. *Chem. Rev.* **1932**, *10*, 213–227.

(68) Evans, M.; Polanyi, M. Inertia and driving force of chemical reaction. *Trans. Faraday Soc.* **1938**, *34*, 11–24.

(69) Hammer, B. Bond activation at monatomic steps: NO dissociation at corrugated ru(0001). *Phys. Rev. Lett.* **1999**, *83*, 3681–3684.

(70) Liu, Z. P.; Hu, P. General rules for predicting where a catalytic reaction should occur on metal surfaces: A density functional theory study of C-H and C-O bond breaking/making on flat, stepped, and kinked metal surfaces. *J. Am. Chem. Soc.* **2003**, *125*, 1958–1967.

(71) Logadottir, A.; Rod, T. H.; Nørskov, J. K.; Hammer, B.; Dahl, S.; Jacobsen, C. J. H. The Brønsted-Evans-Polanyi relation and the volcano plot for ammonia synthesis over transition metal catalysts. *J. Catal.* **2001**, *197*, 229–231.

(72) Bligaard, T.; Nørskov, J. K.; Dahl, S.; Matthiesen, J.; Christensen, C. H.; Sehested, J. The Brønsted-Evans-Polanyi relation and the volcano curve in heterogeneous catalysis. *J. Catal.* **2004**, *224*, 206–217.

(73) Wang, S. et al. Universal transition state scaling relations for (de)hydrogenation over transition metals. *Phys. Chem. Chem. Phys.* **2011**, *13*, 20760–20765.

(74) Hammer, B.; Nørskov, J. K. Electronic factors determining the reactivity of metal surfaces. *Surf. Sci.* **1995**, *343*, 211–220.

(75) Hammer, B.; Morikawa, Y.; Nørskov, J. K. CO chemisorption at metal surfaces and overlayers. *Phys. Rev. Lett.* **1996**, *76*, 2141.

(76) Rossmeisl, J.; Logadottir, A.; Nørskov, J. K. Electrolysis of water on (oxidized) metal surfaces. *Chem. Phys.* **2005**, *319*, 178–184.

(77) Rossmeisl, J.; Qu, Z.-W.; Zhu, H.; Kroes, G.-J.; Nørskov, J. K. Electrolysis of water on oxide surfaces. *J. Electroanal. Chem.* **2007**, *607*, 83–89.

(78) Greeley, J.; Rossmeisl, J.; Hellman, A.; Nørskov, J. K. Theoretical trends in particle size effects for the oxygen reduction reaction. *Z. Phys. Chem.* **2007**, *221*, 1209–1220.

(79) Koper, M. T. M. Thermodynamic theory of multi-electron transfer reactions: Implications for electrocatalysis. *J. Electroanal. Chem.* **2011**, *660*, 254–260.

(80) Man, I. C.; Su, H.-Y.; Calle-Vallejo, F.; Hansen, H. A.; Martínez, J. I.; Inoglu, N. G.; Kitchin, J.; Jaramillo, T. F.; Nørskov, J. K.; Rossmeisl, J. Universality in oxygen evolution electrocatalysis on oxide surfaces. *ChemCatChem* **2011**, *3*, 1159–1165.

(81) Trasatti, S. Work function, electronegativity, and electrochemical behaviour of metals: III. Electrolytic hydrogen evolution in acid solutions. *J. Electroanal. Chem. Interfacial Electrochem.* **1972**, *39*, 163–184.

(82) Nørskov, J. K.; Bligaard, T.; Logadottir, A.; Kitchin, J. R.; Chen, J. G.; Pandelov, S.; Stimming, U. Trends in the exchange current for hydrogen evolution. *J. Electrochem. Soc.* **2005**, *152*, J23–J26.

(83) Calle-Vallejo, F.; Martínez, J. I.; García-Lastra, J. M.; Sautet, P.; Loffreda, D. Fast prediction of adsorption properties for platinum nanocatalysts with generalized coordination numbers. *Angew. Chem. Int. Ed.* **2014**, *53*, 8316–8319.

(84) Calle-Vallejo, F.; Tymoczko, J.; Colic, V.; Vu, Q. H.; Pohl, M. D.; Morgenstern, K.; Loffreda, D.; Sautet, P.; Schuhmann, W.; Bandarenka, A. S. Finding optimal surface sites on heterogeneous catalysts by counting nearest neighbors. *Science* **2015**, *350*, 185–189.

(85) Calle-Vallejo, F.; Loffreda, D.; Koper, M. T. M.; Sautet, P. Introducing structural sensitivity into adsorption–energy scaling relations by means of coordination numbers. *Nat. Chem.* **2015**, *7*, 403–410.

(86) Núñez, M.; Lansford, J. L.; Vlachos, D. G. Optimization of the facet structure of transition-metal catalysts applied to the oxygen reduction reaction. *Nat. Chem.* **2019**, *11*, 449–456.

(87) Zhu, C. et al. Product-specific active site motifs of Cu for electrochemical CO_2 reduction. *Chem* **2020**, *7*, 1–15.

(88) Mavrikakis, M.; Hammer, B.; Nørskov, J. K. Effect of strain on the reactivity of metal surfaces. **1998**, *81*, 2819–2822.

(89) Xu, Y.; Mavrikakis, M. Adsorption and dissociation of O_2 on gold surfaces: Effect of steps and strain. *J. Phys. Chem. B* **2003**, *107*, 9298–9307.

(90) García-Muelas, R.; López, N. Statistical learning goes beyond the *d*-band model providing the thermochemistry of adsorbates on transition metals. *Nat. Commun.* **2019**, *10*, 4687.

(91) Lide, D. R. Handbook of Chemistry and Physics, 84^{th} edition. 2003.

(92) García-Muelas, R. DFT datasets associated with "Statistical learning goes beyond the *d*-band model providing the thermochemistry of adsorbates on transition metals". `https://doi.org/10.19061/iochem-bd-1-43`, 2020; Online; accessed 29 July 2021.

(93) Bagger, A.; Ju, W.; Varela, A. S.; Strasser, P.; Rossmeisl, J. Single site porphyrine-like structures advantages over metals for selective electrochemical CO_2 reduction. *Catal. Today* **2017**, *288*, 74–78.

(94) Ting, L. R. L. et al. Electrochemical reduction of carbon dioxide to 1-Butanol on oxide-derived copper. *Angew. Chem. Int. Ed.* **2020**, *59*, 21072–21079.

(95) Zhi, X.; Vasileff, A.; Zheng, Y.; Jiao, Y.; Qiao, S.-Z. Role of oxygen-bound reaction intermediates in selective electrochemical CO_2 reduction. *Energy Environ. Sci.* **2021**, *14*, 3912–3930.

(96) Calvinho, K. U. D.; Alherz, A. W.; Yap, K. M. K.; Laursen, A. B.; Hwang, S.; Bare, Z. J. L.; Clifford, Z.; Musgrave, C. B.; Dismukes, G. C. Surface hydrides on Fe_2P electrocatalyst reduce CO_2 at low overpotential: Steering selectivity to ethylene glycol. *J. Am. Chem. Soc.* **2021**, *143*, 21275–21285.

(97) Yeo, B. S.; Zhou, Y.; Martín, A.; Dattila, F.; Xi, S.; López, N.; Pérez-Ramírez, J. Fischer-Tropsch synthesis using carbon dioxide, water and electricity. *PREPRINT (Version 1) available at Research Square* **2021**, DOI: 10.21203/rs.3.rs–418062/v1.

(98) Exner, K. S. Does a thermoneutral electrocatalyst correspond to the apex of a volcano plot for a simple two-electron process? *Angew. Chem. Int. Ed.* **2020**, *59*, 10236–10240.

(99) Lindgren, P.; Kastlunger, G.; Peterson, A. A. A Challenge to the $G \sim 0$ interpretation of hydrogen evolution. *ACS Catal.* **2020**, *10*, 121–128.

(100) Huang, J.; Hörmann, N.; Oveisi, E.; Loiudice, A.; De Gregorio, G. L.; Andreussi, O.;

Marzari, N.; Buonsanti, R. Potential-induced nanoclustering of metallic catalysts during electrochemical CO_2 reduction. *Nat. Commun.* **2018**, *9*, 3117.

(101) Gao, D.; Arán-Ais, R. M.; Jeon, H. S.; Roldan-Cuenya, B. Rational catalyst and electrolyte design for CO_2 electroreduction towards multicarbon products. *Nat. Catal.* **2019**, *2*, 198–210.

(102) Kim, Y. G.; Baricuatro, J. H.; Javier, A.; Gregoire, J. M.; Soriaga, M. P. The evolution of the polycrystalline copper surface, first to Cu(111) and then to Cu(100), at a fixed CO_2RR potential: A study by operando EC-STM. *Langmuir* **2014**, *30*, 15053–15056.

(103) Kim, Y.-G.; Baricuatro, J. H.; Soriaga, M. P. Surface reconstruction of polycrystalline Cu electrodes in aqueous $KHCO_3$ electrolyte at potentials in the early stages of CO_2 reduction. *Electrocatalysis* **2018**, *9*, 526–530.

(104) Kim, D.; Resasco, J.; Yu, Y.; Asiri, A. M.; Yang, P. Synergistic geometric and electronic effects for electrochemical reduction of carbon dioxide using gold-copper bimetallic nanoparticles. *Nat. Commun.* **2014**, *5*, 4948.

(105) Kim, Y.-G. G.; Javier, A.; Baricuatro, J. H.; Torelli, D.; Cummins, K. D.; Tsang, C. F.; Hemminger, J. C.; Soriaga, M. P. Surface reconstruction of pure-Cu single-crystal electrodes under CO-reduction potentials in alkaline solutions: A study by seriatim ECSTM-DEMS. *J. Electroanal.* **2016**, *780*, 290–295.

(106) Kuhl, K. P.; Cave, E. R.; Abram, D. N.; Jaramillo, T. F. New insights into the electrochemical reduction of carbon dioxide on metallic copper surfaces. *Energy Environ. Sci.* **2012**, *5*, 7050–7059.

(107) Chou, T.-C. et al. Controlling the oxidation state of Cu electrode and reaction intermediates for electrochemical CO_2 reduction to ethylene. *J. Am. Chem. Soc.* **2020**, *142*, 2857–2867.

(108) Li, C. W.; Kanan, M. W. CO_2 reduction at low overpotential on Cu electrodes resulting from the reduction of thick Cu_2O films. *J. Am. Chem. Soc.* **2012**, *134*, 7231–7234.

(109) Li, C. W.; Ciston, J.; Kanan, M. W. Electroreduction of carbon monoxide to liquid fuel on oxide-derived nanocrystalline copper. *Nature* **2014**, *508*, 504–507.

(110) Ren, D.; Deng, Y.; Handoko, A. D.; Chen, C. S.; Malkhandi, S.; Yeo, B. S. Selective electrochemical reduction of carbon dioxide to ethylene and ethanol on copper(I) oxide catalysts. *ACS Catal.* **2015**, *5*, 2814–2821.

(111) Kim, D.; Lee, S.; Ocon, J. D.; Jeong, B.; Lee, J. K.; Lee, J. Insights into an autonomously formed oxygen-evacuated Cu_2O electrode for the selective production of C_2H_4 from CO_2. *Phys. Chem. Chem. Phys.* **2015**, *17*, 824–830.

(112) Mistry, H. et al. Highly selective plasma-activated copper catalysts for carbon dioxide reduction to ethylene. *Nat. Commun.* **2016**, *7*, 12123.

(113) Handoko, A. D.; Ong, C. W.; Huang, Y.; Lee, Z. G.; Lin, L.; Panetti, G. B.; Yeo, B. S. Mechanistic insights into the selective electroreduction of carbon dioxide to ethylene on Cu_2O-derived copper catalysts. *J. Phys. Chem. C* **2016**, *120*, 20058–20067.

(114) De Luna, P.; Quintero-Bermudez, R.; Dinh, C.-T.; Ross, M. B.; Bushuyev, O. S.; Todorović, P.; Regier, T.; Kelley, S. O.; Yang, P.; Sargent, E. H. Catalyst electroredeposition controls morphology and oxidation state for selective carbon dioxide reduction. *Nat. Catal.* **2018**, *1*, 103–110.

(115) Li, J. et al. Copper adparticle enabled selective electrosynthesis of *n*-propanol. *Nat. Commun.* **2018**, *9*, 4614.

(116) Dutta, A.; Rahaman, M.; Luedi, N. C.; Mohos, M.; Broekmann, P. Morphology matters: tuning the product distribution of CO_2 electroreduction on oxide-derived Cu foam catalysts. *ACS Catal.* **2016**, *6*, 3804–3814.

(117) Reske, R.; Mistry, H.; Behafarid, F.; Roldan Cuenya, B.; Strasser, P. Particle size effects in the catalytic electroreduction of CO_2 on Cu nanoparticles. *J. Am. Chem. Soc.* **2014**, *136*, 6978–6986.

(118) Loiudice, A.; Lobaccaro, P.; Kamali, E. A.; Thao, T.; Huang, B. H.; Ager, J. W.; Buonsanti, R. Tailoring copper nanocrystals towards C_2 products in electrochemical CO_2 reduction. *Angew. Chem. Int. Ed.* **2016**, *55*, 5789–5792.

(119) Lum, Y.; Ager, J. W. Stability of residual oxides in oxide-derived copper catalysts for electrochemical CO_2 reduction investigated with ^{18}O labeling. *Angew. Chem. Int. Ed.* **2018**, *57*, 551–554.

(120) Zhu, Q.; Sun, X.; Yang, D.; Ma, J.; Kang, X.; Zheng, L.; Zhang, J.; Wu, Z.; Han, B. Carbon dioxide electroreduction to C_2 products over copper-cuprous oxide derived from electrosynthesized copper complex. *Nat. Commun.* **2019**, *10*, 3851.

(121) Velasco-Vélez, J.-J. et al. The role of the copper oxidation state in the electrocatalytic reduction of CO_2 into valuable hydrocarbons. *ACS Sustain. Chem. Eng.* **2019**, *7*, 1485–1492.

(122) Lum, Y.; Ager, J. W. Evidence for product-specific active sites on oxide-derived Cu catalysts for electrochemical CO_2 reduction. *Nat. Catal.* **2019**, *2*, 86–93.

(123) Zheng, Y.; Vasileff, A.; Zhou, X.; Jiao, Y.; Jaroniec, M.; Qiao, S.-Z. Understanding the roadmap for electrochemical reduction of CO_2 to multi-carbon oxygenates and hydrocarbons on copper-based catalysts. *J. Am. Chem. Soc.* **2019**, *141*, 7646–7659.

(124) Hasa, B.; Jouny, M.; Ko, B. H.; Xu, B.; Jiao, F. Flow electrolyzer mass spectrometry with a gasdiffusion electrode design. *Angew. Chem. Int. Ed.* **2021**, *60*, 3277–3282.

(125) Lum, Y.; Cheng, T.; Goddard III, W. A.; Ager, J. W. Electrochemical CO reduction

builds solvent water into oxygenate products. *J. Am. Chem. Soc.* **2018**, *140*, 9337–9340.

(126) Wang, H.-Y.; Soldemo, M.; Degerman, D.; Lömker, P.; Schlueter, C.; Nilsson, A.; Amann, P. Direct evidence of subsurface oxygen formation in oxide-derived Cu by X-ray photoelectron spectroscopy. *Angew. Chem. Int. Ed.* **2022**, *61*, e202111021.

(127) Tang, Z.; Nishiwaki, E.; Fritz, K. E.; Hanrath, T.; Suntivich, J. Cu(I) reducibility controls ethylene vs ethanol selectivity on (100)-textured copper during pulsed CO_2 reduction. *ACS Appl. Mater. Interfaces* **2021**, *13*, 14050–14055.

(128) DiDomenico, R. C.; Hanrath, T. Pulse symmetry impacts the C_2 product selectivity in pulsed electrochemical CO_2 reduction. *ACS Energy Lett.* **2022**, *7*, 292–299.

(129) Liu, G.; Lee, M.; Kwon, S.; Zeng, G.; Eichhorn, J.; Buckley, A. K.; Toste, F. D.; Goddard III, W. A.; Toma, F. M. CO_2 reduction on pure Cu produces only H_2 after subsurface O is depleted: Theory and experiment. *Proc. Natl. Acad. Sci. U.S.A.* **2021**, *118*, e2012649118.

(130) Scholten, F.; Nguyen, K.-L. C.; Bruce, J. P.; Heyde, M.; Roldan Cuenya, B. Identifying structure-selectivity correlations in the electrochemical reduction of CO_2: comparison of well-ordered atomically-clean and chemically-etched Cu single crystal surfaces. *Angew. Chem. Int. Ed.* **2021**, *60*, 19169–19175.

(131) Chan, K. A few basic concepts in electrochemical carbon dioxide reduction. *Nat. Commun.* **2020**, *11*, 5954.

(132) Corrigan, D. A.; Bendert, R. M. Effect of coprecipitated metal ions on the electrochemistry of nickel hydroxide thin films: Cyclic voltammetry in 1 M KOH. *J. Electrochem. Soc.* **1989**, *136*, 723.

(133) Doyle, R. L.; Godwin, I. J.; Brandon, M. P.; Lyons, M. E. Redox and electrochemical water splitting catalytic properties of hydrated metal oxide modified electrodes. *Phys. Chem. Chem. Phys.* **2013**, *15*, 13737.

(134) Gong, M.; Li, Y.; Wang, H.; Liang, Y.; Wu, J. Z.; Zhou, J.; Wang, J.; Regier, T.; Wei, F.; Dai, H. An advanced NiFe layered double hydroxide electrocatalyst for water oxidation. *J. Am. Chem. Soc.* **2013**, *135*, 8452–8455.

(135) Diaz-Morales, O.; Ferrus-Suspedra, D.; Koper, M. T. M. The importance of nickel oxyhydroxide deprotonation on its activity towards electrochemical water oxidation. *Chem. Sci.* **2016**, *7*, 2639.

(136) Trotochaud, L.; Young, S. L.; Ranney, J. K.; Boettcher, S. W. Nickel-Iron oxyhydroxide oxygen-evolution electrocatalysts: The role of intentional and incidental iron incorporation. *J. Am. Chem. Soc.* **2014**, *136*, 6744–6753.

(137) Govind Rajan, A.; Carter, E. A. Microkinetic model for pH- and potential-dependent oxygen evolution during water splitting on Fe-doped β-NiOOH. *Energy Environ. Sci.* **2020**, *13*, 4962–4976.

(138) Lee, S.; Bai, L.; Hu, X. Deciphering iron-dependent activity in oxygen evolution catalyzed by nickeliron layered double hydroxide. *Angew. Chem. Int. Ed.* **2020**, *59*, 8072–8077.

(139) Bediako, D. K.; Lassalle-Kaiser, B.; Surendranath, Y.; Yano, J.; Yachandra, V. K.; Nocera, D. G. Structure-activity correlations in a nickel-borate oxygen evolution catalyst. *J. Am. Chem. Soc.* **2012**, *134*, 6801–6809.

(140) Schouten, K. J. P.; Kwon, Y.; van der Ham, C. J. M.; Qin, Z.; Koper, M. T. A new mechanism for the selectivity to C_1 and C_2 species in the electrochemical reduction of carbon dioxide on copper electrodes. *Chem. Sci.* **2011**, *2*, 1902–1909.

(141) Schouten, K. J. P.; Gallent, E. P.; Koper, M. T. M. The influence of pH on the reduction of CO and CO_2 to hydrocarbons on copper electrodes. *J. Electroanal. Chem.* **2014**, *716*, 53–57.

(142) Bertheussen, E. et al. Acetaldehyde as an Intermediate in the Electroreduction of Carbon Monoxide to Ethanol on Oxide-Derived Copper. *Angew. Chem. Int. Ed.* **2016**, *55*, 1450–1454.

(143) Kortlever, R.; Shen, J.; Schouten, K. J. P.; Calle-Vallejo, F.; Koper, M. T. M. Catalysts and reaction pathways for the electrochemical reduction of carbon dioxide. *J. Phys. Chem. Lett.* **2015**, *6*, 4073–4082.

(144) Garza, A. J.; Bell, A. T.; Head-Gordon, M. Mechanism of CO_2 reduction at copper surfaces: Pathways to C_2 products. *ACS Catal.* **2018**, *8*, 1490–1499.

(145) Zhu, S.; Li, T.; Cai, W. B.; Shao, M. CO_2 electrochemical reduction as probed through infrared spectroscopy. *ACS Energy Lett.* **2019**, *4*, 682–689.

(146) Handoko, A. D.; Wei, F.; Jenndy,; Yeo, B. S.; Seh, Z. W. Understanding heterogeneous electrocatalytic carbon dioxide reduction through operando techniques. *Nat. Catal.* **2018**, *1*, 922–934.

(147) Pérez-Gallent, E.; Figueiredo, M. C.; Calle-Vallejo, F.; Koper, M. T. M. Spectroscopic observation of a hydrogenated CO dimer intermediate during CO reduction on Cu(100) electrodes. *Angew. Chem. Int. Ed.* **2017**, *56*, 3621–3624.

(148) Mul, G.; Moradzaman, M. In situ Raman study of potential dependent surface adsorbed carbonate, CO, OH and C-species on Cu-electrodes during electrochemical reduction of CO_2. *ChemElectroChem* **2021**, *8*, 1478–1485.

(149) Kim, Y.; Park, S.; Shin, S.-J.; Choi, W.; Min, B. K.; Kim, H.; Kim, W.; Hwang, Y. J.

Time-resolved observation of C-C coupling intermediates on Cu electrodes for selective electrochemical CO_2 reduction. *Energy & Environ. Sci.* **2020**, *13*, 4301.

(150) Jiang, S.; Klingan, K.; Pasquini, C.; Dau, H. New aspects of operando Raman spectroscopy applied to electrochemical CO_2 reduction on Cu foams. *J. Chem. Phys.* **2019**, *150*, 041718.

(151) Gunathunge, C. M.; Ovalle, V. J.; Li, Y.; Janik, M. J.; Waegele, M. M. Existence of an electrochemically inert CO population on Cu electrodes in alkaline pH. *ACS Catal.* **2018**, *8*, 7507–7516.

(152) An, H.; Wu, L.; Mandemaker, L. D. B.; de Ruiter, J.; Wijten, J. H.; Janssens, J.; van der Stam, W.; Weckhuysen, B. M. Sub-second time-resolved Surface Enhanced Raman spectroscopy reveals dynamic CO intermediates during electrochemical CO_2 reduction on copper. *Angew. Chem. Int. Ed.* **2021**, *60*, 16576–16584.

(153) Zhan, C.; Dattila, F.; Rettenmaier, C.; Bergmann, A.; Kühl, S.; García-Muelas, R.; López, N.; Roldan Cuenya, B. Revealing the CO coverage-driven C−C coupling mechanism for electrochemical CO_2 reduction on Cu_2O nanocubes *via Operando* Raman spectroscopy. *ACS Catal.* **2021**, *11*, 7694–7701.

(154) Herzog, A.; Bergmann, A.; Jeon, H. S.; Timoshenko, J.; Kühl, S.; Rettenmaier, C.; Luna Lopez, M.; Haase, F. T.; Roldan Cuenya, B. Operando investigation of Ag-decorated Cu_2O nanocube catalysts with enhanced CO_2 electroreduction toward liquid products. *Angew. Chem. Int. Ed.* **2021**, *60*, 7426–7435.

(155) Iyengar, P.; Kolb, M. J.; Pankhurst, J. R.; Calle-vallejo, F.; Buonsanti, R. Elucidating the facet-dependent selectivity for CO_2 electroreduction to ethanol of Cu-Ag tandem catalysts. *ACS Catal.* **2021**, *11*, 4456–4463.

(156) Raaijman, S. J.; Schellekens, M. P.; Corbett, P. J.; Koper, M. T. M. High-pressure

CO electroreduction at silver produces ethanol and propanol. *Angew. Chem. Int. Ed.* **2021**, *60*, 21732 –21736.

(157) Creative Commons Attribution 4.0 International License. `http://creativecommons.org/licenses/by/4.0/`, Online; accessed 5 August 2021.

(158) Kim, C.; Bui, J. C.; Luo, X.; Cooper, J. K.; Kusoglu, A.; Weber, A. Z.; Bell, A. T. Tailored catalyst microenvironments for CO_2 electroreduction to multicarbon products on copper using bilayer ionomer coatings. *Nat. Energy* **2021**, *6*, 1026–1034.

(159) Moore, T.; Xia, X.; Baker, S. E.; Duoss, E. B.; Beck, V. A. Elucidating mass transport regimes in gas diffusion electrodes for CO_2 electroreduction. *ACS Energy Lett.* **2021**, *6*, 3600–3606.

(160) Goyal, A.; Marcandalli, G.; Mints, V. A.; Koper, M. T. M. Competition between CO_2 reduction and hydrogen evolution on a gold electrode under well-defined mass transport conditions. *J. Am. Chem. Soc.* **2020**, *142*, 4154–4161.

(161) Goyal, A.; Koper, M. T. M. The interrelated effect of cations and electrolyte pH on the hydrogen evolution reaction on gold electrodes in alkaline media. *Angew. Chem. Int. Ed.* **2021**, *60*, 13452–13462.

(162) Vass, A.; Endrődi, B.; Samu, G. F.; Balog, A.; Kormányos, A.; Cherevko, S.; Janáky, C. Local chemical environment governs anode processes in CO_2 electrolyzers. *ACS Energy Lett.* **2021**, *6*, 3801–3808.

(163) Gupta, N.; Gattrell, M.; MacDougall, B. Calculation for the cathode surface concentrations in the electrochemical reduction of CO_2 in $KHCO_3$ solutions. *J. Appl. Electrochem.* **2006**, *36*, 161–172.

(164) Bohra, D.; Chaudhry, J. H.; Burdyny, T.; Pidko, E. A.; Smith, W. A. Modeling the

electrical double layer to understand the reaction environment in a CO_2 electrocatalytic system. *Energy Environ. Sci.* **2019**, *12*, 3380–3389.

(165) Wang, Y. et al. Catalyst synthesis under CO_2 electroreduction favours faceting and promotes renewable fuels electrosynthesis. *Nat. Catal.* **2019**, *3*, 98–106.

(166) Ringe, S.; Morales-Guio, C. G.; Chen, L. D.; Fields, M.; Jaramillo, T. F.; Hahn, C.; Chan, K. Double layer charging driven carbon dioxide adsorption limits the rate of electrochemical carbon dioxide reduction on Gold. *Nat. Commun.* **2020**, *11*, 33.

(167) Veenstra, F. L.; Ackerl, N.; Martín, A. J.; Pérez-Ramírez, J. Laser-microstructured copper reveals selectivity patterns in the electrocatalytic reduction of CO_2. *Chem* **2020**, *6*, 1707–1722.

(168) Jeon, H. S.; Timoshenko, J.; Rettenmaier, C.; Herzog, A.; Yoon, A.; Chee, S. W.; Oener, S.; Hejral, U.; Haase, F. T.; Roldan Cuenya, B. Selectivity control of Cu nanocrystals in a gas-fed flow cell through CO_2 pulsed electroreduction. *J. Am. Chem. Soc.* **2021**, *143*, 7578–7587.

(169) Cheng, T.; Xiao, H.; Goddard III, W. A. Reaction mechanisms for the electrochemical reduction of CO_2 to CO and formate on the Cu(100) surface at 298 K from quantum mechanics free energy calculations with explicit water. *J. Am. Chem. Soc.* **2016**, *138*, 13802–13805.

(170) Resasco, J.; Chen, L. D.; Clark, E.; Tsai, C.; Hahn, C.; Jaramillo, T. F.; Chan, K.; Bell, A. T. Promoter effects of alkali metal cations on the electrochemical reduction of carbon dioxide. *J. Am. Chem. Soc.* **2017**, *139*, 11277–11287.

(171) Ringe, S.; Clark, E. L.; Resasco, J.; Walton, A.; Seger, B.; Bell, A. T.; Chan, K. Understanding cation effects in electrochemical CO_2 reduction. *Energy Environ. Sci.* **2019**, *12*, 3001–3014.

(172) Singh, M. R.; Kwon, Y.; Lum, Y.; Ager III, J. W.; Bell, A. T. Hydrolysis of electrolyte cations enhances the electrochemical reduction of CO_2 over Ag and Cu. *J. Am. Chem. Soc.* **2016**, *138*, 13006–13012.

(173) Smith, B. D.; Irish, D. E.; Kedzierzawski, P.; Augustynski, J. A Surface Enhanced Raman scattering study of the intermediate and poisoning species formed during the electrochemical reduction of CO_2 on copper. *J. Electrochem. Soc.* **1997**, *144*, 4288–4296.

(174) Bagger, A.; Arnarson, L.; Hansen, M. H.; Spohr, E.; Rossmeisl, J. Electrochemical CO reduction: A property of the electrochemical interface. *J. Am. Chem. Soc.* **2019**, *141*, 1506–1514.

(175) Sebastián Pascual, P.; Petersen, A. S.; Bagger, A.; Rossmeisl, J.; Escudero-Escribano, M. pH and anion effects on Cu-phosphate interfaces for CO electroreduction. *ACS Catal.* **2021**, *11*, 1128–1135.

(176) Cofell, E. R.; Nwabara, U. O.; Bhargava, S. S.; Henckel, D. E.; Kenis, P. J. A. Investigation of electrolyte-dependent carbonate formation on gas diffusion electrodes for CO_2 electrolysis. *ACS Appl. Mater. Interfaces* **2021**, *13*, 15132–15142.

(177) Zhu, J. et al. Cation-deficiency-dependent CO_2 electroreduction over copper-based Ruddlesden-Popper perovskite oxides. *Angew. Chem. Int. Ed.* **2022**, *61*, e202111670.

(178) Raciti, D.; Livi, K. J.; Wang, C. Highly dense Cu nanowires for low-overpotential CO_2 reduction. *Nano Letters* **2015**, *15*, 6829–6835.

(179) Huang, J. E. et al. CO_2 electrolysis to multicarbon products in strong acid. *Science* **2021**, *372*, 1074–1078.

(180) Li, J.; Wu, D.; Malkani, A. S.; Chang, X.; Cheng, M.-J.; Xu, B.; Lu, Q. Hydroxide is

not a promoter of C_{2+} product formation in the electrochemical reduction of CO on copper. *Angew. Chem. Int. Ed.* **2020**, *59*, 4464–4469.

(181) Garcia, A. C.; Touzalin, T.; Nieuwland, C.; Perini, N.; Koper, M. T. M. Enhancement of oxygen evolution activity of nickel oxyhydroxide by electrolyte alkali cations. *Angew. Chem. Int. Ed.* **2019**, *58*, 12999–13003.

(182) Gao, Q.; Ranjan, C.; Pavlovic, Z.; Blume, R.; Schlögl, R. Enhancement of stability and activity of MnO_x/Au electrocatalysts for oxygen evolution through adequate electrolyte composition. *ACS Catal.* **2015**, *5*, 7265–7275.

(183) Vass, Á.; Kormányos, A.; Kószó, Z.; Endrdi, B.; Janáky, C. Anode catalysts in CO_2 electrolysis: Challenges and untapped opportunities. *ACS Catal.* **2022**, *12*, 1037–1051.

(184) Shingaya, Y.; Ito, M. Interconversion of a bisulfate anion into a sulfuric acid molecule on a Pt(111) electrode in a 0.5 M H_2SO_4 solution. *Chem. Phys. Lett.* **1996**, *256*, 438–444.

(185) Nart, F. C.; Iwasita, T.; Weber, M. Vibrational spectroscopy of adsorbed sulfate on Pt(111). *Electrochim. Acta* **1994**, *39*, 961–968.

(186) Shingaya, Y.; Ito, M. Simulation of the electric double layers on Pt(111). *Surf. Sci.* **1997**, *386*, 34–47.

(187) Faguy, P. W.; Marinković, N. S.; Adžić, R. R. Infrared spectroscopic analysis of anions adsorbed from bisulfate-containing solutions on Pt(111) electrodes. *J. Electroanal. Chem.* **1996**, *407*, 209–218.

(188) Marković, N. M.; Grgur, B. N.; Lucas, C. A.; Ross, P. N. Electrooxidation of CO and H_2/CO mixtures on Pt(111) in acid solutions. *J. Phys. Chem. B* **1999**, *103*, 487–495.

(189) García, N.; Climent, V.; Orts, J. M.; Feliu, J. M.; Aldaz, A. Effect of pH and alkaline

metal cations on the voltammetry of Pt(111) single crystal electrodes in sulfuric acid solution. *ChemPhysChem* **2004**, *5*, 1221–1227.

(190) Akbashev, A. R. Electrocatalysis goes nuts. *ACS Catal.* **2022**, *12*, 4296–4301.

(191) Koper, M. T. M. Structure sensitivity and nanoscale effects in electrocatalysis. *Nanoscale* **2011**, *3*, 2054–2073.

(192) Cao, L.; Raciti, D.; Li, C.; Livi, K. J. T.; Rottmann, P. F.; Hemker, K. J.; Mueller, T.; Wang, C. Mechanistic insights for low-overpotential electroreduction of CO_2 to CO on copper nanowires. *ACS Catal.* **2017**, *7*, 8578–8587.

(193) Mistry, H.; Reske, R.; Zeng, Z.; Zhao, Z.-J.; Greeley, J.; Strasser, P.; Cuenya, B. R. Exceptional size-dependent activity enhancement in the electroreduction of CO_2 over Au nanoparticles. *J. Am. Chem. Soc.* **2014**, *136*, 16473–16476.

(194) Feng, X.; Jiang, K.; Fan, S.; Kanan, M. W. A direct grain-boundary-activity correlation for CO electroreduction on Cu nanoparticles. *ACS Cent. Sci.* **2016**, *2*, 169–174.

(195) Mistry, H. et al. Enhanced carbon dioxide electroreduction to carbon monoxide over defect-rich plasma-activated silver catalysts. *Angew. Chem. Int. Ed.* **2017**, *56*, 11394–11398.

(196) Gao, D.; Zegkinoglou, I.; Divins, N. J.; Scholten, F.; Sinev, I.; Grosse, P.; Roldan Cuenya, B. Plasma-activated copper nanocube catalysts for efficient carbon dioxide electroreduction to hydrocarbons and alcohols. *ACS Nano* **2017**, *11*, 4825–4831.

(197) Zhang, B. et al. Highly electrocatalytic ethylene production from CO_2 on nanodefective Cu nanosheets. *J. Am. Chem. Soc.* **2020**, *142*, 13606–13613.

(198) Simon, G. H.; Kley, C. S.; Roldan Cuenya, B. Potential-dependent morphology of

copper catalysts during CO_2 electroreduction revealed by In Situ Atomic Force Microscopy. *Angew. Chem. Int. Ed.* **2021**, *60*, 2561–2568.

(199) Kas, R.; Yang, K.; Bohra, D.; Kortlever, R.; Burdyny, T.; Smith, W. Electrochemical CO_2 reduction on nanostructured metal electrodes: Fact or defect? *Chem. Sci.* **2020**, *11*, 1738–1749.

(200) Daelman, N.; Hegner, F. S.; Rellán-Piñeiro, M.; Capdevila-Cortada, M.; García-Muelas, R.; López, N. Quasi-degenerate states and their dynamics in oxygen deficient reducible metal oxides. *J. Chem. Phys.* **2020**, *152*, 050901.

(201) Marks, L. D.; Peng, L. Nanoparticle shape, thermodynamics and kinetics. *J. Phys. Condens. Matter* **2016**, *28*, 053001.

(202) Eilert, A. et al. Subsurface oxygen in oxide-derived copper electrocatalysts for carbon dioxide reduction. *J. Phys. Chem. Lett.* **2017**, *8*, 285–290.

(203) Cavalca, F.; Ferragut, R.; Aghion, S.; Eilert, A.; Diaz-Morales, O.; Liu, C.; Koh, A. L.; Hansen, T. W.; Pettersson, L. G. M.; Nilsson, A. Nature and distribution of stable subsurface oxygen in copper electrodes during electrochemical CO_2 reduction. *J. Phys. Chem. C* **2017**, *121*, 25003–25009.

(204) Singh, A. K.; Zhou, L.; Shinde, A.; Suram, S. K.; Montoya, J. H.; Winston, D.; Gregoire, J. M.; Persson, K. A. Electrochemical stability of metastable materials. *Chem. Mater.* **2017**, *29*, 10159–10167.

(205) Liu, C.; Lourenço, M. P.; Hedström, S.; Cavalca, F.; Diaz-Morales, O.; Duarte, H. A.; Nilsson, A.; Pettersson, L. G. Stability and effects of subsurface oxygen in oxide-derived Cu catalyst for CO_2 reduction. *J. Phys. Chem. C* **2017**, *121*, 25010–25017.

(206) Schedel-Niedrig, T.; Neisius, T.; Böttger, I.; Kitzelmann, E.; Weinberg, G.; De-

muth, D.; Schlögl, R. Copper (sub)oxide formation: A surface sensitive characterization of model catalysts. *Phys. Chem. Chem. Phys.* **2000**, *2*, 2407–2417.

(207) Zhang, Z.; Zandkarimi, B.; Alexandrova, A. N. Ensembles of metastable states govern heterogeneous catalysis on dynamic interfaces. *Acc. Chem. Res.* **2020**, *53*, 447–458.

(208) McCrum, I. T.; Bondue, C. J.; Koper, M. T. M. Hydrogen-induced step-edge roughening of platinum electrode surfaces. *J. Phys. Chem. Lett.* **2019**, *10*, 6842–6849.

(209) Yoon, J.; Cao, Z.; Raju, R. K.; Wang, Y.; Burnley, R.; Gellman, A. J.; Farimani, A. B.; Ulissi, Z. W. Deep reinforcement learning for predicting kinetic pathways to surface reconstruction in a ternary alloy. *Mach. Learn.: Sci. Technol.* **2021**, *2*, 045018.

(210) Dattila, F.; García-Muelas, R.; López, N. Active and selective ensembles in oxide-derived copper catalysts for CO_2 reduction. *ACS Energy Lett.* **2020**, *5*, 3176–3184.

(211) Cheng, D. et al. The nature of active sites for carbon dioxide electroreduction over oxide-derived copper catalysts. *Nat. Commun.* **2021**, *12*, 395.

(212) Korpelin, V.; Kiljunen, T.; Melander, M. M.; Caro, M. A.; Kristoffersen, H. H.; Mammen, N.; Apaja, V.; Honkala, K. Addressing dynamics at catalytic heterogeneous interfaces with DFT-MD: Anomalous temperature distributions from commonly used thermostats. *J. Phys. Chem. Lett.* **2022**, *13*, 2644–2652.

(213) Huang, Y.; Chen, Y.; Cheng, T.; Wang, L.-W.; Goddard III, W. A. Identification of the selective sites for electrochemical reduction of CO to C_{2+} products on copper nanoparticles by combining reactive force fields, density functional theory, and machine learning. *ACS Energy Lett.* **2018**, *3*, 2983–2988.

(214) Rieder, K. H.; Stocker, W. Hydrogen-induced subsurface reconstruction of Cu(110). *Phys. Rev. Lett.* **1986**, *57*, 2548–2551.

(215) Jensen, F.; Besenbacher, F.; Laegsgaard, E.; Stensgaard, I. Surface reconstruction of Cu(110) induced by oxygen chemisorption. *Phys. Rev. B* **1990**, *41*, 10233–10236.

(216) Chorkendorff, I.; Rasmussen, P. B. Reconstruction of Cu(100) by adsorption of atomic hydrogen. *Surf. Sci.* **1991**, *248*, 35–44.

(217) Jensen, F.; Besenbacher, F.; Stensgaard, I. Two new oxygen induced reconstructions on Cu(111). *Surf. Sci. Lett.* **1992**, *259*, L774–L780.

(218) Foss, M.; Besenbacher, F.; Klink, C.; Stensgaard, I. Deuterium-induced restructuring of Cu(100). *Chem. Phys. Lett.* **1993**, *215*, 535–540.

(219) Hellman, A.; Svensson, K.; Andersson, S. Hydrogen-induced reconstruction of Cu(100): Two-dimensional and one-dimensional structures of surface hydride. *J. Phys. Chem. C* **2014**, *118*, 15773–15778.

(220) Tian, J.; Cao, H.; Wu, W.; Yu, Q.; Guisinger, N. P.; Chen, Y. P. Graphene induced surface reconstruction of Cu. *Nano Lett.* **2012**, *12*, 3893–3899.

(221) Matsushima, H.; Taranovskyy, A.; Haak, C.; Gründer, Y.; Magnussen, O. M. Reconstruction of Cu(100) electrode surfaces during hydrogen evolution. *J. Am. Chem. Soc.* **2009**, *131*, 10362–10363.

(222) Matsushima, H.; Haak, C.; Taranovskyy, A.; Gründer, Y.; Magnussen, O. M. *In situ* video STM studies of the hydrogen-induced reconstruction of Cu(100): Potential and pH dependence. *Phys. Chem. Chem. Phys.* **2010**, *12*, 13992–13998.

(223) Kim, Y. G.; Soriaga, M. P. Cathodic regeneration of a clean and ordered Cu(100)-(1×1) surface from an air-oxidized and disordered electrode: An operando STM study. *J. Electroanal. Chem.* **2014**, *734*, 7–9.

(224) Gunathunge, C. M.; Li, X.; Li, J.; Hicks, R. P.; Ovalle, V. J.; Waegele, M. M. Spectroscopic observation of reversible surface reconstruction of copper electrodes under CO_2 reduction. *J. Phys. Chem. C* **2017**, *121*, 12337–12344.

(225) Akhade, S. A.; McCrum, I. T.; Janik, M. J. The impact of specifically adsorbed ions on the copper-catalyzed electroreduction of CO_2. *J. Electrochem. Soc.* **2016**, *163*, F477–F484.

(226) Hersbach, T. J.; McCrum, I. T.; Anastasiadou, D.; Wever, R.; Calle-Vallejo, F.; Koper, M. T. M. Alkali metal cation effects in structuring Pt, Rh, and Au surfaces through cathodic corrosion. *ACS Appl. Mater. Interfaces* **2018**, *10*, 39363–39379.

(227) Andreussi, O.; Dabo, I.; Marzari, N. Revised self-consistent continuum solvation in electronic-structure calculations. *J. Chem. Phys.* **2012**, *136*, 064102.

(228) Bonnet, N.; Marzari, N. First-principles prediction of the equilibrium shape of nanoparticles under realistic electrochemical conditions. *Phys. Rev. Lett.* **2013**, *110*, 086104.

(229) Łodziana, Z.; Topsøe, N. Y.; Nørskov, J. K. A negative surface energy for alumina. *Nat. Mater.* **2004**, *3*, 289–293.

(230) Mathur, A.; Sharma, P.; Cammarata, R. C.; Łodziana, Z.; Topsøe, N. Y.; Nørskov, J. K. Negative surface energy - Clearing up confusion. *Nat. Mater.* **2005**, *4*, 186.

(231) Feibelman, P. J. Surface-diffusion mechanism versus electric field: Pt/Pt(001). *Phys. Rev. B* **2001**, *64*, 125403.

(232) Almora-Barrios, N.; Carchini, G.; Błoński, P.; López, N. Costless derivation of dispersion coefficients for metal surfaces. *J. Chem. Theory Comput.* **2014**, *10*, 5002–5009.

(233) Dattila, F. DFT datasets associated with "Emergence of potential-controlled Cu-nanocuboids and graphene-covered Cu-nanocuboids under Operando CO_2 electroreduction". `https://doi.org/10.19061/iochem-bd-1-185`, 2020; Online; accessed 29 July 2021.

(234) Wulff, G. Zur frage der geschwindigkeit des wachsthums und der auflösung der krystallflächen. *Z. Kristallog.* **1901**, *34*, 449–530.

(235) Barmparis, G. D.; Lodziana, Z.; López, N.; Remediakis, I. N. Nanoparticle shapes by using Wulff constructions and first-principles calculations. *Beilstein J. Nanotechnol.* **2015**, *6*, 361–368.

(236) Ouyang, R.; Liu, J. X.; Li, W. X. Atomistic theory of Ostwald ripening and disintegration of supported metal particles under reaction conditions. *J. Am. Chem. Soc.* **2013**, *135*, 1760–1771.

(237) Pršlja, P.; López, N. Stability and redispersion of Ni nanoparticles supported on N-doped carbons for the CO_2 electrochemical reduction. *ACS Catal.* **2021**, *11*, 88–94.

(238) Pršlja, P. DFT datasets associated with "Stability and redispersion of Ni nanoparticles supported on Ndoped carbons for the CO_2 electrochemical reduction". `https://doi.org/10.19061/iochem-bd-1-168`, 2020; Online; accessed 29 July 2021.

(239) Woodard, F. E.; Scortichini, C. L.; Reilley, C. N. H. Chemisorption and Related Anion Effects on Pt(110) Electrodes. *J. Electroanal. Chem. Interfacial Electrochem.* **1983**, *151*, 109–131.

(240) Gómez, R.; Clavilier, J. Electrochemical Behaviour of Platinum Surfaces Containing (110) Sites and the Problem of the Third Oxidation Peak. *J. Electroanal. Chem.* **1993**, *354*, 189–208.

(241) Diaz-Morales, O.; Hersbach, T. J.; Badan, C.; Garcia, A. C.; Koper, M. T. M. Hydrogen adsorption on nano-structured platinum electrodes. *Faraday Discuss.* **2018**, *210*, 301.

(242) Rost, C. M.; Sachet, E.; Borman, T.; Moballegh, A.; Dickey, E. C.; Hou, D.; Jones, J. L.; Curtarolo, S.; Maria, J.-P. Entropy-stabilized oxides. *Nat. Commun.* **2015**, *6*, 8485.

(243) Capdevila-Cortada, M.; López, N. Entropic contributions enhance polarity compensation for CeO_2(100) surfaces. *Nat. Mater.* **2017**, *16*, 328–334.

(244) Gao, D.; McCrum, I. T.; Deo, S.; Choi, Y.-W.; Scholten, F.; Wan, W.; Chen, J. G.; Janik, M. J.; Roldan Cuenya, B. Activity and selectivity control in CO_2 electroreduction to multicarbon products over CuO_x catalysts via electrolyte design. *ACS Catal.* **2018**, *8*, 10012–10020.

(245) Li, F. et al. Interplay of electrochemical and electrical effects induces structural transformations in electrocatalysts. *Nat. Catal.* **2021**, *4*, 479–487.

(246) Huang, H.-H. The Eh-pH diagram and its advances. *Metals* **2016**, *6*, 1–30.

(247) Scott, S. B. et al. Absence of oxidized phases in Cu under CO reduction conditions. *ACS Energy Lett.* **2019**, *4*, 803–804.

(248) Lee, S. H. et al. Oxidation state and surface reconstruction of Cu under CO_2 reduction conditions from *In Situ* Xray characterization. *J. Am. Chem. Soc.* **2021**, *143*, 588–592.

(249) Guan, R.; Hashimoto, H.; Kuo, K. H. Electron-microscopic study of the structure of metastable oxides formed in the initial stage of copper oxidation. II. Cu_8O. *Acta Cryst.* **1984**, *B40*, 560–566.

(250) Guan, R.; Hashimoto, H.; Kuo, K. H. Electron-microscopic study of the structure of

metastable oxides formed in the initial stage of copper oxidation. III. $Cu_{64}O$. *Acta Cryst.* **1985**, *B41*, 219–225.

(251) Favaro, M.; Xiao, H.; Cheng, T.; Goddard III, W. A.; Yano, J.; Crumlin, E. J. Subsurface oxide plays a critical role in CO_2 activation by Cu(111) surfaces to form chemisorbed CO_2, the first step in reduction of CO_2. *Proc. Natl. Acad. Sci. USA* **2017**, *114*, 6706–6711.

(252) Lee, S. Y.; Jung, H.; Kim, N.-K.; Oh, H.-S.; Min, B. K.; Hwang, Y. J. Mixed copper states in anodized Cu electrocatalyst for stable and selective ethylene production from CO_2 reduction. *J. Am. Chem. Soc.* **2018**, *140*, 8681–8689.

(253) Bai, X.; Li, Q.; Shi, L.; Niu, X.; Ling, C.; Wang, J. Hybrid Cu^0 and Cu^{x+} as atomic interfaces promote high-selectivity conversion of CO_2 to C_2H_5OH at low potential. *Small* **2019**, *16*, 1901981.

(254) Tomboc, G. M.; Choi, S.; Kwon, T.; Hwang, Y. J.; Lee, K. Potential link between Cu surface and selective CO_2 electroreduction: Perspective on future electrocatalyst designs. *Adv. Mater.* **2020**, *32*, 1908398.

(255) Lin, S.-C.; Chang, C.-C.; Chiu, S.-Y.; Pai, H.-T.; Liao, T.-Y.; Hsu, C.-S.; Chiang, W.-H.; Tsai, M.-K.; Chen, H. M. Operando time-resolved X-ray absorption spectroscopy reveals the chemical nature enabling highly selective CO_2 reduction. *Nat. Commun.* **2020**, *11*, 1–12.

(256) Zhang, W.; Huang, C.; Xiao, Q.; Yu, L.; Shuai, L.; An, P.; Zhang, J.; Qiu, M.; Ren, Z.; Yu, Y. Atypical oxygen-bearing copper boosts ethylene selectivity toward electrocatalytic CO_2 reduction. *J. Am. Chem. Soc.* **2020**, *142*, 11417–11427.

(257) Bai, H. et al. Controllable CO adsorption determines ethylene and methane productions from CO_2 electroreduction. *Sci. Bull.* **2020**, *66*, 62–68.

(258) Möller, T. et al. Electrocatalytic CO_2 reduction on CuO_x nanocubes tracking the evolution of chemical state, geometric structure, and catalytic selectivity using Operando Spectroscopy. *Angew. Chem. Int. Ed.* **2020**, *59*, 17974–17983.

(259) Garza, A. J.; Bell, A. T.; Head-Gordon, M. Is subsurface oxygen necessary for the electrochemical reduction of CO_2 on copper? *J. Phys. Chem. Lett.* **2018**, *9*, 601–606.

(260) Fields, M.; Hong, X.; Nørskov, J. K.; Chan, K. Role of subsurface oxygen on Cu surfaces for CO_2 electrochemical reduction. *J. Phys. Chem. C* **2018**, *122*, 16209–16215.

(261) Marx, D.; Hutter, J. *Ab initio molecular dynamics: basic theory and advanced methods*; Cambridge University Press, 2009.

(262) Mistry, A.; Franco, A. A.; Cooper, S. J.; Roberts, S. A.; Viswanathan, V. How machine learning will revolutionize electrochemical sciences. *ACS Energy Lett.* **2021**, *6*, 1422–1431.

(263) Zou, X.; Pan, J.; Sun, Z.; Wang, B.; Jin, Z.; Xu, G.; Yan, F. Machine learning analysis and prediction models of alkaline anion exchange membranes for fuel cells. *Energy Environ. Sci.* **2021**, *14*, 3965.

(264) Jacobsen, K. W.; Nørskov, J. K.; Puska, M. J. Interatomic interactions in the effective-medium theory. *Phys. Rev. B* **1987**, *35*, 7423.

(265) Jacobsen, K. W.; Stoltze, P.; Nørskov, J. K. A semi-empirical effective medium theory for metals and alloys. *Surf. Sci.* **1996**, *366*, 394–402.

(266) Gauthier, J. A.; Stenlid, J. H.; Abild-Pedersen, F.; Head-Gordon, M.; Bell, A. T. The role of roughening to enhance selectivity to C_{2+} products during CO_2 electroreduction on copper. *ACS Energy Lett.* **2021**, *6*, 3252–3260.

(267) Seifert, G. Tight-binding density functional theory: An approximate Kohn-Sham DFT scheme. *J. Phys. Chem. A* **2007**, *111*, 5609–5613.

(268) Peterson, A. A. Global optimization of adsorbate-surface structures while preserving molecular identity. *Top. Catal.* **2014**, *57*, 40–53.

(269) Perdew, J. P.; Burke, K.; Ernzerhof, M. Generalized gradient approximation made simple. *Phys. Rev. Lett.* **1996**, *77*, 3865–3868.

(270) Nosé, S. A unified formulation of the constant temperature molecular dynamics methods. *J. Chem. Phys.* **1984**, *81*, 511–519.

(271) Dattila, F. Supporting Videos 1-7 for "Active and selective ensembles in oxide-derived copper catalysts for CO_2 reduction". `https://iochem-bd.iciq.es/browse/handle/100/26145`, 2020; Online; accessed 24 July 2020.

(272) Dudarev, S. L.; Botton, G. A.; Savrasov, S. Y.; Humphreys, C. J.; Sutton, A. P. Electron-energy-loss spectra and the structural stability of nickel oxide: An LSDA+U study. *Phys. Rev. B* **1998**, *57*, 1505–1509.

(273) Isseroff, L. Y.; Carter, E. A. Importance of reference Hamiltonians containing exact exchange for accurate one-shot GW calculations of Cu_2O. *Phys. Rev. B* **2012**, *85*, 235142.

(274) Bendavid, L. I.; Carter, E. A. First-principles predictions of the structure, stability, and photocatalytic potential of Cu_2O surfaces. *J. Phys. Chem. B* **2013**, *117*, 15750–15760.

(275) Heinemann, M.; Eifert, B.; Heiliger, C. Band structure and phase stability of the copper oxides Cu_2O, CuO, and Cu_4O_3. *Phys. Rev. B* **2013**, *87*, 115111.

(276) Gattinoni, C.; Michaelides, A. Atomistic details of oxide surfaces and surface oxidation: The example of copper and its oxides. *Surf. Sci. Rep.* **2015**, *70*, 424–447.

(277) Yang, F.; Choi, Y.; Liu, P.; Hrbek, J.; Rodriguez, J. A. Autocatalytic reduction of a Cu_2O/Cu(111) surface by CO: STM, XPS, and DFT studies. *J. Phys. Chem. C* **2010**, *114*, 17042–17050.

(278) Yu, J.; Namba, Y. Atomic surface roughness. *Appl. Phys. Lett.* **1998**, *73*, 3607–3609.

(279) Birgersson, M.; Almbladh, C. O.; Borg, M.; Andersen, J. N. Density-functional theory applied to Rh(111) and CO/Rh(111) systems: Geometries, energies, and chemical shifts. *Phys. Rev. B* **2003**, *67*, 045402.

(280) Köhler, L.; Kresse, G. Density functional study of CO on Rh(111). *Phys. Rev. B* **2004**, *70*, 165405.

(281) Garofalini, S. H. Molecular dynamics simulation of the frequency spectrum of amorphous silica. *J. Chem. Phys.* **1982**, *76*, 3189–3192.

(282) Mandal, L. et al. Investigating the role of copper oxide in electrochemical CO_2 reduction in real time. *ACS Appl. Mater. Interfaces* **2018**, *10*, 8574–8584.

(283) Deng, Y.; Handoko, A. D.; Du, Y.; Xi, S.; Yeo, B. S. In Situ Raman spectroscopy of copper and copper oxide surfaces during electrochemical oxygen evolution reaction: Identification of Cu^{III} oxides as catalytically active species. *ACS Catal.* **2016**, *6*, 2473–2481.

(284) Zhao, Y.; Chang, X.; Malkani, A. S.; Yang, X.; Thompson, L.; Jiao, F.; Xu, B. Speciation of Cu surfaces during the electrochemical CO reduction reaction. *J. Am. Chem. Soc.* **2020**, *142*, 9735–9743.

(285) Van Duin, A. C. T.; Dasgupta, S.; Lorant, F.; Goddard III, W. A. ReaxFF: A reactive force field for hydrocarbons. *J. Phys. Chem. A* **2001**, *105*, 9396–9409.

(286) Chenoweth, K.; Van Duin, A. C. T.; Goddard III, W. A. ReaxFF reactive force field

for molecular dynamics simulations of hydrocarbon oxidation. *J. Phys. Chem. A* **2008**, *112*, 1040–1053.

(287) Cheng, T.; Xiao, H.; Goddard III, W. A. Nature of the active sites for CO reduction on copper nanoparticles; Suggestions for optimizing performance. *J. Am. Chem. Soc.* **2017**, *139*, 11642–11645.

(288) Daw, M. S.; Foiles, S. M.; Baskes, M. I. The embedded-atom method: a review of theory and applications. *Mater. Sci. Rep.* **1993**, *9*, 251–310.

(289) Huang, S. D.; Shang, C.; Kang, P.-L.; Zhang, X.-J.; Liu, Z.-P. LASP: Fast global potential energy surface exploration. *WIREs Comput Mol Sci.* **2019**, *9*, e1415.

(290) Nie, X.; Griffin, G. L.; Janik, M. J.; Asthagiri, A. Surface phases of $Cu_2O(111)$ under CO_2 electrochemical reduction conditions. *Catal. Commun.* **2014**, *52*, 88–91.

(291) Zhou, Y. DFT datasets associated with "The Role of Fe species on NiOOH in oxygen evolution reactions". `https://doi.org/10.19061/iochem-bd-1-147`, 2020; Online; accessed 29 July 2021.

(292) Elbaz, Y.; Caspary Toroker, M. Dual mechanisms: Hydrogen transfer during water oxidation catalysis of pure and Fe-doped nickel oxyhydroxide. *J. Phys. Chem. C* **2017**, *121*, 16819–16824.

(293) Casas-Cabanas, M.; Canales-Vázquez, J.; Rodríguez-Carvajal, J.; Palacín, M. R. Deciphering the structural transformations during nickel oxyhydroxide electrode operation. *J. Am. Chem. Soc.* **2007**, *129*, 5840–5842.

(294) Deng, J.; Nellist, M. R.; Stevens, M. B.; Dette, C.; Wang, Y.; Boettcher, S. W. Morphology dynamics of single-layered $Ni(OH)_2$/NiOOH nanosheets and subsequent Fe incorporation studied by *in situ* electrochemical Atomic Force Microscopy. *Nano Lett.* **2017**, *17*, 6922–6926.

(295) Doyle, A. D.; Bajdich, M.; Vojvodic, A. Theoretical insights to bulk activity towards oxygen evolution in oxyhydroxides. *Catal. Lett.* **2017**, *147*, 1533–1539.

(296) Xu, H. et al. Highly selective electrocatalytic CO_2 reduction to ethanol by metallic clusters dynamically formed from atomically dispersed copper. *Nat. Energy* **2020**, *5*, 623–632.

(297) Verdaguer-Casadevall, A.; Li, C. W.; Johansson, T. P.; Scott, S. B.; McKeown, J. T.; Kumar, M.; Stephens, I. E.; Kanan, M. W.; Chorkendorff, I. Probing the active surface sites for CO reduction on oxide-derived copper electrocatalysts. *J. Am. Chem. Soc.* **2015**, *137*, 9808–9811.

(298) Kim, D.; Kley, C. S.; Li, Y.; Yang, P. Copper nanoparticle ensembles for selective electroreduction of CO_2 to C_2–C_3 products. *Proc. Natl. Acad. Sci. U.S.A.* **2017**, *114*, 10560–10565.

(299) Huang, Y.; Handoko, A. D.; Hirunsit, P.; Yeo, B. S. Electrochemical reduction of CO_2 using copper single-crystal surfaces: Effects of CO* coverage on the selective formation of ethylene. *ACS Catal.* **2017**, *7*, 1749–1756.

(300) Calle-Vallejo, F.; Koper, M. T. M. Theoretical considerations on the electroreduction of CO to C_2 species on Cu(100) electrodes. *Angew. Chem. Int. Ed.* **2013**, *52*, 7282–7285.

(301) Green, G. An essay on the application of mathematical analysis to the theories of electricity and magnetism. *J. fur die Reine und Angew. Math.* **1852**, 356–374.

(302) García-Muelas, R.; Dattila, F.; Shinagawa, T.; Martín, A. J.; Pérez-Ramírez, J.; López, N. Origin of the selective electroreduction of carbon dioxide to formate by chalcogen modified copper. *J. Phys. Chem. Lett.* **2018**, *9*, 7153–7159.

(303) García-Muelas, R. DFT datasets associated with "Origin of the selective electroreduction of carbon dioxide to formate by chalcogen modified copper". https://doi.org/10.19061/iochem-bd-1-92, 2018; Online; accessed 29 July 2021.

(304) Vasileff, A.; Zhi, X.; Xu, C.; Ge, L.; Jiao, Y.; Zheng, Y.; Qiao, S. Z. Selectivity control for electrochemical CO_2 reduction by charge redistribution on the surface of copper alloys. *ACS Catal.* **2019**, *9*, 9411–9417.

(305) Pérez, L. C. P. et al. Determining structure-activity relationships in oxide derived Cu-Sn catalysts during CO_2 electroreduction using X-Ray Spectroscopy. *Adv. Energy Mater.* **2022**, *12*, 2103328.

(306) Dattila, F. DFT datasets associated with "Determining structure-activity relationships in oxide derived Cu-Sn catalysts during CO_2 electroreduction using X-ray spectroscopy". https://doi.org/10.19061/iochem-bd-1-211, 2021; Online; accessed 24 December 2021.

(307) Xiao, H.; Goddard III, W. A.; Cheng, T.; Liu, Y. Cu metal embedded in oxidized matrix catalyst to promote CO_2 activation and CO dimerization for electrochemical reduction of CO_2. *Proc. Natl. Acad. Sci. USA* **2017**, *114*, 6685–6688.

(308) Sang, J. et al. A reconstructed $Cu_2P_2O_7$ catalyst for selective CO_2 electroreduction to multicarbon products. *Angew. Chem. Int. Ed.* **2022**, *61*, e202114238.

(309) Ismail, A. M.; Samu, G. F.; Nguyën, H. C.; Csapó, E.; López, N.; Janáky, C. Au/Pb interface allows methane formation pathway in carbon dioxide electroreduction. *ACS Catal.* **2020**, *10*, 5681–5690.

(310) Nguyën, H. C. DFT datasets associated with "Au/Pb interface allows methane formation pathway in carbon dioxide electroreduction". https://doi.org/10.19061/iochem-bd-1-167, 2020; Online; accessed 29 July 2021.

(311) Pavesi, D.; Dattila, F.; Van de Poll, R. C. J.; Anastasiadou, D.; García-Muelas, R.; Figueiredo, M.; Gruter, G.-J. M.; López, N.; Koper, M. T. M.; Jan Schouten, K. Modulation of the selectivity of CO_2 to CO electroreduction in Palladium rich Palladium-Indium nanoparticles. *J. Catal.* **2021**, *402*, 229–237.

(312) Dattila, F. DFT datasets associated with "Modulation of the selectivity of CO_2 to CO electroreduction in Palladium rich Palladium-Indium nanoparticles". `https://doi.org/10.19061/iochem-bd-1-207`, 2021; Online; accessed 24 December 2021.

(313) Dattila, F. DFT datasets associated with "Active and selective ensembles in oxide-derived copper catalysts for CO_2 Reduction". `https://doi.org/10.19061/iochem-bd-1-165`, 2020; Online; accessed 29 July 2021.

(314) Dattila, F. Glyoxylate-like configurations: (O_{ss})OCCO, sites 1-9. `https://doi.org/10.19061/iochem-bd-1-165`, 2020; Online; accessed 24 July 2020.

(315) Muchowska, K. B.; Varma, S. J.; Moran, J. Synthesis and breakdown of universal metabolic precursors promoted by iron. *Nature* **2019**, *569*, 104–107.

(316) Choi, Y. W.; Mistry, H.; Roldan Cuenya, B. New insights into working nanostructured electrocatalysts through operando spectroscopy and microscopy. *Curr. Opin. Electrochem.* **2017**, *1*, 95–103.

(317) Katayama, Y.; Nattino, F.; Giordano, L.; Hwang, J.; Rao, R. R.; Andreussi, O.; Marzari, N.; Shao-Horn, Y. An *In Situ* surface-enhanced infrared absorption spectroscopy study of electrochemical CO_2 reduction: Selectivity dependence on surface C-bound and O-bound reaction intermediates. *J. Phys. Chem. C* **2019**, *123*, 5951–5963.

(318) Dattila, F. DFT datasets associated with "Revealing the CO coverage-driven C–C coupling mechanism for electrochemical CO_2 reduction on Cu_2O nanocubes *via Operando*

Raman spectroscopy". https://doi.org/10.19061/iochem-bd-1-192, 2021; Online; accessed 29 July 2021.

(319) Hori, Y.; Wakebe, H.; Tsukamoto, T.; Koga, O. Electrocatalytic process of CO selectivity in electrochemical reduction of CO_2 at metal electrodes in aqueous media. *Electrochimica Acta* **1994**, *39*, 1833–1839.

(320) Vijay, S.; Ju, W.; Brückner, S.; Tsang, S.-C.; Strasser, P.; Chan, K. Unified mechanistic understanding of CO_2 reduction to CO on transition metal and single atom catalysts. *Nat. Catal.* **2021**, *4*, 1024–1031.

(321) Amatore, C.; Savéant, J. M. Mechanism and kinetic characteristics of the electrochemical reduction of carbon dioxide in media of low proton availability. *J. Am. Chem. Soc.* **1981**, *103*, 5021–5023.

(322) Hori, Y.; Murata, A.; Kikuchi, K.; Suzuki, S. Electrochemical reduction of carbon dioxide to carbon monoxide at a gold electrode in aqueous potassium hydrogen carbonate. *J. Chem. Soc., Chem. Commun.* **1987**, 728–729.

(323) Wuttig, A.; Yaguchi, M.; Motobayashi, K.; Osawa, M.; Surendranath, Y. Inhibited proton transfer enhances Au-catalyzed CO_2-to-fuels selectivity. *Proc. Natl. Acad. Sci. USA* **2016**, *113*, E4585–E4593.

(324) Gauthier, J. A.; Fields, M.; Bajdich, M.; Chen, L. D.; Sandberg, R. B.; Chan, K.; Nørskov, J. K. Facile electron transfer to CO_2 during adsorption at the metal — solution Interface. *J. Phys. Chem. C* **2019**, *123*, 29278–29283.

(325) Peterson, A. A.; Nørskov, J. K. Activity descriptors for CO_2 electroreduction to methane on transition-metal catalysts. *J. Phys. Chem. Lett.* **2012**, *3*, 251–258.

(326) Peng, H.; Tang, M. T.; Liu, X.; Lamoureux, P. S.; Bajdich, M.; Abild-pedersen, F.

The role of atomic carbon in directing electrochemical $CO_{(2)}$ reduction to multicarbon products. *Energy Environ. Sci.* **2021**, *14*, 473–482.

(327) Yoo, J. S.; Christensen, R.; Vegge, T.; Nørskov, J. K.; Studt, F. Theoretical insight into the trends that guide the electrochemical reduction of carbon dioxide to formic acid. *ChemSusChem* **2016**, *9*, 358–363.

(328) Liu, H.; Liu, J.; Yang, B. Promotional role of a cation intermediate complex in C_2 formation from electrochemical reduction of CO_2 over Cu. *ACS Catal.* **2021**, *11*, 12336–12343.

(329) Santatiwongchai, J.; Faungnawakij, K.; Hirunsit, P. Comprehensive mechanism of CO_2 electroreduction toward ethylene and ethanol: The solvent effect from explicit waterCu(100) interface models. *ACS Catal.* **2021**, *11*, 9688–9701.

(330) Kibria, M. G.; Edwards, J. P.; Gabardo, C. M.; Dinh, C.-T.; Seifitokaldani, A.; Sinton, D.; Sargent, E. H. Electrochemical CO_2 reduction into chemical feedstocks: From mechanistic electrocatalysis models to system design. *Adv. Mater.* **2019**, *31*, 1807166.

(331) Chang, X.; Li, J.; Xiong, H.; Zhang, H.; Xu, Y.; Xiao, H.; Lu, Q.; Xu, B. CC Coupling is unlikely to be the ratedetermining step in the formation of C_{2+} products in the coppercatalyzed electrochemical reduction of CO. *Angew. Chem. Int. Ed.* **2022**, *61*, e202111167.

(332) Kibria, M. G. et al. A surface reconstruction route to high productivity and selectivity in CO_2 electroreduction toward C_{2+} hydrocarbons. *Adv. Mater.* **2018**, *30*, 1804867.

(333) Ledezma-Yanez, I.; Gallent, E. P.; Koper, M. T. M.; Calle-Vallejo, F. Structure-sensitive electroreduction of acetaldehyde to ethanol on copper and its mechanistic implications for CO and CO_2 reduction. *Catal. Today* **2016**, *262*, 90–94.

(334) Pablo-García, S.; Veenstra, F. L. P.; Ting, L. R. L.; García-Muelas, R.; Martín, A. J.; Dattila, F.; Yeo, B. S.; Pérez-Ramírez, J.; López, N. Mechanistic routes toward C_3 products in copper-catalysed CO_2 electroreduction. *Catal. Sci. Technol.* **2022**, *12*, 409–417.

(335) Clark, E. L.; Wong, J.; Garza, A. J.; Lin, Z.; Head-Gordon, M.; Bell, A. T. Explaining the incorporation of oxygen derived from solvent water into the oxygenated products of CO reduction over Cu. *J. Am. Chem. Soc.* **2019**, *141*, 4191–4193.

(336) Heenen, H. H.; Kastlunger, G.; Shin, H.; Overa, S.; Gauthier, J. A.; Jiao, F.; Chan, K. Mechanism for acetate formation in $CO_{(2)}$ reduction on Cu: Selectivity trends with pH and nanostructuring derive from mass transport. *ChemRxiv* **2021**, DOI: 10.26434/chemrxiv–2021–p3d4s. This content is a preprint and has not been peer–reviewed.

(337) Pang, Y. et al. Efficient electrocatalytic conversion of carbon monoxide to propanol using fragmented copper. *Nat. Catal.* **2019**, *2*, 251–258.

(338) Choi, M.; Bong, S.; Kim, J. W.; Lee, J. Formation of 1-Butanol from CO_2 without *CO dimerization on a phosphorus-rich copper cathode. *ACS Energy Lett.* **2021**, *6*, 2090–2095.

(339) Marcandalli, G.; Goyal, A.; Koper, M. T. M. Electrolyte effects on the Faradaic efficiency of CO_2 reduction to CO on a gold electrode. *ACS Catal.* **2021**, *11*, 4936–4945.

(340) Bondue, C. J.; Graf, M.; Goyal, A.; Koper, M. T. M. Suppression of hydrogen evolution in acidic electrolytes by electrochemical CO_2 reduction. *J. Am. Chem. Soc.* **2021**, *143*, 279–285.

(341) Marshall, A. T. Using microkinetic models to understand electrocatalytic reactions. *Current Opinion in Electrochemistry* **2018**, *7*, 75–80.

(342) Liu, D.-Q. et al. Adiabatic versus non-adiabatic electron transfer at 2D electrode materials. *Nat. Commun.* **2021**, *12*, 7110.

(343) Li, J.; Stenlid, J. H.; Ludwig, T.; Lamoureux, P. S.; Abild-Pedersen, F. Modeling potential-dependent electrochemical activation barriers: Revisiting the alkaline hydrogen evolution reaction. *J. Am. Chem. Soc.* **2021**, *143*, 19341–19355.

(344) Liu, X.; Xiao, J.; Peng, H.; Hong, X.; Chan, K.; Nørskov, J. K. Understanding trends in electrochemical carbon dioxide reduction rates. *Nat. Commun.* **2017**, *8*, 15438.

(345) Rohr, B. A.; Singh, A. R.; Gauthier, J. A.; Statt, M. J.; Nrskov, J. K. Micro-kinetic model of electrochemical carbon dioxide reduction over platinum in non-aqueous solvents. *Phys. Chem. Chem. Phys.* **2020**, *22*, 9040–9045.

(346) Zijlstra, B.; Zhang, X.; Liu, J.-X.; Filot, I. A.; Zhou, Z.; Sun, S.; Hensen, E. J. First-principles microkinetics simulations of electrochemical reduction of CO_2 over Cu catalysts. *Electrochimica Acta* **2020**, *335*, 135665.

(347) Kastlunger, G.; Wang, L.; Govindarajan, N.; Heenen, H. H.; Ringe, S.; Jaramillo, T.; Hahn, C.; Chan, K. Using pH dependence to understand mechanisms in electrochemical CO reduction. *ACS Catal.* **2022**, *12*, 4344–4357.

(348) Limaye, A. M.; Zeng, J. S.; Willard, A. P.; Manthiram, K. Bayesian data analysis reveals no preference for cardinal Tafel slopes in CO_2 reduction electrocatalysis. *Nat. Commun.* **2021**, *12*, 703.

(349) Liu, X. et al. pH effects on the electrochemical reduction of $CO_{(2)}$ towards C_2 products on stepped copper. *Nat. Commun.* **2019**, *10*, 32.

(350) Wang, L. et al. Electrochemical carbon monoxide reduction on polycrystalline copper: Effects of potential, pressure, and pH on selectivity toward multicarbon and oxygenated products. *ACS Catal.* **2018**, *8*, 7445–7454.

(351) Singh, M. R.; Goodpaster, J. D.; Weber, A. Z.; Head-Gordon, M.; Bell, A. T. Mechanistic insights into electrochemical reduction of CO_2 over Ag using density functional theory and transport models. *P.N.A.S.* **2017**, *114*, E8812–E8821.

(352) Hara, K.; Kudo, A.; Sakata, T. Electrochemical reduction of carbon dioxide under high pressure on various electrodes in an aqueous electrolyte. *J. Electroanal. Chem.* **1995**, *391*, 141–147.

(353) Creative Commons Attribution-NonCommercial-NoDerivatives 4.0 International (CC BY-NC-ND 4.0) License. `https://creativecommons.org/licenses/by-nc-nd/4.0/`, Online; accessed 24 December 2021.

(354) Clark, E. L.; Bell, A. T. Direct observation of the local reaction environment during the electrochemical reduction of CO_2. *J. Am. Chem. Soc.* **2018**, *140*, 7012–7020.

(355) Philips, M. F.; Gruter, G.-J. M.; Koper, M. T. M.; Schouten, K. J. P. Optimizing the electrochemical reduction of CO_2 to formate: A State-of-the-Art analysis. *ACS Sustainable Chem. Eng.* **2020**, *8*, 15430–15444.

(356) Burdyny, T.; Smith, W. A. CO_2 reduction on gas-diffusion electrodes and why catalytic performance must be assessed at commercially-relevant conditions. *Energy Environ. Sci.* **2019**, *12*, 1442–1453.

(357) Rabinowitz, J. A.; Kanan, M. W. The future of low-temperature carbon dioxide electrolysis depends on solving one basic problem. *Nat. Commun.* **2020**, *11*, 5231.

(358) Birdja, Y. Y.; Koper, M. T. M. The importance of Cannizzaro-type reactions during electrocatalytic reduction of carbon dioxide. *J. Am. Chem. Soc.* **2017**, *139*, 2030–2034.

(359) Monteiro, M. C. O.; Philips, M. F.; Schouten, K. J. P.; Koper, M. T. M. Efficiency and selectivity of CO_2 reduction to CO on gold gas diffusion electrodes in acidic media. *Nat. Commun.* **2021**, *12*, 4943.

(360) Pérez-Gallent, E.; Marcandalli, G.; Figueiredo, M. C.; Calle-Vallejo, F.; Koper, M. T. M. Structure-and potential-dependent cation effects on CO reduction at copper single-crystal electrodes. *J. Am. Chem. Soc.* **2017**, *139*, 16412–16419.

(361) Frumkin, A. N. Influence of cation adsorption on the kinetics of electrode processes. *Trans. Faraday Soc.* **1959**, *55*, 156–167.

(362) Waegele, M. M.; Gunathunge, C. M.; Li, J.; Li, X. How cations affect the electric double layer and the rates and selectivity of electrocatalytic processes. *J. Chem. Phys.* **2019**, *151*, 160902.

(363) Mills, J. N.; McCrum, I. T.; Janik, M. J. Alkali cation specific adsorption onto fcc(111) transition metal electrodes. *Phys. Chem. Chem. Phys.* **2014**, *16*, 13699.

(364) Dunwell, M.; Wang, J.; Yan, Y.; Xu, B. Surface enhanced spectroscopic investigations of adsorption of cations on electrochemical interfaces. *Phys. Chem. Chem. Phys.* **2017**, *19*, 971.

(365) Malkani, A. S.; Li, J.; Oliveira, N. J.; He, M.; Chang, X.; Xu, B.; Lu, Q. Understanding the electric and nonelectric field components of the cation effect on the electrochemical CO reduction reaction. *Sci. Adv.* **2020**, *6*, eabd2569.

(366) Hussain, G.; Pérez-Martínez, L.; Le, J.-B.; Papasizza, M.; Cabello, G.; Cheng, J.; Cuesta, A. How cations determine the interfacial potential profile: Relevance for the CO_2 reduction reaction. *Electrochim. Acta* **2019**, *327*, 135055.

(367) Singh, M. R.; Clark, E. L.; Bell, A. T. Effects of electrolyte, catalyst, and membrane composition and operating conditions on the performance of solar-driven electrochemical reduction of carbon dioxide. *Phys. Chem. Chem. Phys.* **2015**, *17*, 18924–18936.

(368) Malkani, A. S.; Anibal, J.; Xu, B. Cation effect on interfacial CO_2 concentration in the electrochemical CO_2 reduction reaction. *ACS Catal.* **2020**, *10*, 14871–14876.

(369) Ayemoba, O.; Cuesta, A. Spectroscopic evidence of size-dependent buffering of interfacial pH by cation hydrolysis during CO_2 electroreduction. *ACS Appl. Mater. Interfaces* **2017**, *9*, 27377–27382.

(370) Zhu, Q.; Wallentine, S. K.; Deng, G.-H.; Rebstock, J. A.; Baker, L. R. The solvation-induced Onsager reaction field rather than the double-layer field controls CO_2 reduction on gold. *JACS Au* **2022**, *2*, 472–482.

(371) Dattila, F. DFT datasets associated with "Absence of CO_2 electroreduction on copper, gold and silver electrodes without metal cations in solution". `https://doi.org/10.19061/iochem-bd-1-194`, 2021; Online; accessed 29 July 2021.

(372) Borukhov, I.; Andelman, D.; Orland, H. Adsorption of large ions from an electrolyte solution: A modified Poisson-Boltzmann equation. *Electrochim. Acta* **2000**, *46*, 221–229.

(373) Xue, S.; Garlyyev, B.; Watzele, S.; Liang, Y.; Fichtner, J.; Pohl, M. D.; Bandarenka, A. S. Influence of alkali metal cations on the hydrogen evolution reaction activity of Pt, Ir, Au, and Ag electrodes in alkaline electrolytes. *ChemElectroChem* **2018**, *5*, 2326–2329.

(374) McCrum, I. T.; Koper, M. T. M. The role of adsorbed hydroxide in hydrogen evolution reaction kinetics on modified platinum. *Nat. Energy* **2020**, *5*, 1–9.

(375) Monteiro, M. C.; Goyal, A.; Moerland, P.; Koper, M. T. M. Understanding cation trends for hydrogen evolution on platinum and gold electrodes in alkaline media. *ACS Catal.* **2021**, *11*, 14328–14335.

(376) Dattila, F. DFT datasets associated with "The role of cation acidity on the competition between hydrogen evolution and CO_2 reduction on gold electrodes". `https://doi.org/10.19061/iochem-bd-1-213`, 2021; Online; accessed 24 December 2021.

(377) Marcus, Y. Ionic radii in aqueous solutions. *Chem. Rev.* **1988**, *88*, 1475–1498.

(378) Schouten, K. J. P.; Qin, Z.; Pérez Gallent, E.; Koper, M. T. M. Two pathways for the formation of ethylene in CO reduction on single-crystal copper electrodes. *J. Am. Chem. Soc.* **2012**, *134*, 9864–9867.

(379) Shinagawa, T.; Garcia-Esparza, A. T.; Takanabe, K. Insight on Tafel slopes from a microkinetic analysis of aqueous electrocatalysis for energy conversion. *Sci. Rep.* **2015**, *5*, 13801.

(380) Monteiro, M. C. O.; Koper, M. T. M. Measuring local pH in electrochemistry. *Curr. Opin. Electrochem.* **2021**, *25*, 100649.

(381) Monteiro, M. C. O.; Jacobse, L.; Koper, M. T. M. Understanding the voltammetry of bulk CO electrooxidation in neutral media through combined SECM M-measurements. *J. Phys. Chem. Lett.* **2020**, *11*, 9708–9713.

(382) Monteiro, M.; Jacobse, L.; Touzalin, T.; Koper, M. T. M. Mediator-free SECM for probing the diffusion layer pH with functionalized gold ultramicroelectrodes. *Anal. Chem.* **2019**, *92*, 2237–2243.

(383) Monteiro, M. C. O.; Mirabal, A.; Jacobse, L.; Doblhoff-Dier, K.; Barton, S. C.; Koper, M. T. M. Time-resolved local pH measurements during CO_2 reduction using scanning electrochemical microscopy: Buffering and tip effects. *JACS Au* **2021**, *1*, 1915–1924.

(384) Zhang, Z.; Melo, L.; Jansonius, R. P.; Habibzadeh, F.; Grant, E. R.; Berlinguette, C. P. pH matters when reducing CO_2 in an electrochemical flow cell. *ACS Energy Lett.* **2020**, *5*, 215–220.

(385) Zhang, F.; Co, A. C. Direct evidence of local pH change and the role of alkali cation

during CO_2 electroreduction in aqueous media. *Angew. Chem. Int. Ed.* **2020**, *59*, 1674–1681.

(386) Yang, K.; Kas, R.; Smith, W. A. In Situ infrared spectroscopy reveals persistent alkalinity near electrode surfaces during CO_2 electroreduction. *J. Am. Chem. Soc.* **2019**, *141*, 15891–15900.

(387) Dunwell, M.; Yang, X.; Setzler, B. P.; Anibal, J.; Yan, Y.; Xu, B. Examination of near-electrode concentration gradients and kinetic impacts on the electrochemical reduction of CO_2 using surface-enhanced infrared spectroscopy. *ACS Catal.* **2018**, *8*, 3999–4008.

(388) Zhang, B. A.; Ozel, T.; Elias, J. S.; Costentin, C.; Nocera, D. G. Interplay of homogeneous reactions, mass transport, and kinetics in determining selectivity of the reduction of CO_2 on gold electrodes. *ACS Cent. Sci.* **2019**, *5*, 1097–1105.

(389) Kas, R.; Star, A. G.; Yang, K.; Cleve, T. V.; Neyerlin, K. C.; Smith, W. A. Along the channel gradients impact on the spatioactivity of gas diffusion electrodes at high conversions during CO_2 electroreduction. *ACS Sustainable Chem. Eng.* **2021**, *9*, 1286–1296.

(390) Raciti, D.; Mao, M.; Wang, C. Mass transport modeling for the electroreduction of CO_2 on Cu nanowires. *Nanotechnology* **2018**, *29*, 044001.

(391) El-Kharouf, A.; Mason, T. J.; Brett, D. J. L.; Pollet, B. G. Ex-situ characterisation of gas diffusion layers for proton exchange membrane fuel cells. *J. Power Sources* **2012**, *218*, 393–404.

(392) Morawietz, T.; Artrith, N. Machine learning-accelerated quantum mechanics-based atomistic simulations for industrial applications. *J. Comput. Aided Mol. Des.* **2021**, *35*, 557–586.

(393) Ulissi, Z. W.; Medford, A. J.; Bligaard, T.; Nørskov, J. K. To address surface reaction network complexity using scaling relations machine learning and DFT calculations. *Nat. Commun.* **2017**, *8*, 14621.

(394) Zhang, N. et al. Machine Learning in screening high performance electrocatalysts for CO_2 reduction. *Small Methods* **2021**, *5*, 2100987.

(395) Li, Z.; Ma, X.; Xin, H. Feature engineering of machine-learning chemisorption models for catalyst design. *Catal. Today* **2017**, *280*, 232–238.

(396) Li, Z.; Wang, S.; Chin, W. S.; Achenie, L. E.; Xin, H. High-throughput screening of bimetallic catalysts enabled by machine learning. *J. Mater. Chem. A* **2017**, *5*, 24131–24138.

(397) Tran, K.; Ulissi, Z. W. Active learning across intermetallics to guide discovery of electrocatalysts for CO_2 reduction and H_2 evolution. *Nat. Catal.* **2018**, *1*, 696–703.

(398) Zhong, M. et al. Accelerated discovery of CO_2 electrocatalysts using active machine learning. *Nature* **2020**, *581*, 178–183.

(399) Behler, J.; Parrinello, M. Generalized neural-network representation of high-dimensional potential-energy surfaces. *Phys. Rev. Lett.* **2007**, *98*, 146401.

(400) Artrith, N.; Hiller, B.; Behler, J. Neural network potentials for metals and oxides - First applications to copper clusters at zinc oxide. *Phys. Status Solidi B* **2013**, *250*, 1191–1203.

(401) Kolsbjerg, E. L.; Peterson, A. A.; Hammer, B. Neural-network-enhanced evolutionary algorithm applied to supported metal nanoparticles. *Phys. Rev. B* **2018**, *97*, 195424.

(402) Artrith, N.; Kolpak, A. M. Understanding the composition and activity of electrocatalytic nanoalloys in aqueous solvents: A combination of DFT and accurate neural network potentials. *Nano Lett.* **2014**, *14*, 2670–2676.

(403) Artrith, N.; Kolpak, A. M. Grand canonical molecular dynamics simulations of Cu-Au nanoalloys in thermal equilibrium using reactive ANN potentials. *Comput. Mater. Sci.* **2015**, *110*, 20–28.

(404) Riniker, S. Molecular dynamics fingerprints (MDFP): Machine learning from MD data to predict free-energy differences. *J. Chem. Inf. Model.* **2017**, *57*, 726–741.

(405) Behler, J. Constructing high-dimensional neural network potentials: A tutorial review. *Int. J. Quantum Chem.* **2015**, *115*, 1032–1050.

(406) Behler, J. First principles neural network potentials for reactive simulations of large molecular and condensed systems. *Angew. Chem. Int. Ed.* **2017**, *56*, 12828–12840.

(407) Behrens, M. et al. The active site of methanol synthesis over $Cu/ZnO/Al_2O_3$ industrial catalysts. *Science* **2012**, *336*, 893–897.

(408) Varandili, S. B.; Stoian, D.; Vavra, J.; Rossi, K.; Pankhurst, J. R.; Guntern, Y.; López, N.; Buonsanti, R. Elucidating the structure-dependent selectivity towards methane and ethanol of CuZn in the CO_2 electroreduction using tailored Cu/ZnO precatalysts. *Chem. Sci.* **2021**, *12*, 14484–14493.

(409) Guzmán, H.; Salomone, F.; Batuecas, E.; Tommasi, T.; Russo, N.; Bensaid, S.; Hernández, S. How to make sustainable CO_2 conversion to Methanol: Thermocatalytic versus electrocatalytic technology. *Chem. Eng. J.* **2021**, *417*.

(410) Selvaratnam, B.; Koodali, R. T.; Miró, P. Prediction of optoelectronic properties of Cu_2O using neural network potential. *Phys. Chem. Chem. Phys.* **2020**, *22*, 14910–14917.

(411) Wei, J.; De Luna, P.; Bengio, Y.; Aspuru-Guzik, A.; Sargent, E. H. Use machine learning to find energy materials. *Nature* **2017**, *552*, 23–25.

(412) Timoshenko, J.; Jeon, H. S.; Sinev, I.; Haase, F. T.; Herzog, A.; Roldan Cuenya, B. Linking the evolution of catalytic properties and structural changes in copper-zinc nanocatalysts using: operando EXAFS and neural-networks. *Chem. Sci.* **2020**, *11*, 3727.

(413) Creative Commons Attribution 3.0 Unported Licence. `https://creativecommons.org/licenses/by/3.0/`, Online; accessed 5 August 2021.

(414) Jeon, H. S.; Timoshenko, J.; Scholten, F.; Sinev, I.; Herzog, A.; Haase, F. T.; Roldan Cuenya, B. Operando insight into the correlation between the structure and composition of CuZn nanoparticles and their selectivity for the electrochemical CO_2 reduction. *J. Am. Chem. Soc.* **2019**, *141*, 19879–19887.

(415) Artrith, N.; Butler, K. T.; Coudert, F.-X.; Han, S.; Isayev, O.; Jain, A.; Walsh, A. Best practices in machine learning for chemistry. *Nat. Chem.* **2021**, *13*, 505–508.

(416) Álvarez-Moreno, M.; de Graaf, C.; López, N.; Maseras, F.; Poblet, J.; Bo, C. Managing the computational chemistry big data problem: The ioChem-BD Platform. *J. Chem. Inf. Model.* **2015**, *55*, 95–103.

(417) Bo, C.; Maseras, F.; López, N. The role of computational results databases in accelerating the discovery of catalysts. *Nat. Catal.* **2018**, *1*, 809–810.

(418) ioChem-BD. `https://www.iochem-bd.org/`, Online; accessed 29 July 2021.

(419) The Materials Project. `https://www.materialsproject.org/`, Online; accessed 29 July 2021.

(420) Hummelshøj, J. S.; Abild-Pedersen, F.; Studt, F.; Bligaard, T.; Nørskov, J. K. CatApp: A web application for surface chemistry and heterogeneous catalysis. *Angew. Chem. Int. Ed.* **2012**, *51*, 272–274.

(421) Garcés-Pineda, F. A.; Blasco-Ahicart, M.; Nieto-Castro, D.; López, N.; Galán-Mascarós, J. R. Direct magnetic enhancement of electrocatalytic water oxidation in alkaline media. *Nat. Energy* **2019**, *4*, 519–525.

(422) Bhargava, S. S.; Azmoodeh, D.; Chen, X.; Cofell, E. R.; Esposito, A. M.; Verma, S.; Gewirth, A. A.; Kenis, P. J. A. Decreasing the energy consumption of the CO_2 electrolysis process using a magnetic field. *ACS Energy Lett.* **2021**, *6*, 2427–2433.

(423) Kitchin, J. R. Machine learning in catalysis. *Nat. Catal.* **2018**, *1*, 230–232.

(424) Ulissi, Z. W. et al. Machine-learning methods enable exhaustive searches for active bimetallic facets and reveal active site motifs for CO_2 reduction. *ACS Catal.* **2017**, *7*, 6600–6608.

Graphical TOC entry